Shallow Gas: Rock Physics and AVO

An analysis of the seismic response as a function of gas saturation

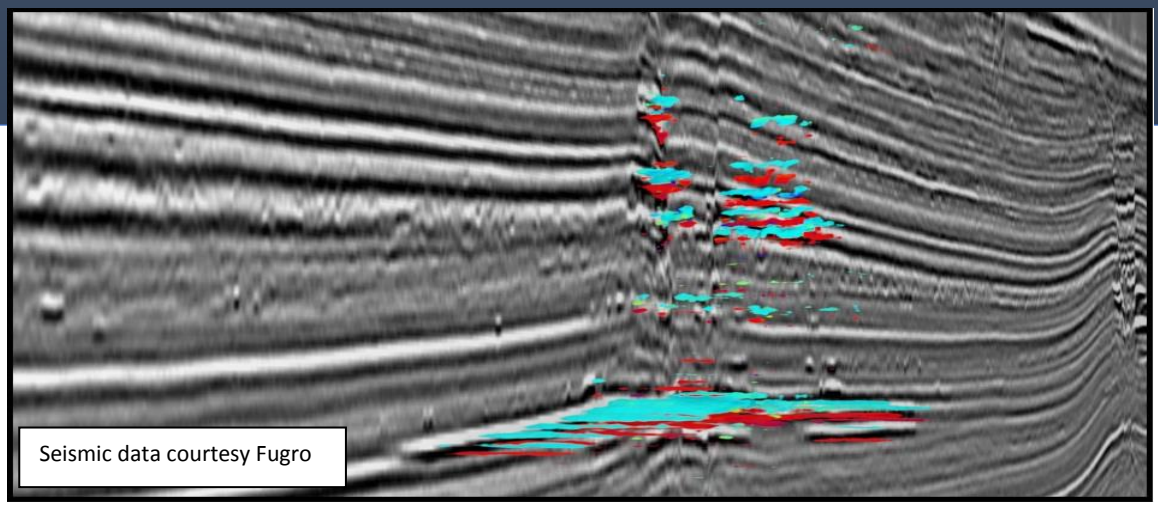

Martijn M.T.G. Janssen

June 2015

Student number – 4139194
(F120805)

Master Thesis – GEO4-1520

Supervisors:
M. Boogaard, van den (EBN)
H.L.J.G. Hoetz (EBN)
Prof. dr. J.A. Trampert (UU)

Universiteit Utrecht

EBN B.V., Daalsesingel 1, 3511 SV Utrecht, The Netherlands, Telephone: +31 (0)30 2339001.

Utrecht University, Faculty of Geosciences, Department of Earth Sciences, Princetonplein 6, 3584 CC Utrecht, The Netherlands, Telephone: +31 (0)30 2535151.

First Printing, May 2015

Acknowledgements

I would like to thank EBN B.V. for giving me the opportunity to do my graduation research and internship in this unique environment, providing me the chance to experience the Dutch E&P industry from the inside. The last eight months were really inspiring, working on an interesting and challenging project. Thanks go to all colleagues and interns at EBN B.V. for their help and for creating a fantastic working atmosphere. Especially Mijke van den Boogaard and Guido Hoetz are thanked for their continuous support, input and supervision throughout the entire project. Walter Eikelenboom and Jan Lutgert are thanked for respectively guidance with Petrel software and help with the petrophysical analysis. Many thanks go to Headwave, Inc. for the provision of their software and to Hugo Poelen for helping me to understand and to use the Headwave software. Jeannot Trampert is also thanked for his supervision. And last but not least, I would like to thank Gerhard Diephuis and John Verbeek for their discussion sessions during the project.

Abstract

As a result of the presence of hydrocarbons, ample shallow seismic anomalies are observed in sediments of Cenozoic age in the northern part of the Dutch North Sea area. In The Netherlands, which was the first of all North Sea countries that started producing the *play*, there are currently three successfully producing shallow fields. The sand production that was expected is effectively controlled by the use of mechanical sand control methods and no water breakthrough is seen so far. With almost eight years of production, the shallow play has proven to be a valuable resource in The Netherlands. There are, besides the three producing fields, still many possibilities for the production of shallow gas in the Dutch offshore section. Therefore a better understanding of its seismic signature is required. The main challenge in assessing these shallow anomalies, or *bright spots*, is that amplitude brightening already occurs at very low (non-producible) gas saturations or it might even have a lithological origin. Therefore, gas saturation is seen as the largest pre-drill uncertainty. In this study, a detailed forward model, which contains parameters that are used to describe these shallow *reservoirs*, is compared with the *amplitude versus offset* (AVO) behavior of state-of-the-art pre-stack seismic data of the study area: the F04/F05 licence blocks in the Dutch offshore section. Attention is paid to the relationship between the AVO response and the gas saturation; is distinction between low and high gas saturations possible by analyzing the seismic response of shallow gas in the pre-stack domain?

In order to obtain representative *reservoir* and *seal* parameters for the modelling work, petrophysical analyses are performed using data from three different wells within the study area. A total of eight wells were drilled in the F04/F05 blocks. Although all the wells drilled show limited data availability of the shallow subsurface, datasets from wells F04-01, F05-01 and F05-04 are used due to their data accessibility for both shallow sand and shale layers. The outcomes of wells F04-01 and F05-01 show potential *net-to-gross* (N/G) ratios of 50%. A clean sand interval with overlying shale layer, resulting from the petrophysical analysis of well F04-01, is marked as a *base-case* scenario due to the estimated net-to-gross ratios for both seal and reservoir of respectively 20% and 50%. Log data (compressional wave velocity) and estimated density and shear wave velocity data are used to construct a model of elastic properties for the water-bearing situation; the base-case. Next, Gassmann's algorithm is applied to derive new elastic properties for different gas saturations. The complete V_p-V_s-ρ sets act as input parameters for the Zoeppritz equations. The full Zoeppritz equations are used to model the variation in amplitude with *offset* for various gas saturations within the reservoir, corresponding to the top-reservoir reflector. A *stochastic* approach has been applied to the Zoeppritz equations. Modelling results show that in most of the cases the AVO trends for gas-bearing sediments indicate increasing negative amplitudes with increasing offset (e.g. class 3 anomalies). The pre-stack seismic data is initially analyzed using the *intercept-gradient* method. This method yields five AVO anomalies that correspond to the bright spots observed on full-stack seismic data. Next, the AVO behavior of some of the anomalies has been analyzed in more detail, both *off- and on-structure*. The top-gas sand reflectors of all the analyzed bright spots show decreasing negative amplitudes with increasing offset (e.g. class 4 anomalies). A difference is observed between the modelled AVO responses and the results of the pre-stack data analysis.

Partly due to the large uncertainties in rock properties and in the methods used (e.g. Gassmann's equations), it is very challenging to model the seismic response of these shallow sediments in the pre-stack domain. Since the model parameters are based on the observed combination of seal and reservoir in well F04-01 and the analyzed anomalies lie at different locations and depths with respect to this particular seal-reservoir combination, comparison between the model and the real data itself has a significant uncertainty level due to lateral variations in lithology, temperature and pressure. The outcome of this study shows that, based on the dataset used, the observed AVO behavior on pre-stack seismic data cannot be modelled yet. Whether studying the AVO response of shallow gas accumulations contributes to minimizing the gas saturation uncertainty is therefore still inconclusive.

Contents

List of definitions

Amplitude versus offset (AVO) analysis	Analysis of the amplitude variation with change in distance between shot point and receiver.
Background trend	A trend which has to be identified when the intercept-gradient method is used. The background trend covers all reflectivity points which are assumed to be related to brine-filled sediments.
Biogenic sourcing (biogenic gas)	Natural gas which is created by organisms in shallow sediments.
Bright spot	An amplitude anomaly observed on seismic data that may indicate the presence of hydrocarbons.
Brine	Water which contains more dissolved inorganic salt than typical seawater.
Deterministic model	A particular model whose final results is entirely determined by its initial state and inputs.
Dim spot	A seismic event that shows weak amplitudes which might correlate with the presence of hydrocarbons.
Direct hydrocarbon indicator (DHI)	A type of seismic event that can occur in a reservoir which is hydrocarbon-bearing.
Field	A proven accumulation of hydrocarbons, or other mineral resources, in the subsurface.
Hashin-Shtrikman bounds	These are the tightest bounds possible from a range of composite moduli for a two-phase material.
Henry's law	A chemistry law which states that the mass of a gas which will dissolve into a solution is directly proportional to the partial pressure of that gas above the solution.
Intercept-gradient method	A technique to analyze pre-stack seismic data that may help in identifying hydrocarbon-bearing sediments.
Kelly bushing (KB)	A device that connects the rotary table to the kelly. Depth measurements are commonly referenced to the KB.
Leads	An exploration stage in which interesting features in the subsurface are identified but no hydrocarbons are predicted yet.
Measured depth (MD)	The length of the wellbore along its path. The measured depth is the same as the true vertical depth in case of a vertical well. The measured depth is often referenced to the KB (e.g. MD equals zero at the KB).
Mid-Miocene Unconformity (MMU)	A buried erosional or non-depositional surface which separates two strata of different ages within the Cenozoic era.
Multiple stacked reservoirs	A sequence of reservoirs (e.g. hydrocarbon-filled sand members) and seals (e.g. shale members).
Net-to-gross (N/G)	The fraction reservoir rock within the reservoir (e.g. fraction quartz/fraction shale).
Normal moveout (NMO)	The effect of the distance between source and receiver on the arrival time of a reflection event.
Off-structure	The area within the subsurface next to an identified structure (e.g. an anticlinal structure).

Offset	The horizontal distance from source to receiver in seismic acquisition.
On-structure	The area within the subsurface on top of an identified structure (e.g. anticlinal structure).
Play	An area in which hydrocarbon accumulations or a given type of prospects occur.
Polarity convention	A way to visualize zero-phase seismic data. Two polarity conventions are used in the industry: the US and the EU polarity convention.
Prospects	An exploration stage in which the presence of hydrocarbons is predicted to be economically interesting.
Reservoir	A rock in the subsurface which has sufficient porosity and permeability to accumulate and transmit pore fluids.
Residual gas saturations	Portion of gas that does not move when gas is transported through the rock in normal conditions.
Seal	A relatively impermeable rock that forms a barrier above and around reservoir rock. In this way fluids cannot escape from the reservoir.
Shaley sands	A sand body which also contains a fraction shale.
Signal-to-noise ratio	A measure that compares the level of a desired signal to the amount of background noise. A ratio higher than 1 indicates more signal than noise.
Stacking velocity	The velocity that is used to correct the arrival times of reflection events in the separate traces. After this correction has been applied, the amplitudes should have horizontal alignment and can be stacked.
Stochastic model	A model which yields probability distributions of potential outcomes. Instead of fixed input parameters, random variation is applied to one or more inputs.
The unit constraint	A formula which covers all the constituents of a certain system.
The Upper North Sea Group (NU)	This group comprises all the post-Oligocene sediments in The Netherlands.
Thermogenic sourcing (thermogenic gas)	Natural gas which is created from buried organic material that has been exposed to high temperatures and pressures.
True vertical depth subsea (TVD_{ss})	The absolute vertical distance between a point in the wellbore and the mean sea level.
Tuning thickness	The bed thickness at which two reflection events (top- and bottom-reflectors) become indistinguishable in time due to wave interference.
Two way travel time (TWT)	The elapsed time for a seismic wave to travel from its source to a reflector and subsequently back to a receiver at the Earth's surface.
Well logging	The technique of making a detailed record of the subsurface which has been penetrated by a borehole.

1. Introduction

In the context of this study shallow gas in The Netherlands is defined as gas in unconsolidated formations of Tertiary age under low pressures. These sediments are part of a Late-Cenozoic delta system, often referred to as the Eridanos Delta (Overeem *et al.,* 2001). The origin of the gas may be a *thermogenic* and/or a *biogenic* source. First proof of the existence of shallow gas accumulations in the northern part of the Dutch offshore area has been obtained in the 70's by analyzing full-stack seismic data. Ten years later, some accumulations were proven by wells. Due to the expected sand production and early water breakthrough, as the reservoir consists of unconsolidated sediments, operating companies were hesitant to start developing these *fields*. The first shallow gas producing company in The Netherlands was Chevron with the A12-FA field; production started in 2007. Respectively two and four years later the F02a-B-Pliocene and the B13-FA fields came into production (figure 1.3). Nowadays, several other fields in the northern part of the Dutch offshore are waiting to be developed as sand controlling measures in the three producing fields have appeared to be successful (Chevron, 2009). Mechanical sand controlling methods often deal with the placement of sand screens or gravel packs. Gravel packing, applied in field F02a-B-Pliocene, consists of installing a filter in the well to control the entry of unconsolidated sediments, but still allow the production of hydrocarbons. The other two fields, A12-FA and B13-FA, are developed with expendable sand screens. The success of the currently producing fields and the promising results of a preliminary study that showed significant additional potential (2009, report on www.ebn.nl) encouraged EBN B.V. to look into the *play* in more detail. On top of that, the tax incentive applicable to marginal fields and the widely available 3D seismic data is raising a lot of interest from the E&P industry.

1.1 Geological setting

The shallow gas accumulations in the study area, the F04 and F05 licence blocks in the northern part of the Dutch offshore area, mainly occur above the *Mid-Miocene Unconformity* (MMU). Reservoirs, which are 5-20 m thick, typically consist of unconsolidated sands with varying shale content, sealed by shale layers. The shale layers may be relatively thin (~5 m thick) and still have sufficient capillary seal capacity (Verweij *et al.,* 2014). The depositional setting is a large fluvio-deltaic system. Typical reservoir depths are 300-800 m and the gas is often trapped in anticlinal structures above salt domes. Frequently *multiple stacked reservoirs* are observed (figure 1.1). Gas saturation in the producing reservoirs is ~55%-60% and the predicted recovery factor 50%-75%.

1.2 Seismic signature

There are several shallow *leads* and *prospects* in the Dutch offshore section besides the proven fields (figure 1.3). Leads are defined as features of interest which are not yet subjected to a more detailed study. When the structure is studied in more detail and it is seen as a potential trap that may contain hydrocarbons, it is called a prospect. The shallow leads and prospects in the Dutch North Sea area are recognizable on seismic data as so called *'bright spots*'. Bright spots are amplitude anomalies caused by a relatively high impedance contrast. When changing the water in the pores of a water-bearing sand to hydrocarbons, the shale-sand impedance contrast increases, which results in a brightening event (figure 1.1). Two of the five bright spots in the study area were drilled. Corresponding wells aimed for deeper targets, resulting in incomplete sets of log data for the shallow subsurface.

The challenge in evaluating the shallow play is that seismic brightening already occurs at very low (non-producible) gas saturations or the amplitude anomalies might even have a lithological origin. Gas saturation therefore forms the largest pre-drill subsurface uncertainty and EBN B.V. has started a study in which this issue is addressed. First, a semi-quantitative bright spot characterization scheme was developed to improve the understanding of different types of amplitude anomalies (Van den Boogaard and Hoetz, 2012). Using this scheme the highest ranking leads based on geometrical parameters such as size, depth and amount of stacked layers could be identified. However, since saturation forms the largest uncertainty, the second step would be to get a better grip on the seismic signature of these bright spots in relation to fluid content. This has been done by extending the characterization scheme with *direct hydrocarbon indicators* (DHIs) such as the presence of a flat spot, velocity pull-down, attenuation and gas chimneys (figure 1.1). Also a seismic modelling study was done in which forward modelling of Gassmann's fluid substitution in sandstones was applied using the software of RokDoc (Van den Boogaard *et al*., 2013). Comparison to full-stack seismic data showed that the trends observed can be modelled, but distinguishing low from high gas saturations remains challenging. Moreover, pre-stack seismic data has not yet been investigated in this analysis.

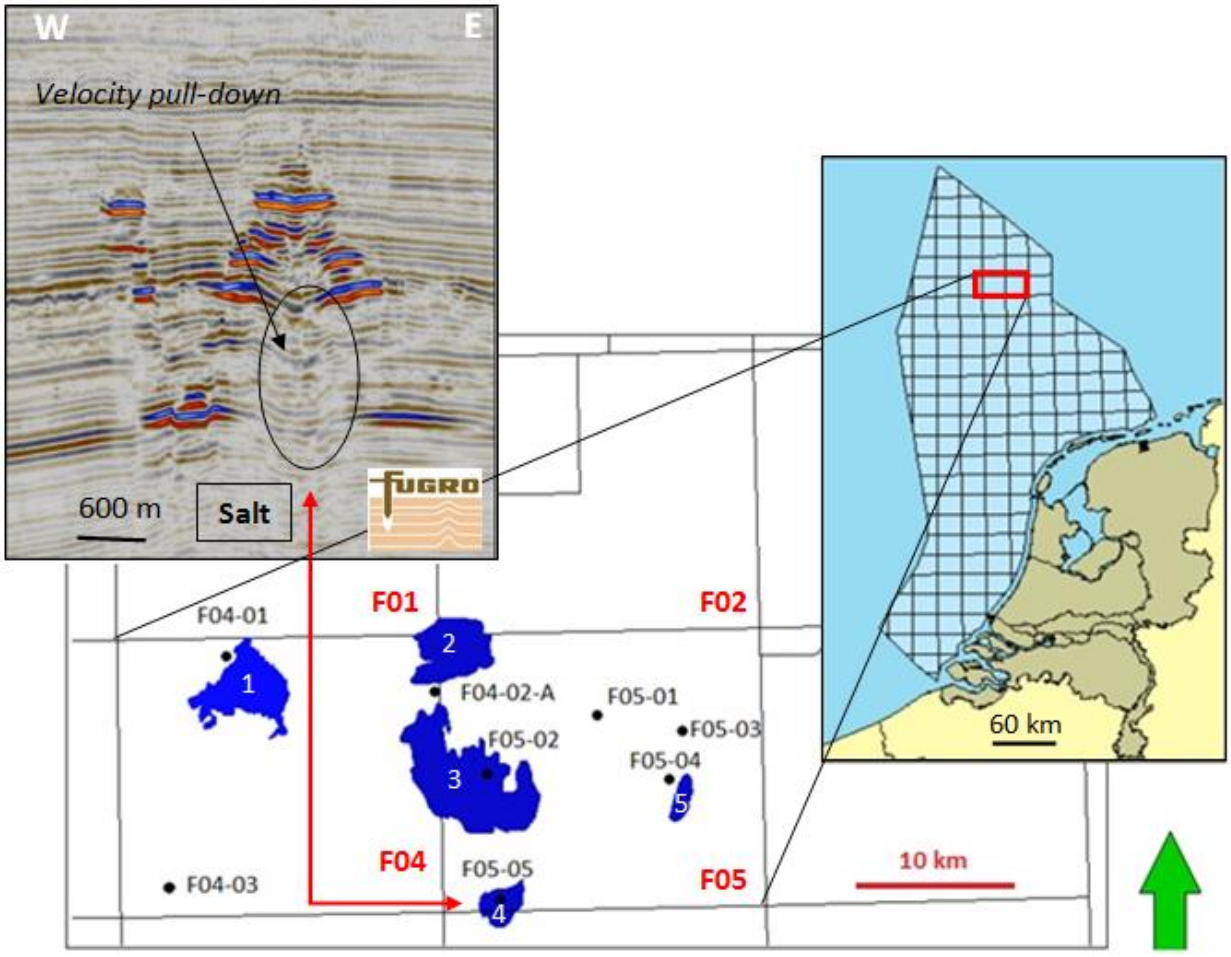

Figure 1.1: Dutch offshore blocks, zoomed in on the study area. The shallow gas leads within the study area are shown in blue. The wells which were drilled in the area of interest are also displayed. The study area comprises the F04 and F05 blocks in the northern part of the Dutch offshore. A seismic section through one of the drilled anomalies is shown in the upper left. Note that both well F05-02 and well F05-05 were drilled through amplitude anomalies.

This work is a follow-up study of the work of Van den Boogaard et al. (2013) and includes *amplitude versus offset* (AVO) analysis of gas-bearing reservoirs in unconsolidated sediments in the study area (figure 1.1) aiming at selecting those anomalies that have highest development potential in terms of gas saturation. In order to find out if AVO analysis helps predicting gas saturations, the AVO behavior of state-of-the-art pre-stack seismic data is compared with a detailed forward modelling study. The study area, the F04 and F05 licence blocks, is chosen due to both the availability of new, high quality, 3D seismic data and the presence of high prospectivity bright spots according to the characterization scheme of Van den Boogaard and Hoetz (2012).

This research has been carried out during an eight-month internship at the Technical Department of EBN B.V., and combines a master thesis and internship. On behalf of the Dutch government, EBN B.V. actively participates in exploration, production, storage and trading natural gas and oil in The Netherlands. The company aims at optimally exploiting the Dutch subsurface. Promoting opportunities, sharing knowledge and facilitating E&P activities are part of the job of EBN employees. The profits generated by these activities are fully transferred to the state, the only shareholder.

1.3 Research question

In this study, the following research question is answered:

- Can the pre-stack seismic response of gas in unconsolidated shallow sediments help in reducing the pre-drill gas saturation uncertainty?

This includes the next sub questions:

- Are the used methods for fluid substitution and reflectivity modelling applicable to the shallow, unconsolidated reservoirs in The Netherlands?
- How does the seismic response, in the pre-stack domain, of a water- versus gas-filled unconsolidated sandstone behave with varying offset?

The first phase of this work includes a petrophysical analysis in order to find suitable parameters which describe the water-bearing shallow reservoirs and overlying seals. Next, Gassmann's fluid substitution method is used to construct new elastic properties corresponding to different gas saturations within the reservoir. The results are used to model the pre-stack seismic response of water-bearing versus gas-bearing unconsolidated reservoirs using the Zoeppritz (1919) equations. In the second phase of this research, pre-stack seismic gathers will be studied. The AVO behavior of state-of-the-art 3D seismic data is compared with the forward modelling results.

1.4 Report structure

The report starts with the theory behind seismic reflection and seismic processing, fluid substitution and AVO techniques (Chapter 2). Reflection seismic is an important tool for the oil and gas industry to search for hydrocarbons and fluid substitution allows one to construct a new set of elastic parameters which relates to a desirable fluid content (e.g. gas). In Chapter 3 the use of full- and angle-stack seismic data is discussed. This section stresses the relevance of using pre-stack data in addition to full-stack seismic data and shows the observations made by analyzing the full- and angle-stack data of the study area. Chapter 4 describes the petrophysical analysis using well data in order to find an appropriate representative water-bearing seal-reservoir combination that can act as a base-case model for the elastic properties. Using these properties, Gassmann's (1951) algorithm for fluid substitution is used to

derive sets of elastic parameters corresponding to different gas saturations in the reservoir. In order to do so, a complete set of elastic properties (density and compressional and shear wave velocity) for the base-case model is required. As complete sets of elastic parameters are often unavailable, rock physics methods can be used. Rock physics provides the link between the physical properties of rocks and their seismic response, and that link may be used to predict any missing data. The derivation of required elastic input parameters and the use of Gassmann's method to predict elastic properties corresponding to various gas saturations, is explained in Chapter 5. The method behind modelling AVO responses stochastically, using the Zoeppritz (1919) equations, and corresponding results are shown in Chapter 6. In Chapter 7, the results of the pre-stack data analysis are given. Subsequently, the learnings are integrated into the discussion (Chapter 8), conclusions (Chapter 9) and recommendations (Chapter 10). Figure 1.2 presents a schematic overview of the workflow that is used in this study.

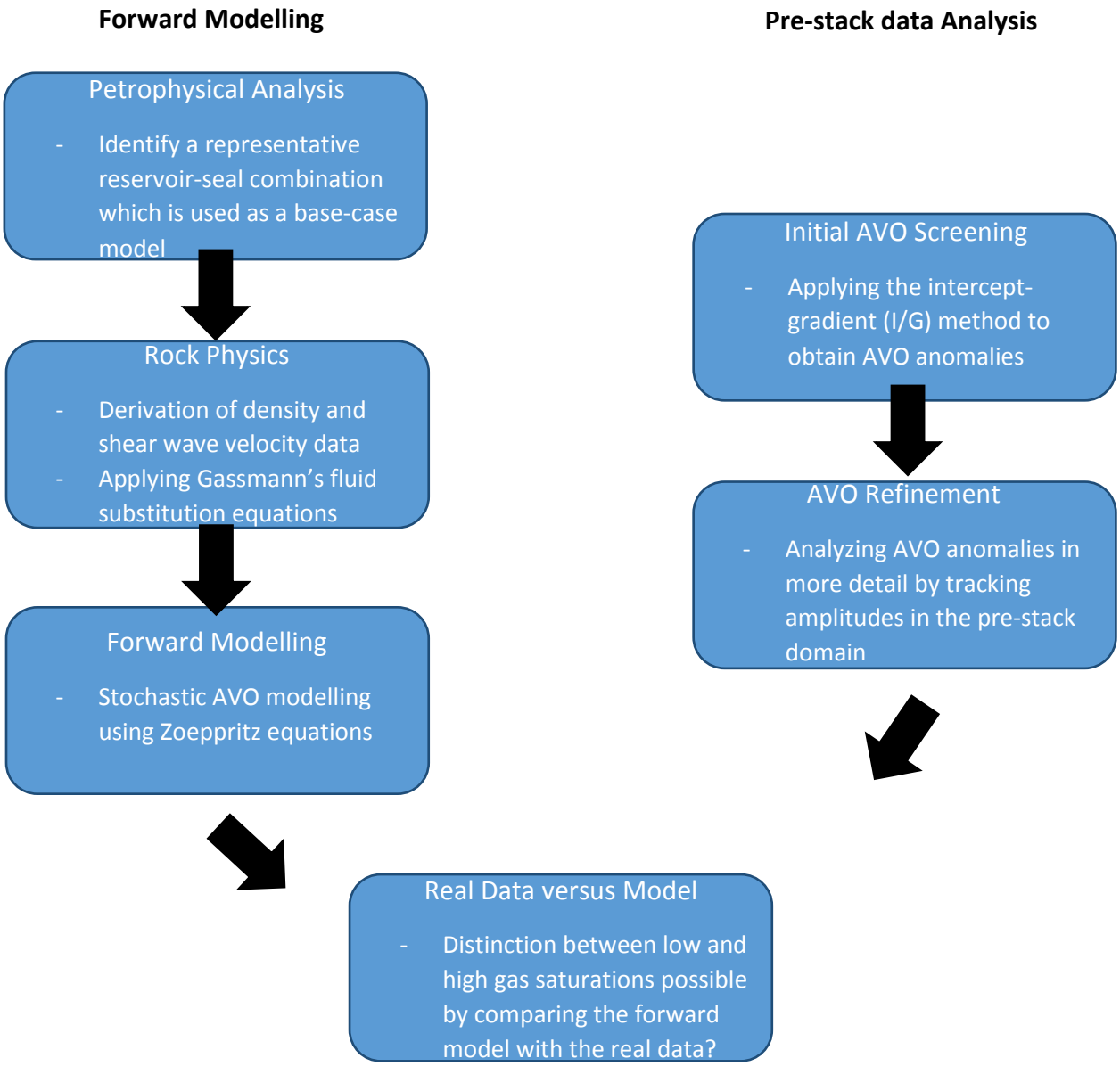

Figure 1.2: The workflow used in this study. The work can be divided into two parts: forward modelling and pre-stack seismic data analysis.

1.5 Data

Both seismic (full- and pre-stack) and well data have been used in this study for respectively (pre-stack) data analysis and forward modelling (figure 1.2). The full- and pre-stack seismic data cube is part of a high quality 3D seismic volume, which is acquired by Fugro in the year 2011. Since this seismic survey covers parts of the D, E and F blocks in the northern part of the Dutch offshore area, this survey is also known as the 'DEF survey'. The study area, which covers approximately 880 km^2, lies completely within the DEF survey. As discussed in more detail in Chapter 3, the seismic data uses the European *polarity convention* where an increasing impedance yields a negative (red) reflector. The pre-stack seismic data covers the entire study area and uses the same polarity convention as the full-stack seismic data. The data is acquired using the common midpoint gather (CMP) method and the receiver spacing equals 12.5 m. Figure 1.3 presents the outline of the DEF survey.

For the forward modelling part (e.g. the petrophysical analysis) public well data is used from the NL Olie- en Gasportaal (NLOG) (www.nlog.nl). According to the Dutch law, all well data (e.g. well logs and reports) acquired after 1 January 2003 should be released after five years. Data which has been obtained before 1 January 2003 should be released after ten years. As seen in figure 1.1, eight wells are present in the study area and all corresponding data is open for public. The types of well data used in this work include well logs (e.g. gamma ray and sonic logs) and well reports.

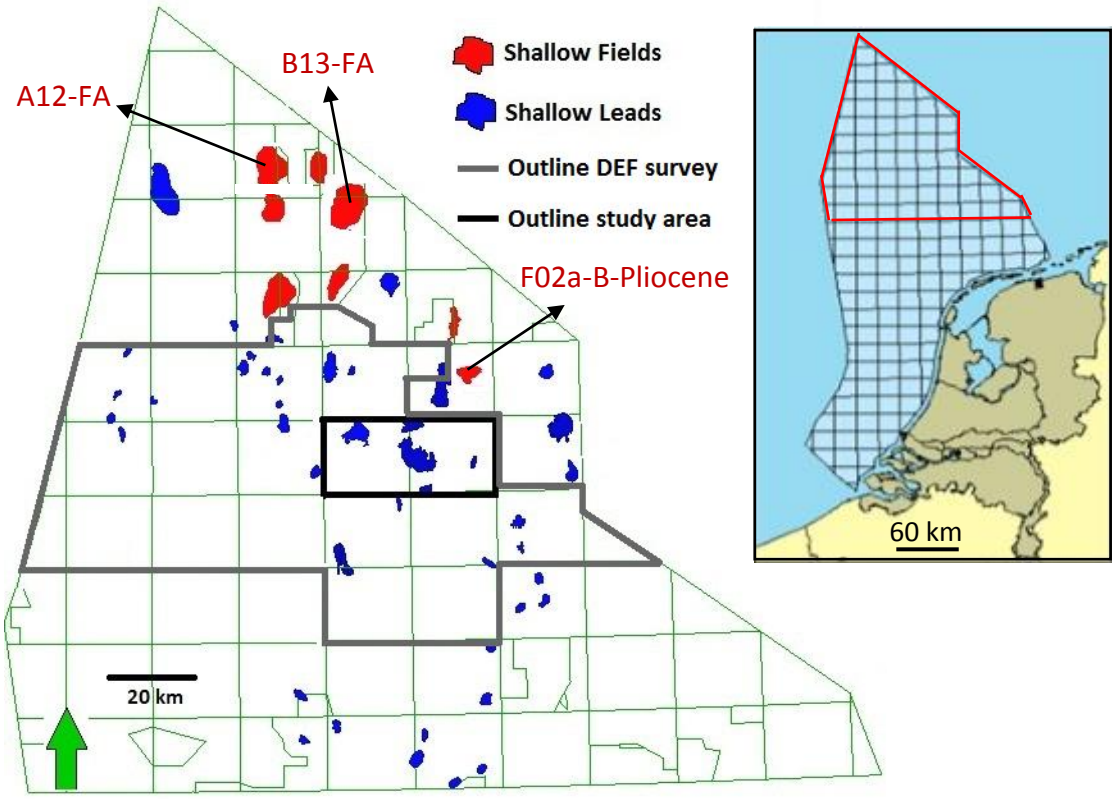

Figure 1.3: Shallow gas fields and leads in the northern part of the Dutch North Sea area, shown in respectively red and blue. Both the outlines of the study area and of the DEF survey, and the three producing shallow fields are displayed. Only the biggest leads (>2km^2) are shown.

1.6 Software

Software packages used in this work include RokDoc, Headwave and Petrel. RokDoc software is used to perform forward modelling and rock physics modelling within unconsolidated reservoirs in the study area. Headwave is used to analyze the pre-stack seismic data cube and for analyzing full-stack seismic data Petrel software has been used.

2. Theoretical background

Since the seismic response of water- and gas-bearing unconsolidated sediments is modelled in this study, and the results are compared with the AVO behavior of state-of-the-art 3D seismic data, it is necessary to understand the theory behind the methods used. This chapter provides the basic theory behind reflection seismic, seismic processing, fluid substitution and AVO analysis.

2.1 Seismic reflection theory

Seismic reflection is a method of exploration geophysics that uses the principles of seismology in order to estimate the properties of the Earth's subsurface from reflected seismic waves (Waters, 1987). When a seismic wave is generated by a controlled seismic source (e.g. a dynamite or an air gun), the receiver (e.g. a geophone or an hydrophone) records the *two way travel time* (TWT) of the wave. By moving the shot point and the receiver, series of reflections of the reflecting layer are generated. On the seismic record, reflections show up as wiggly traces that can be correlated across a profile (Norris *et al.,* 1999). Reflection seismology is the most important tool for 2D/3D mapping of the Earth's subsurface and is extensively used by the oil & gas industry to search for hydrocarbon accumulations. This section describes the construction of the seismic signal, the use of the Zoeppritz (1919) equations, the influence of the fluid content to the seismic signal and the tuning effect.

2.1.1 Construction of the seismic signal

Seismic exploration mainly uses two different types of seismic waves: compressional waves (P-waves), in which the direction of particle motion is in the same direction of wave propagation, and shear waves (S-waves), in which the direction of particle motion is orthogonal to the direction of wave propagation. The speed at which seismic waves are travelling through the Earth is controlled by the medium's elasticity and density. The elasticity of a medium is controlled by its bulk modulus (K) and its shear modulus (μ). The bulk and shear moduli measure respectively the incompressibility of the rock and the resistance to shear deformation (Waters, 1987). These parameters are often expressed in gigapascal (GPa). The compressional and shear wave velocities, in an elastic medium, are given by:

$$V_P = \sqrt{\frac{K + \frac{4}{3}\mu}{\rho}} \tag{1}$$

$$V_S = \sqrt{\frac{\mu}{\rho}} \tag{2}$$

where V_p and V_s are respectively the P-wave and the S-wave velocities. K and μ are the bulk and shear moduli and ρ is the mass density.

For zero-offset traces (source and receiver are on the same position) the reflections are controlled by the contrast in acoustic impedance (Z) since no shear waves are generated. The acoustic impedance is the product of the compressional wave velocity (V_p) and the density (ρ) of the rock. For offset traces, the contrast in elastic impedance determines the reflections (Waters, 1987). A change in lithology (e.g. a shale-sand interface) or a change in pore fluid (e.g. a water-gas contact) results most likely in an acoustic/elastic impedance contrast across that interface. Due to this impedance contrast, a part of the energy of the propagating wave is reflected towards the surface of the Earth and recorded by the

receiver, and a part is transmitted further into the subsurface of the Earth (figure 2.1;2.2). Note that, when the variation in velocity cancels out the change in density, a transition in lithologies does not explicitly results in a reflection event. The reflection coefficient (R), in case of normal incidence, and the transmission coefficient (T) are given by the following equations:

$$R = \frac{Z2 - Z1}{Z2 + Z1} \tag{3}$$

$$T = 1 - R \tag{4}$$

where Z2 (V_{p2}*ρ_2) and Z1 (V_{p1}*ρ_1) are respectively the acoustic impedances of layers 2 and 1, as shown in figures 2.2 and 2.4.

The polarity of the reflected wave depends on the sign of the reflection coefficient (R) and on the convention used (figure 2.9). According to Yilmaz (2001), every reflective interface produces a wavelet and the trace recorded at the surface is basically a sum of all these wavelets. Amplitudes indicate the strength of the recorded reflection event. Figure 2.1 shows a schematic section of how the signal, measured at the surface, is constructed of different reflection events.

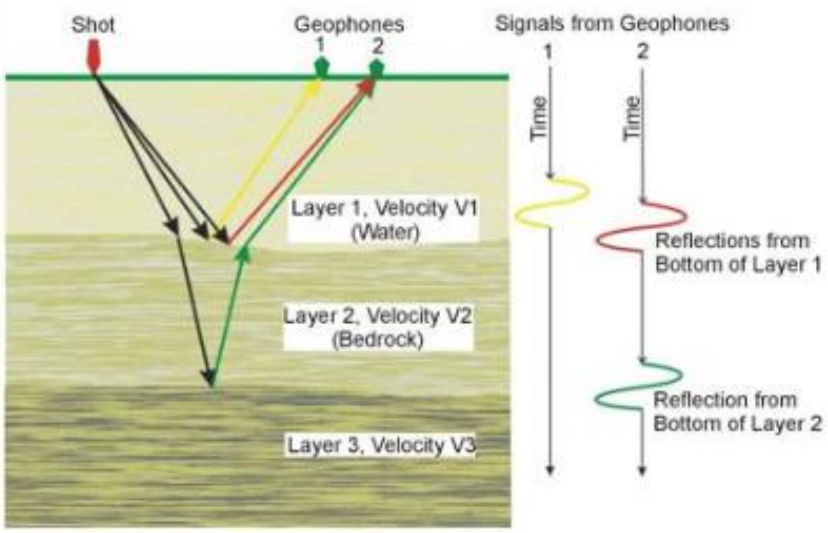

Figure 2.1: The acoustic waves and their travel paths for two geophones. Due to impedance contrasts between the three layers, reflection events occur at the two boundaries. The right hand side shows the seismic signals arriving at the geophones. The signal observed at the surface is just the sum of all the wavelets that are produced by the reflective interfaces (picture from www.cflhd.gov).

At the boundaries between layers 1 and 2 and between layers 2 and 3 in figure 2.1, an impedance contrast results in a reflective and a transmitted part of the seismic energy. The reflected parts travel back to the surface and is recorder by the two geophones. The recorded trace is just the sum of the wavelets that are produced by the reflective interfaces. In practice, many shots are fired as the seismic survey continues along a line. Later, the series of seismic records are processed and assembled to form a seismic section which can be interpreted by geoscientists (Yilmaz, 2001).

2.1.2 Zoeppritz equations

In nonnormal incidence situations, an incident P-wave generates reflected P- and S-waves as well as transmitted P- and S-waves. The corresponding reflection and transmission coefficients depend on the angle of incidence and on the elastic material properties of the two layers (Mavko *et al.,* 1998). Figure 2.2 presents a schematic overview of the waves generated by an incident P-wave. The parameters are related by Snell's law as follows:

$$p = \frac{\sin \theta 1}{V_{p1}} = \frac{\sin \theta 2}{V_{p2}} = \frac{\sin \emptyset 1}{V_{s1}} = \frac{\sin \emptyset 2}{V_{s2}} \tag{5}$$

Where p represents the *ray parameter*.

The complete solution for the reflection coefficients of reflected and transmitted P- and S-waves is given by the Zoeppritz (1919) equations. As these equations do not account for headwave energy, they give only accurate results for angles of incidence up to the critical angle (Sheriff, 1975). Headwaves are produced at the angle of incidence, θ_1, for which the transmitted P-wave propagates along the interface ($\theta_2 = 90°$). The Zoeppritz (1919) equations assume continuity of stress and displacement at the interface.

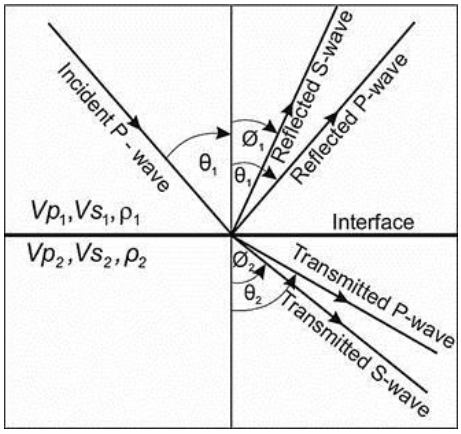

Figure 2.2: Waves generated at an interface by an incident P-wave. When the elastic properties of both the layers are known, Zoeppritz equations can be used to find the relation between the angle of incidence and the reflection coefficient of the reflected P-wave (Mavko et al., 1998).

Since the data used in this study is offshore data, the used hydrophones at the surface only measure the reflected P-wave. Aki and Richards (1980) gave the Zoeppritz (1919) equations in matrix form. They explicitly give the P-to-P reflectivity, the reflection coefficient of the reflected P-wave, (R_{pp}) as follows:

$$R_{PP} = \frac{\left[\left(b\frac{\cos \theta 1}{V_{p1}} - c\frac{\cos \theta 2}{V_{p2}}\right)F - \left(a + d\frac{\cos \theta 1}{V_{p1}}\frac{\cos \emptyset 2}{V_{s2}}\right)Hp^2\right]}{D} \tag{6}$$

where

$$a = \rho_2 (1 - 2 \sin^2 \emptyset 2) - \rho_1 (1 - 2 \sin^2 \emptyset 1) \quad (7)$$

$$b = \rho_2 (1 - 2 \sin^2 \emptyset 2) + 2\rho_1 \sin^2 \emptyset 1 \quad (8)$$

$$c = \rho_1 (1 - 2 \sin^2 \emptyset 1) + 2\rho_2 \sin^2 \emptyset 2 \quad (9)$$

$$d = 2\left(\rho_2 {V_{s2}}^2 - \rho_1 {V_{s1}}^2\right) \quad (10)$$

$$D = EF + GHp^2 \quad (11)$$

$$E = b\frac{\cos \theta 1}{V_{p1}} + c\frac{\cos \theta 2}{V_{p2}} \quad (12)$$

$$F = b\frac{\cos \emptyset 1}{V_{s1}} + c\frac{\cos \emptyset 2}{V_{s2}} \quad (13)$$

$$G = a - d\frac{\cos \theta 1}{V_{p1}}\frac{\cos \emptyset 2}{V_{s2}} \quad (14)$$

$$H = a - d\frac{\cos \theta 2}{V_{p2}}\frac{\cos \emptyset 1}{V_{s1}} \quad (15)$$

When all the elastic parameters (V_p, V_s and ρ) are known for both the seal and the reservoir (for varying gas saturations), the *ray* parameter p, $\emptyset_1$, $\emptyset_2$ and θ_2 can be derived for different values corresponding to the angle of incidence (θ_1) using Snell's law. When all these parameters are known, the above equations could be used to derive the P-to-P reflectivity (R_{pp}) per angle of incidence. The P-to-P reflectivity can be converted to an amplitude using the defined wavelet.

In this study, the Zoeppritz equations are used to model the reflectivity behavior with varying angle of incidence for different gas saturations in the reservoir.

2.1.2.1 Approximations to the Zoeppritz equations

Over the years, a number of approximations to the Zoeppritz equations have been made (e.g. Shuey (1985); Aki and Richards (1980)). These equations are only valid for angles of incidence up to 35° and they assume small contrasts in material properties (Mavko *et al.,* 1998). This section discusses both the Aki and Richards (1980) and Shuey (1985) approximations.

2.1.2.1.1 The Aki and Richards approximation.

Aki and Richards (1980) derive the equation for the reflected P-wave in a form that comprises three terms: a density term (the first term), a P-wave velocity term (the second term) and a third term involving shear-wave velocity. The equation is expressed in terms of contrasts in V_p, V_s and ρ as follows:

$$R_{pp}(\theta) \approx \frac{1}{2}\left(1 - 4p^2{V_s}^2\right)\frac{\Delta\rho}{\rho} + \frac{1}{2\cos^2\theta}\frac{\Delta V_p}{V_p} - 4p^2{V_s}^2\frac{\Delta V_s}{V_s} \quad (16)$$

where

$$p = \frac{\sin\theta 1}{V_{p1}} = \frac{\sin\theta 2}{V_{p2}} \quad (17)$$

$$\theta = \frac{\theta_2 + \theta_1}{2} \quad (18)$$

$$\Delta\rho = \rho_2 - \rho_1 \quad (19)$$

$$\rho = \frac{\rho_2 + \rho_1}{2} \quad (20)$$

$$\Delta V_p = V_{p2} - V_{p1} \quad (21)$$

$$V_p = \frac{V_{p_2} + V_{p_1}}{2} \quad (22)$$

$$\Delta V_S = V_{S2} - V_{S1} \quad (23)$$

$$V_S = \frac{V_{S_2} + V_{S_1}}{2} \quad (24)$$

When all the elastic parameters (V_p, V_s and ρ) are known for both the seal and the reservoir then p and θ_2 can be derived from Snell's law for a certain angle of incidence (θ_1). In this way, R_{pp} values can be obtained using this approximation.

2.1.2.1.2 The Shuey approximation

Shuey (1985) modified the approximation of Aki and Richards (1980) by proposing a polynomial fit for the reflectivity that is accurate for an angle of incidence up to 35° and so expressing the P-to-P reflectivity in terms of the Poisson's ratio, ν, as follows:

$$R_{pp}(\theta_1) \approx \frac{1}{2}\left(\frac{\Delta V_p}{V_p} + \frac{\Delta\rho}{\rho}\right) + \left[G\,\frac{1}{2}\left(\frac{\Delta V_p}{V_p} + \frac{\Delta\rho}{\rho}\right) + \frac{\Delta\nu}{(1-\nu)^2}\right]\sin^2\theta_1 + \frac{1}{2}\frac{\Delta V_p}{V_p}(\tan^2\theta_1 - \sin^2\theta_1) \quad (25)$$

where

$$G = \frac{\frac{\Delta V_p}{V_p}}{\frac{\Delta V_p}{V_p} + \frac{\Delta\rho}{\rho}} - 2\left(1 + \frac{\frac{\Delta V_p}{V_p}}{\frac{\Delta V_p}{V_p} + \frac{\Delta\rho}{\rho}}\right)\left(\frac{1-2\nu}{1-\nu}\right) \quad (26)$$

$$\Delta\nu = \nu_2 - \nu_1 \quad (27)$$

$$\nu = \frac{\nu_2 + \nu_1}{2} \tag{28}$$

and

$$\nu = 0.5\left(\frac{\left(\frac{V_p}{V_S}\right) - 2}{\left(\frac{V_p}{V_S}\right) - 1}\right) \tag{29}$$

In the Shuey equation, the first term is the normal incidence reflection coefficient and is controlled by the contrast in acoustic impedances. The second term, often referred to as the AVO gradient, describes the variation at intermediate offsets. The third term dominates at far offsets near the critical angle.

2.1.2.1.3 Comparison with the Zoeppritz (1919) equations.

Figure 2.3 compares the exact solution of the Zoeppritz equations (thick solid line) with the Aki and Richards approximation (dotted line) and the Shuey approximation (small circles) for the model shown. For this example a simple Ricker 25 Hz wavelet was used. The Aki and Richards and the Shuey approximations overlap each other for the range of angles of incidence displayed. As mentioned before, both approximations describe the Zoeppritz equations accurately up to angles of incidences of 35°.

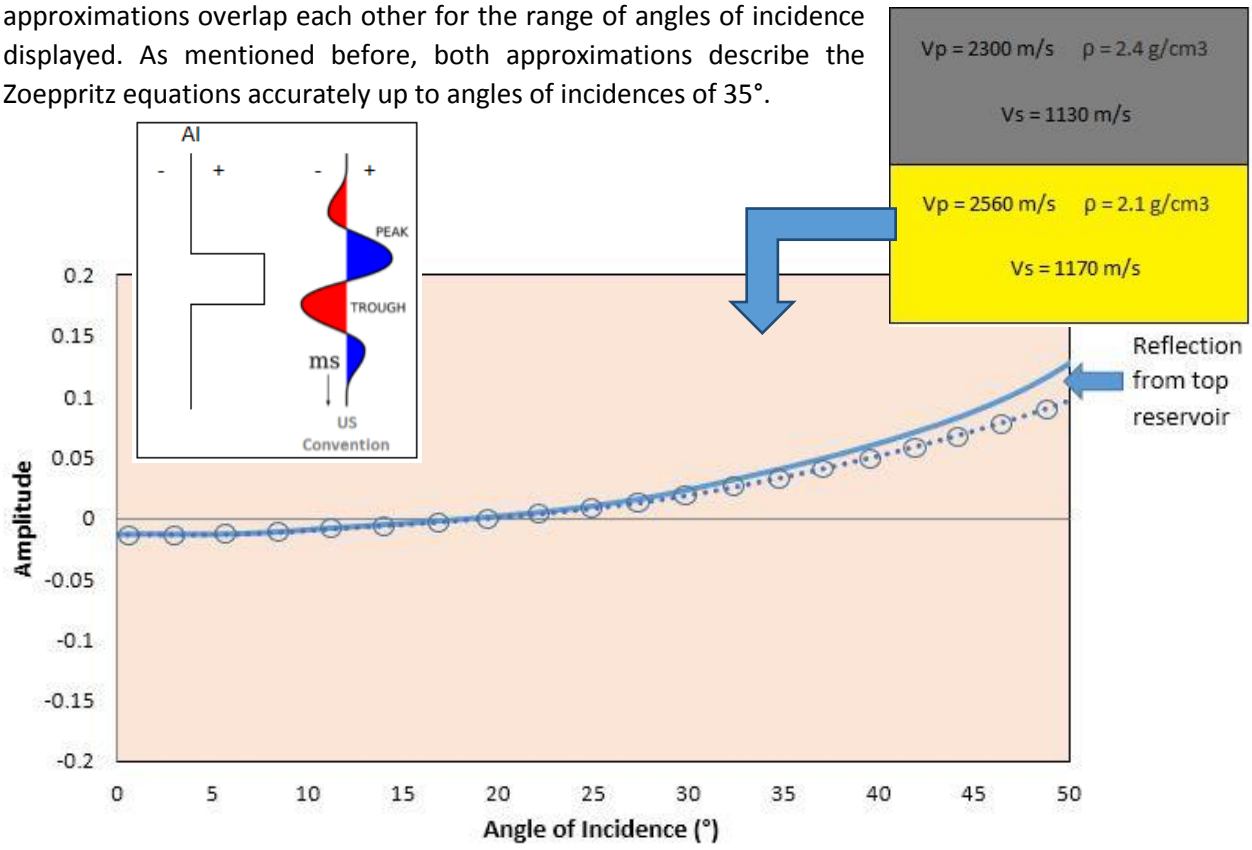

Figure 2.3: Comparison of the exact solution of the Zoeppritz equations (thick solid line) with the Aki and Richards approximation (dotted line) and the Shuey approximation (small circles) for the model shown above. The two approximations overlap each other for the range of angles of incidence displayed here, and they slightly deviate from the exact solution after 35°. A simple Ricker 25 Hz wavelet was used for this purpose. Note that the US polarity convention is used here; increasing impedance yields positive amplitudes.

2.1.3 Seismic signal related to fluid content

The observed seismic signal partly depends on the type of pore fluid. The presence of hydrocarbons in a reservoir, instead of water, normally reduces the impedance since hydrocarbons are relatively light compared to water. The occurrence of hydrocarbons in the subsurface may be recognizable on seismic data by *direct hydrocarbon indicators* (DHIs). The most common DHIs are bright spots, flat spots, dim spots, velocity pull-down, attenuation, gas chimneys and polarity reversals (Swan, 1993). If the water-bearing reservoir has a lower impedance than its surrounding cap rock, the replacement of the pore fluid to hydrocarbons increases the impedance contrast which may result in a bright spot. According to Swan (1993), bright spots occur typically in poorly consolidated reservoirs. Another DHI are flat spots. Flat spots are horizontal reflectors that cross existing stratigraphy and might indicate a hydrocarbon-water level within a reservoir. It can be generated by a contrast between a relatively low impedance of a hydrocarbon-filled rock and a relatively high impedance of a water-saturated rock (assuming the same rock properties). Dim spots typically occur in well consolidated, deep reservoirs which have a higher impedance than its surrounding lithology. It results from a decrease in impedance contrast when hydrocarbons replace *brine* in the saturated zone. Sometimes the reduction of the impedance contrast completely removes the reflection coefficient so no amplitudes are recognizable on seismic data. Polarity reversals might occur where the cap rock has a slightly lower impedance than the reservoir. The hydrocarbons inside the reservoir will reduce its impedance so that it becomes lower than its surroundings, resulting in a reversed sign of the reflection coefficient. Note that a bright spot might also be produced in this scenario (figure 2.4). Figure 2.5 presents the influence of the fluid content on the seismic signal in a simple anticlinal model for the zero-incidence case.

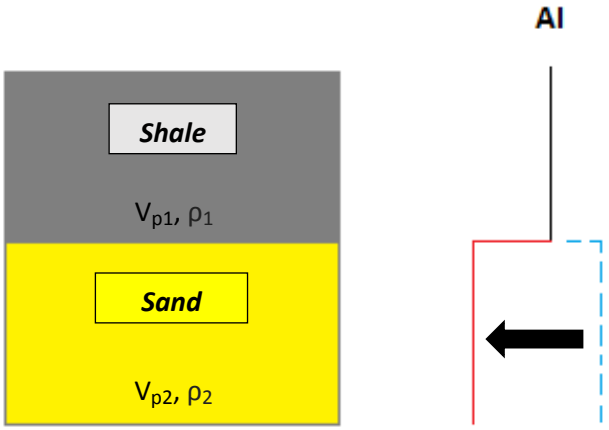

Figure 2.4: A schematic section of the hydrocarbon effect on the acoustic impedance (AI) contrast. The blue dashed line and the red line represent respectively the AI for the water-bearing and gas-bearing sand. In this case, the presence of hydrocarbons results in a polarity reversal and might produce a bright spot. This schematic section assumes zero-offset reflectivity.

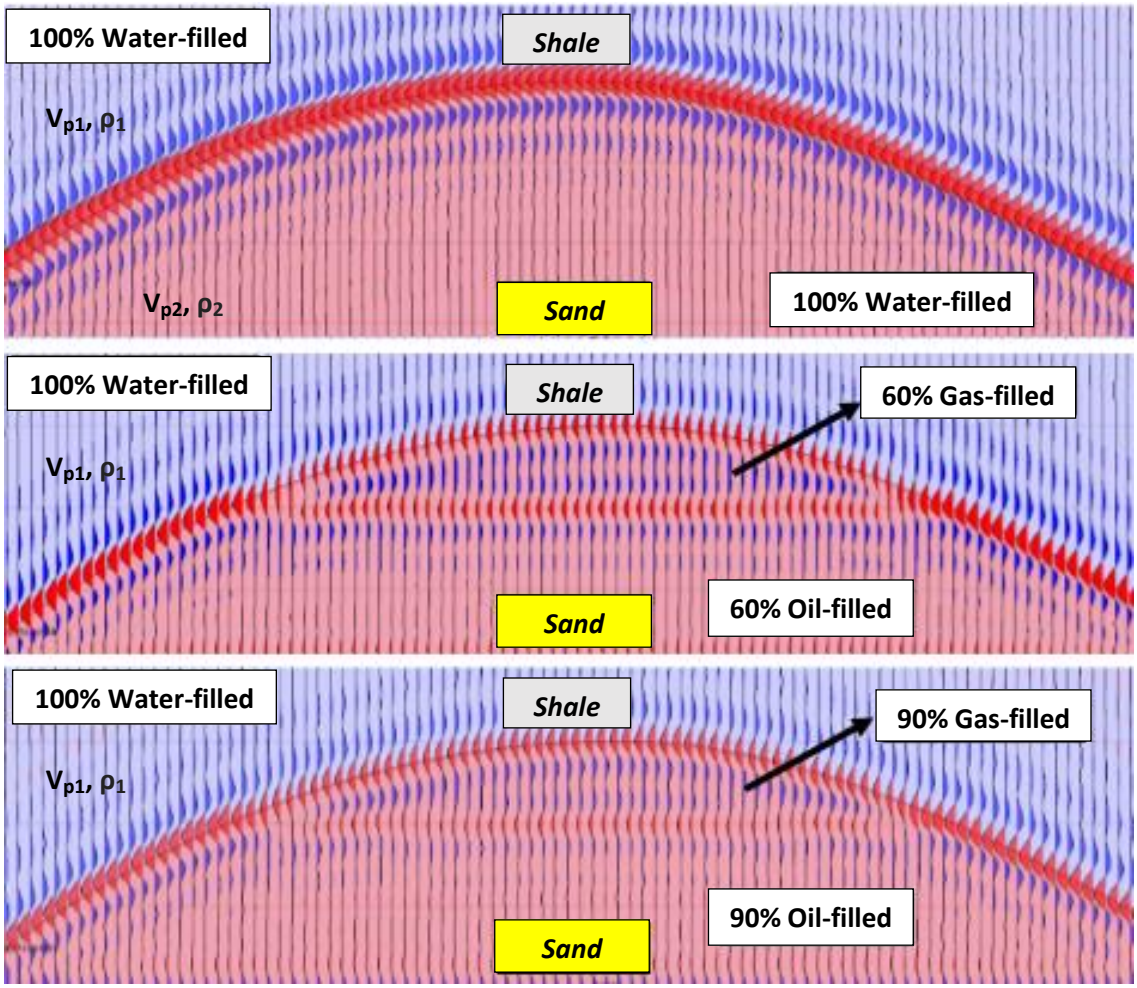

Figure 2.5: The influence of hydrocarbons on the seismic signal. The simple model presents a consolidated reservoir (high impedance) overlain by a relative soft shale formation (low impedance). The water-bearing sand and shale layers contain the following properties: V_{p2} = 2200 m/s, ρ_2 = 2.3 g/cm^3, V_{p1} = 1850 m/s, ρ_1 = 1.9 g/cm^3. An increasing impedance results in a negative amplitude here (EU polarity convention). Both the reservoir and the corresponding cap rock are 100% water-filled in the upper model. The middle picture shows the situation where the reservoir is filled with 60% gas (gas cap) and 60% oil, the other 40% is filled with brine. Hydrocarbon saturations of 90% are used in the model shown below. The cap rock is always 100% water-bearing. Note that a dim spot has been modelled here: the presence of hydrocarbons lowers the impedance contrast. The gas-oil contact represents a low-high impedance transition as gas is relatively light compared to oil. Red amplitudes represent negative magnitudes. RokDoc software has been used in order to construct this model.

2.1.4 Tuning effect

When considering thin reservoirs, it is important to realize that closely-spaced wavelets will interfere, increasing or reducing amplitudes, and sometimes making it impossible to identify two separate beds (Gastaldi *et al*., 1998). First, the amplitude magnitude of the top-reflector increases due to the influence of the side loop of the wave of the bottom-reflector, and later the two waves (of the bottom- and top-reflector) cancel each other out (figure 2.6). At a spacing of less than approximately one-quarter of the wavelength, reflections experience interference and produce a single event of high amplitude, which makes it impossible to determine the bed thickness. At depths greater than one-quarter of the wavelength, the event begins to be resolvable as two separate events: the top- and bottom-reflectors are distinguishable (Robertson and Nogami, 1984). The bed thickness at which two events become indistinguishable in time is called the *tuning thickness*. Figure 2.6 shows an example of a simple tuning wedge model. The tuning thickness in this model equals 14.9 m and corresponds to the maximum magnitude of amplitude of the top-sand reflector, marked by the black circle and the red arrow. This is close to the 19 m which is equal to one-quarter of the wavelength used (25 Hz Ricker wavelet). The tuning thickness is a measure for the vertical seismic resolution.

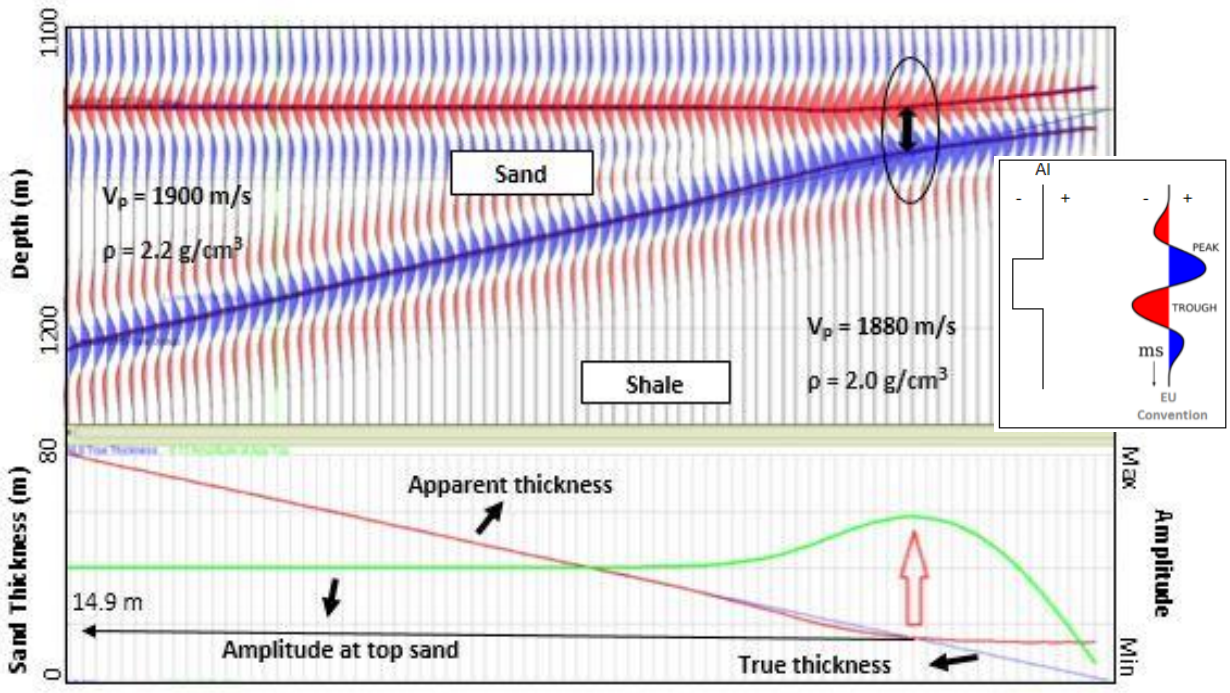

Figure 2.6: A simple tuning wedge model consisting of a sand body (high impedance) and surrounding shale (low impedance). The upper picture presents the synthetic seismic section where red indicates negative amplitudes. The lower graph shows the apparent thickness (derived by picking the top and bottom amplitudes corresponding to the sand body), the true thickness and the magnitude of the amplitude at the top-sand reflector. A 25 Hz Ricker wavelet was used here. The tuning thickness, according to this model, equals 14.9 m (which is the thickness indicated by the black and red arrow in respectively the upper and lower graph). The model was made using RokDoc software. Again, only zero-incidence reflectivities were modelled. The same polarity convention is used here as in figure 2.5: the EU convention; see upper right picture where AI represents the acoustic impedance.

2.2 Seismic processing

The purpose of seismic processing is to manipulate acquired data into an image that can be used by geoscientists to interpret the subsurface of the Earth (Norris *et al.,* 1999). This section briefly describes the type of acquisition that is applied to the dataset which is used in this study and the importance of converting the seismic data to zero-phase.

2.2.1 Acquisition

The reflected waves are recorded at the surface by receivers that detect the motion of the ground (onshore) or pressure changes (offshore), over a fixed time period. On land, the receivers are called geophones while for offshore work hydrophones are used. A response to one single shot is known as a trace. Seismic images consist of sets of multiple traces. The acquisition method applied to the dataset which is used in this work is the common midpoint gather (CMP) method. In this method the traces are sorted such that they approximate one single reflection point in the subsurface (figure 2.7).

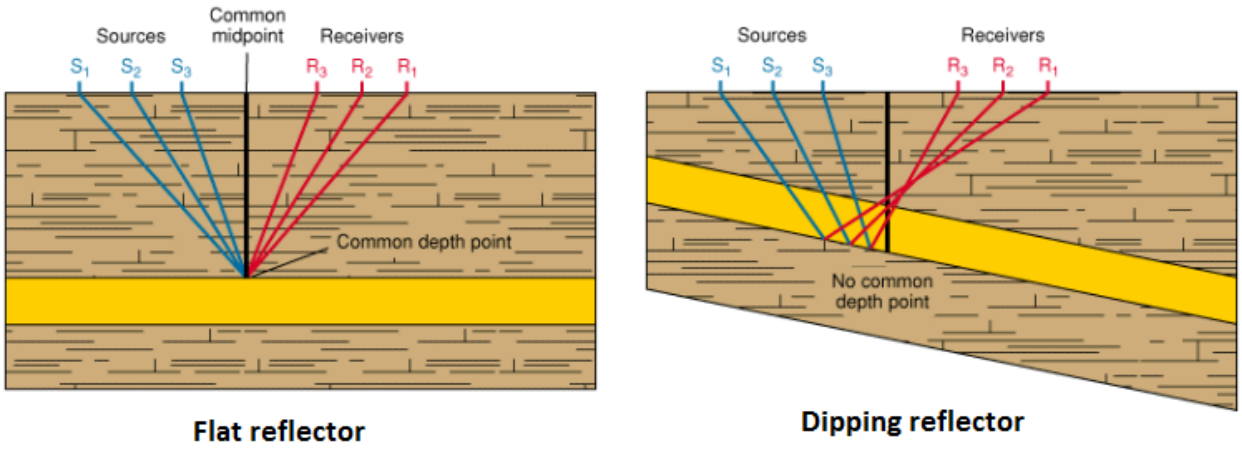

Figure 2.7: The CMP method. A flat reflector in the subsurface results in a common depth point, which is the halfway point in the path from source to flat reflector to receiver. In case of a dipping reflector, the reflection points do not occur directly beneath the common midpoint and no common depth point is observed. In these situations, reflections are geometrically re-located to the location where the event really occurred. This process is called seismic migration (Schlumberger glossary: www.glossary.oilfield.slb.com).

In case of dipping reflectors, seismic migration geometrically relocates the reflection events to the location where the event really occurred (Norris *et al.,* 1999). When the true (migrated) reflector is found, a *normal moveout* (NMO) correction is applied to the dataset. Norris et al. (1999) state that the NMO represents the effect of the separation between source and receiver on the arrival time of a reflection. Normally a reflection arrives first at the receiver nearest the source. The distance between the source and other receivers induces a delay in the arrival time. In order to stack the data, the reflection events should have horizontal alignment. This is often realized by applying a *stacking velocity* to the data (figure 2.8). In the first graph of figure 2.8 a typical NMO curve is presented by the red dotted line. When the offsets and two way travel times are known, it is possible to derive the stacking velocity with the equation shown in figure 2.8 (Castle, 1994). When the reflections are horizontally aligned, the data is stacked in order to increase the *signal-to-noise ratio* (fully stacked seismic data). Stacking of reflections may increase the signal-to-noise ratio, but also information might get lost. Therefore pre-stack data (middle picture in figure 2.8) can be used to obtain more information of the reflector studied by performing AVO analysis. Pre-stack seismic data could also be used to check whether the correct stacking velocity has been applied during seismic processing.

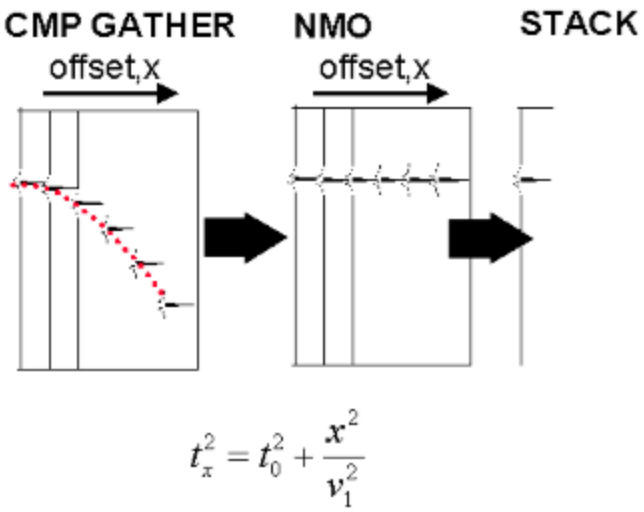

Figure 2.8: NMO correction. The two way travel time is displayed on the vertical axes. If an accurate NMO correction has been applied, reflections will appear as horizontal straight lines. The travel time equation shown represents a flat, horizontal reflector. When the travel times at zero (t_0) and non-zero (t_x) offsets are known, the NMO velocity (V_1) can be derived (Castle, 1994).

2.2.2 Wavelets

The seismic wavelet is the link between seismic data, consisting of seismic traces, on which interpretations are based and the geology that is interpreted (Bacon *et al.,* 2007). Thus, before interpreting the troughs and peaks of a seismic cube, the interpreter needs to establish the type of the wavelet in the data. In other words, the seismic interpreter needs to know the phase (e.g. minimum- or zero-phase) and the polarity (US or EU convention) of the dataset analyzed. A comparison between the zero- and minimum-phase wavelets is shown in figure 2.10.

The preferred output from seismic data processing is a seismic section that represents the reflectivity of the Earth convolved with a zero-phase wavelet, since these wavelets have the greatest resolution for any given bandwidth (Bacon *et al.,* 2007). The zero-phase wavelet is symmetrical, whereas a minimum phase wavelet contains most of the energy near time zero. As most sources (e.g. air guns) produces wavelets that are close to minimum-phase (since an output before time zero is physically impossible), the seismic data is often converted to zero-phase during processing: the deconvolution process. Ideally, deconvolution replaces the original wavelet by a consistent zero-phase wavelet. In this way each reflection occurs at the peak energy and the interpreter can start with interpreting troughs and peaks.

In the industry, often synthetics traces are produced during forward modelling studies. For instance, when the contrast in acoustic impedance across an interface is known in the time domain, this can be converted to a corresponding reflectivity (e.g. equation 3 for normal incidence situations). The next step is to convolve the reflectivity with a certain wavelet which results in a synthetic seismic trace (figure 2.9). Normally noise and multiples are added in order to meet real conditions.

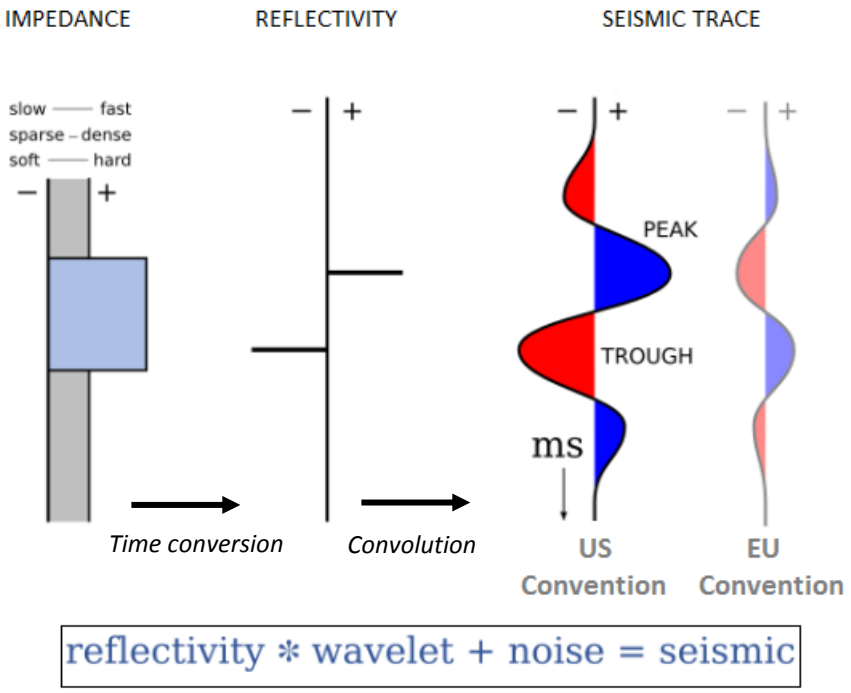

Figure 2.9: A basic model of seismic reflection. The geology is shown on the left: a hard bed surrounded by softer material, resulting in a so-called 'hard-kick' at the top of the fast layer. The contrast in impedance is used to convert to reflectivities. After transformation to the time domain, convolution with a wavelet yields a seismic trace. Note the two ways of displaying a seismic trace: the US and EU polarity convention.

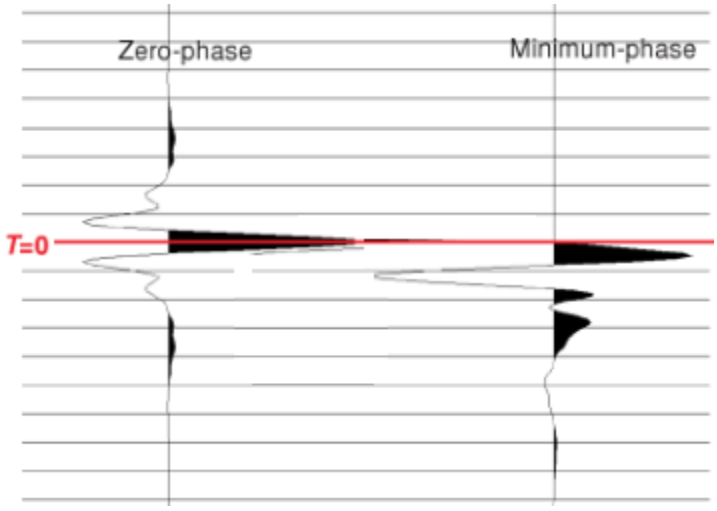

Figure 2.10: Comparison of zero-phase and minimum-phase wavelets. It is desirable that the seismic section, which is interpreted, represents the reflectivity of the Earth convolved with a zero-phase wavelet. However, seismic sources, such as an air gun, cannot be zero-phase since an output before T=0 is not possible. During processing the data is normally converted to zero-phase (Bacon et al., 2007).

2.3 Fluid substitution

In order to check whether AVO analysis can help reducing the pre-drill gas saturation uncertainty, the pre-stack data analysis is compared with a detailed forward model (Chapter 1). To study the AVO response corresponding to known gas saturations, Gassmann's algorithm for fluid substitution is applied to an identified water-bearing reservoir. Given an initial set of elastic properties for a rock with an initial set of fluids, the application of this method results in new sets of elastic parameters (V_p, V_s and ρ) corresponding to different, known, hydrocarbon saturations (Gassmann, 1951). These new elastic properties are required in order to apply the Zoeppritz equations.

2.3.1 Gassmann's equations

Gassmann's theory relates the bulk modulus of a saturated rock (K_{sat}) to the bulk moduli of the porous (dry) rock frame (K_{dry}), the pore fluid (K_{fl}) and the mineral matrix ($K_{mineral}$) as follows:

$$K_{sat} = K_{dry} + \frac{\left(1 - \frac{K_{dry}}{K_{mineral}}\right)^2}{\frac{\phi}{K_{fl}} + \frac{(1-\phi)}{K_{mineral}} - \frac{K_{dry}}{{K_{mineral}}^2}} \tag{30}$$

and

$$\mu_{dry} = \mu_{sat} \tag{31}$$

where ϕ is the porosity, μ_{dry} is the shear modulus of the rock skeleton (the dry rock) and μ_{sat} is the shear modulus of the rock with pore fluid.

When initial P- and S-wave velocities and the mass density is known (e.g. from *well logging*), equations 1 and 2 can be used to compute the corresponding shear ($\mu_{sat}^{initial}$) and bulk moduli ($K_{sat}^{initial}$). Next, estimations of the initial bulk moduli of the mineral matrix and the pore fluid are required. At this stage the bulk modulus of the dry rock frame, for a certain porosity, can be derived by using $K_{sat}^{initial}$ as K_{sat} in equation 30. The same K_{dry} is then used to obtain the saturated bulk modulus after fluid substitution (K_{sat}^{final}), using the new bulk modulus of the desirable pore fluid.

For the derivation of the bulk modulus of the mineral matrix, it is necessary to know the mineral composition of the rock (e.g. from core samples). When the mineral constituents are determined, the bulk modulus of the mineral matrix is calculated using Voigt-Reuss-Hill (VRH) averaging (Hill, 1952):

$$\mathrm{K}_{mineral} = \frac{1}{2}\left(\left[V_{clay}K_{clay} + V_{quartz}K_{quartz}\right] + \left[\frac{V_{clay}}{K_{clay}} + \frac{V_{quartz}}{K_{quartz}}\right]\right) \tag{32}$$

where K_{clay} and K_{quartz} are respectively the bulk moduli of clay and quartz, and V_{clay} and V_{quartz} the volume of clay and quartz as a fraction. Note that in the above equation a mineral model of two constituents is assumed: clay and quartz. The equation can be expanded for more constituents. When working in an effective porosity system (section 5.3.1), shale should be used instead of clay. The density of the mineral matrix ($\rho_{mineral}$) can be calculated by averaging the densities of the individual mineral

constituents with respect to their volume fractions. The mineral matrix does not change during fluid substitution, thus K_{matrix} and ρ_{matrix} remain constant.

Fluid in the pore spaces consists of brine and/or hydrocarbons (oil and/or gas). The bulk modulus (K_{fl}) and density (ρ_{fl}) of the mixed pore fluid phase can be estimated by Wood's equation (Wood, 1955) and the mass balance equation respectively:

$$\frac{1}{K_{fl}} = \frac{WS}{K_{brine}} + \frac{HS}{K_{hyc}} \tag{33}$$

$$\rho_{fl} = WS\rho_{brine} + \mathrm{HS}\rho_{hyc} \tag{34}$$

where WS is the fraction water saturation and HS is the hydrocarbon saturation (= 1-WS), K_{hyc} and ρ_{hyc} are the bulk modulus and density of the hydrocarbons and K_{brine} and ρ_{brine} are respectively the bulk modulus and the density of brine. When the hydrocarbons present consists only of oil, then $K_{hyc} = K_{oil}$ and $\rho_{hyc} = \rho_{oil}$, the same holds for gas. Since in this study only gas is considered, the bulk modulus and density of the hydrocarbons correspond with the properties of gas. The derivation of the bulk modulus and density of both brine and gas is described in Chapter 5.

As mentioned before, K_{dry} can be determined by rewriting Gassmann's equation, equation 30, for K_{dry} and using $K_{sat}^{initial}$ as $K_{sat.}$ The needed initial bulk moduli for the mineral matrix and pore fluid can be derived from the equations above and the initial saturated bulk modulus, $K_{sat}^{initial}$, is often derived from logged V_p, ρ and V_s data. Normally the porosity is obtained during a petrophysical analysis. The bulk modulus of the dry rock frame remains unchanged during fluid substitution.

After K_{dry} has been estimated using Gassmann's equation, the same equation is used to estimate the bulk modulus of the saturated rock after fluid substitution, K_{sat}^{final}, using the new derived $K_{fl,}$ according to the desired hydrocarbon-brine combinations and the initial values for $K_{mineral}$ and K_{dry}. The density of the saturated rock after fluid substitution can be estimated using the principle of a mass balance (equation 71). An estimation for the new seismic velocities, V_p and V_s, is made using the new density, bulk modulus (K_{sat}^{final}) and the initial shear modulus, $\mu_{sat}^{initial}$ (equations 1 and 2). The new obtained set of elastic parameters for a certain reservoir can be used, in combination with the properties of the overlaying seal, in the Zoeppritz equations to model the amplitude behavior of the top-reservoir reflector for varying angles of incidence for different gas saturations in the reservoir. This is also done in this work.

Normally fluid substitution is performed by starting with the initial P- and S-wave velocities measured on rocks saturated with the initial pore fluid by well logs. A problem arises when trying to estimate the alter in V_p during the substitution process and V_s has not been included in the well logging, which is the case prior to fluid substitution in this work. Since the initial V_s value is needed in order to apply Gassmann's algorithm for fluid substitution, a solution has to be found. This is described in Chapter 5. The results of the fluid substitution process are presented in section 5.3.

2.3.2 Assumptions

Gassmann's algorithm for fluid substitution is based on several assumptions. Some assumptions are already mentioned while going over the properties of the rock, fluids, matrix and frame (section 2.3.1). It is very important to keep the following assumptions in mind while performing fluid substitution according to Gassmann's method:

- It is only valid for isotropic, elastic and homogeneous materials. This assumption is violated if the rock is composed of multiple minerals with a large contrast in the elasticity of these minerals, like a sand-shale interval. Gassmann's method often leads to an over-prediction of the fluid effect in laminated sands/shale layers where shale has sufficient sealing capacity, because fluid changes occur (in reality) only in the sand layers and shale laminations are also being modelled (Singleton and Keirstead, 2011).
- The porosity does not change with different saturating fluids. This does not take into account diagenetic processes, such as cementation or dissolution (Mavko *et al.,* 1998).
- It assumes that the pore space is well connected and in pressure equilibrium. In other words, the stresses applied to the rock are of a frequency low enough to allow pressure equilibrium throughout the pore space. This assumption is violated in low-porosity sediments or in *shaley sands* since the bound water in shale cannot move freely (Simm, 2007).
- It is only valid when the assumption is made that there are no chemical interactions between the fluids and the rock frame meaning that the shear modulus remains constant (Mavko *et al.,* 1998).
- It assumes that the bulk moduli of the mineral matrix and the frame do not change with different saturating fluid (Gassmann, 1951).

2.3.3 Approximations to Gassmann's equations

Given the uncertainties and assumptions of Gassmann's equations, one may wish to use one of the approximations as a rough estimate to check the quality of Gassmann's predictions. Approximations are often easier to apply. On the other hand, approximations are more robust as they have fewer parameters. Two approximations to Gassmann's method are given below.

- *Mavko et al. (1995) approximation*. In this approximation the bulk modulus in Gassmann's equations is replaced with the plane-wave modulus (M). The advantage is that the plane-wave modulus is directly calculable from the P-wave velocity and density, thus explicit knowledge of the shear modulus is not required here.
- *Castagna et al. (1993) approximation*. This approximation only requires the compressional wave velocity in brine-saturated sand. The relationship is given as:

  $$V_{gas\ sand} = -0.07{V_{brine\ sand}}^2 + 1.67V_{brine\ sand} - 1.74\ km/s$$

  where $V_{gas\ sand}$ and $V_{brine\ sand}$ represent the P-wave velocity in gas-saturated sand and in brine-saturated sand respectively (in km/s). Empirical V_p-V_s-ρ relationships may be used to predict corresponding shear wave velocity and density.

The less exact methods discussed above are not used in this study as the traditional Gassmann equations remain the theoretical basis for understanding differences between brine- and gas-sand seismic velocities.

2.3.4 Other methods

The most widely-used theory for fluid substitution is Gassmann's theory, but there are more fluid substitution theories and they are divided into two classes: static and squirt limit fluid substitution theories. The static limit theories are based on the assumption that the stresses applied to the rock are of an elastic frequency low enough to allow pressure equilibrium throughout the pore space (Cardona, 2002). Gassmann's equations belong to the static limit theories. The second class of theories, for high frequencies, assumes that fluids in pores of different shape are not allowed to equilibrate pressures among each other, these are squirt limit theories. Brief descriptions of some static and squirt limit theories follow.

2.3.4.1 Static limit theories

A brief description of some static limit theories:

- *The Biot-Gassmann theory (BGT).* Biot's (1956) theory is an extension of the classical Gassmann theory and includes fluid viscosity and the fact that pore fluids can move relative to the frame. Because of the extension, this method shows the possibility of having two P-waves propagating at different velocities through a medium. Although this method is proven to be more accurate than the classic Gassmann theory, the needed parameters are more difficult to derive (Biot, 1956).
- *Brown and Korringa's (1975) theory.* Again, this is an extension of Gassmann's algorithm, but for anisotropic rocks. This theory relates the effective elastic moduli of an anisotropic dry rock to the effective moduli of the same rock containing fluid. The method assumes that all the minerals making up the rock have the same moduli and that the fluid bearing rock is always completely saturated (Mavko *et al.,*1998).

2.3.4.2 Squirt limit theories

A brief description of some squirt limit theories:

- *Mukerji and Mavko's (1994) theory.* The "anisotropic squirt theory" is applicable at high seismic frequencies. It recognizes that when stresses are applied to a saturated anisotropic rock, fluid particles in the narrowest pores are isolated from flow. This formulation can be used to calculate high-frequency saturated rock velocities from dry rock velocities. High seismic frequencies, suited for ultrasonic laboratory measurements, are assumed (Mukerji and Mavko, 1994).
- *Thomsen's (1995) theory.* This method takes into account the effects that changes in the bulk modulus of the saturating fluid have on the anisotropic parameters of a porous rock with aligned cracks (Cardona, 2002). This method also assumes high seismic frequencies.

The fluid substitution theories mentioned above are more difficult to apply with respect to Gassmann's algorithm as the needed input parameters are harder to derive (Mavko *et al.,* 1998). Therefore, as earlier mentioned, Gassmann's method is used in this work.

2.4 AVO analysis

Amplitude versus offset (AVO) analysis makes use of variations in the seismic reflection coefficient as a function of distance between the sources and receivers (figures 2.11 and 2.12). Bill Ostrander (1980) established the idea that seismic AVO might be used to distinguish false bright spots (brightening that is not related to the presence of hydrocarbons) from those associated with hydrocarbons, as he observed a completely different AVO behavior for gas-bearing sediments with respect to brine-saturated sediments. AVO techniques allow geophysicists to get a better understanding of the rock properties of the reservoir (e.g. porosity, density, lithology and fluid content) and to distinguish bright spots related to hydrocarbons from those associated with other geological features (Ostrander, 2006). Nowadays, AVO analysis is widely used in hydrocarbon exploration and fluid parameter analysis (Feng and Bancroft, 2006).

2.4.1 Classification of AVO anomalies

The concept of AVO was already known in the late 70's. In 1982, Rutherford began looking for AVO effects in real data. He studied ways to condition input data in order to observe those effects the best. Rutherford analyzed huge amounts of seismic and well data and summarized his experiences in a paper on AVO classification (Rutherford and Williams, 1989). Rutherford's derived classes of AVO behavior in sandstones are explained in this section. It is important to realize that the classification of AVO anomalies was done using the US polarity convention (figure 2.9) and only top-sand reflectors are considered. The AVO classification for gas sands presents three classes that span the range of AVO effects related to gas sands that are usually encountered in exploration. The three classes are described as follows:

- Class 1: high-impedance sands;
- Class 2: near-zero impedance contrast sands;
- Class 3: low-impedance sands.

2.4.1.1 Class 1 anomalies

If a gas sand, with a high impedance, is encased in low-impedance shale, the top-sand reflection coefficient is positive at zero-offset (using the US polarity convention) and initially decreases in magnitude with increasing offset (thus increasing angle of incidence). Polarity reversals may occur when the angle/offset range availability is sufficient (figure 2.11). Because of the polarity reversal, a dim-spot effect may be seen on full-stack seismic data as stacking the data might cancel out the responses. Hard gas sand formations often correspond to deep, well-consolidated reservoirs.

2.4.1.2 Class 2 anomalies

Gas sands overlain by a shale which have a slightly higher or lower impedance show class 2 responses. The reflection at zero-offset is close to zero and can be positive or negative of magnitude and decreases (positive reflectivities) or increases (negative reflectivities) with increasing offset. These sands can appear as dim spots, bright spots or polarity reversals on stacked seismic data. According to Rutherford and Williams (1989), class 2 anomalies are often seen in moderately compacted and consolidated gas sands.

2.4.1.3 Class 3 anomalies

Class 3 gas sands have typically lower impedances than its surrounding shale layers, resulting in a negative reflection coefficient at zero-offset, which increases with increasing angle of incidence. These sands are the classic bright spot sands seen on stacked seismic data and display high reflectivity at all offsets. Often, relatively shallow unconsolidated gas sands exhibit class 3 anomalies.

Castagna and Swan (1997) extended the classification scheme of Rutherford and Williams (1989) by including a new class: class 4 AVO anomalies.

2.4.1.4 Class 4 anomalies

Castagna and Swan (1997) observed that not all shallow, unconsolidated gas sands show class 3 anomalies. Some of these very unconsolidated sands have large, negative reflection coefficients at zero-offset and decrease slightly with increasing offset. Such anomalies might be observed if the unconsolidated gas sand is situated below a hard cap rock such as a hard shale, siltstone or carbonate.

Figure 2.11 shows the different AVO trends described above and table 2.1 gives a brief overview.

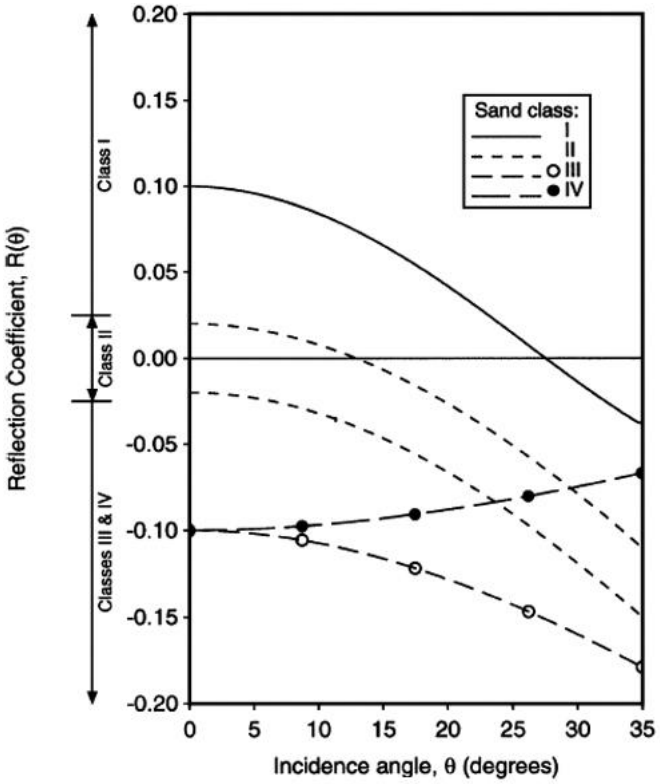

Figure 2.11: The different AVO trends corresponding to the four AVO classes. Note that only top-sand reflections are considered here and that the US polarity convention is used. The plot presents Zoeppritz P-wave reflection coefficients for a range of angles of incidence (Castagna and Swan, 1997).

Since the described AVO classes were derived using the US polarity convention (figure 2.9), this polarity convention is used in the rest of this work.

2.4.2 AVO attributes: The intercept-gradient method

Motivated to make AVO analysis more reliable so that fewer dry holes would be drilled, Foster got involved with AVO studies in 1987 (Foster *et al.,* 1993). As Foster was determined to make AVO analysis less rigid, instead of fitting Zoeppritz (1919) curves to the data, he used the two-term Shuey (1985) approximation and plotted the amplitude against the squared sine of the angle of incidence ($\sin^2\theta$). The two-term Shuey approximation is shown in equation 35 and parameters A and B can be found in section 2.1.2.1.2.

$$R_{pp}(\theta) \approx A + B\sin^2\theta + \cdots \tag{35}$$

In the above equation A denotes the AVO intercept and B the AVO gradient. As can be seen, the two-term approximation of Shuey represents a linear relation. For angles up to 35° this equation is a good approximation of the Zoeppritz equations. The derivation of the AVO intercept and AVO gradient attributes, from real pre-stack seismic data, is shown in figure 2.12.

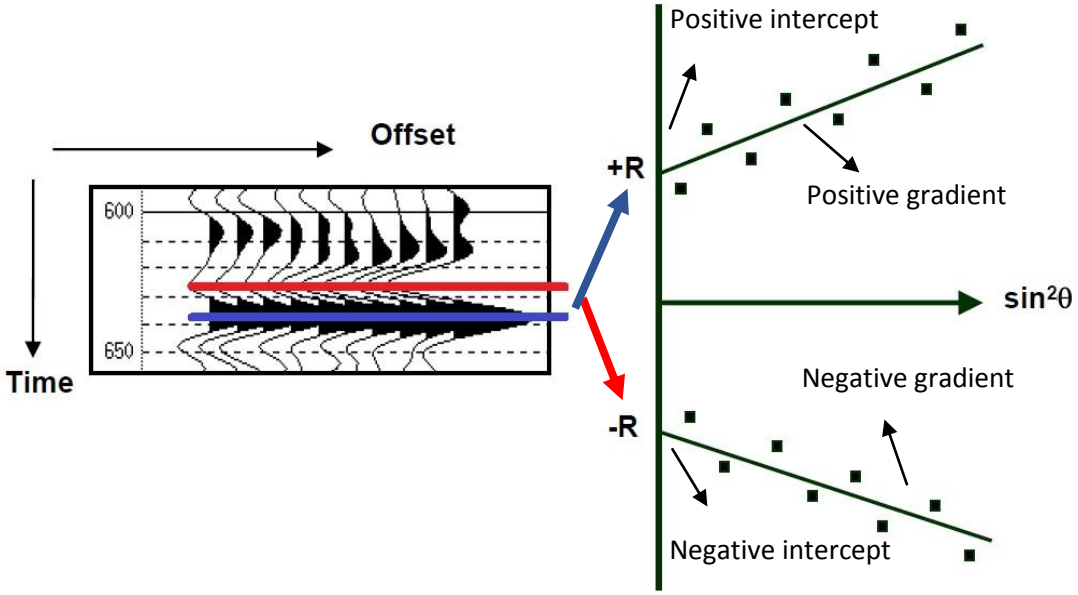

Figure 2.12: From a pre-stack gather to an intercept-gradient combination. In the pre-stack gather on the left, the aligning negative/positive amplitudes are picked and subsequently the magnitudes are plotted against the $\sin^2\theta$ shown in the right figure. After applying a linear fit to the reflectivities, the gradient and intercept values are obtained. Note that one alignment of amplitudes in a pre-stack gather results in one single intercept-gradient combination. These combinations are then plotted in an intercept-gradient cross plot (figure 2.13). R represents the reflectivity.

When the intercept and gradient values are derived, these are plotted in the intercept-gradient cross plot (figure 2.13). Within certain reasonable geological circumstances, the intercept and gradient for brine-saturated sandstones and shale layers follow a well-defined *background trend.* AVO anomalies are seen as deviations from this background trend and may be related to hydrocarbons (especially when they correspond with structural and/or stratigraphic closures) or lithological factors (Castagna and Swan, 1997). In order to obtain a reliable background trend which is easy to interpret, the intercept-gradient analysis has to be applied within limited depth ranges as rock properties vary with depth due to compaction. The cross plot can be divided into four different quadrants as shown in figure 2.13. Table 2.1 summarizes the AVO behavior of the various gas sand classes.

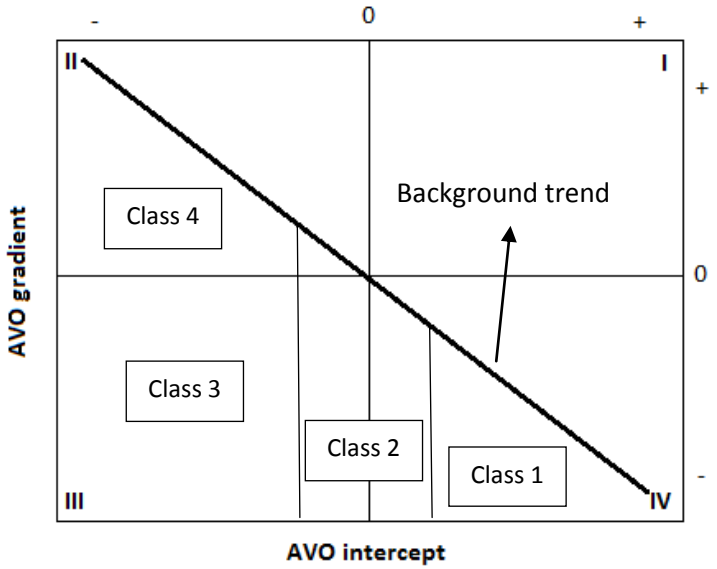

Figure 2.13: The intercept-gradient cross plot. When the two-term Shuey approximation has been applied to a pre-stack seismic cube, within a limited depth and space range, multiple intercept-gradient combinations are obtained and plotted in the cross plot. After identifying the background trend, AVO anomalies can be recognized as deviations from this background trend. The four AVO classes, and a quadrant numbering system, are also displayed. Note that only top-gas sand reflections are considered.

Table 2.1: An overview of the AVO behavior corresponding to the discussed gas sand classes. With amplitude versus offset the variation of the reflection coefficient with increasing offset is meant.

Class	Relative Impedance	Quadrant	Intercept	Gradient	Amplitude vs. Offset
1	Higher than overlying unit	IV	+	-	Decreases
2	Slightly higher or lower than overlying unit	II, III or IV	+ or -	-	Increase or decrease
3	Lower than overlying unit	III	-	-	Increases
4	Lower than overlying unit	II	-	+	Decreases

In this work, the intercept-gradient method is applied to a limited depth range in the study area in order to find the areas of interest (AVO anomalies). When the anomalies are identified, some of the pre-stack gathers are analyzed in more detail. As mentioned earlier, the Zoeppritz equations are used to model the amplitude behavior with varying angle of incidence. Intercept and gradient values, for different gas saturations within the reservoir, are derived by applying a linear fit to the modelled reflection coefficients up to angles of incidence of 35°. The intercept and gradient attributes follow from respectively the intercept and the slope of the regression line (figure 2.12).

2.4.3 AVO analysis: practical examples

AVO analysis may be a powerful tool that gives information about pore fluids and lithology, but it can easily be misinterpreted. Avseth (2005) discusses some practical examples of AVO analysis. A common problem with interpretation of intercept-gradient cross plots is that multiple combinations of rock properties might result in the same intercept-gradient combination. Thus, as a result of natural variation in geological features and fluid properties, one particular geological scenario may cover a relatively large area in the intercept-gradient cross plot instead of one unique point. This is one reason why AVO analysis, by using the intercept-gradient method, can give erroneous results. Another reason is the fact that these cross plots, based on pre-stack data analysis, are often affected by noise in the data (after all, seismic data is stacked in order to increase the signal-to-noise ratio). Below 2 case examples are shown which were described by Avseth (2005).

2.4.3.1 The Glitne Field in the North Sea

In case of the Glitne field, which lies in the Norwegian sector of the North Sea, hydrocarbons were successfully predicted using the intercept-gradient cross plot. Oil was predicted in the lobe channels and it has been confirmed by drilling. The reservoir consists of separate sand sheets of deep-marine fan deposits of Paleocene age (often referred to as the Lower Tertiary). Statoil owns most of the interest of the field and the field went into production in 2001.

2.4.3.2 The Grane area in the North Sea

The Grane area, also located in the Norwegian sector of the North Sea, is an example where AVO analysis was not successful. In this case AVO analysis indicated the presence of oil bearing reservoir sands next to the already proven main reservoir, but the model neglected other lithologies than sands and shale. In fact, instead of oil saturated sands, tuff layers were encountered. Avseth (2005) states that it was not the methodology that failed here, but insufficient information about the geology.

Based on the described case examples, it is concluded that knowledge about the local geology is extremely important in this work. Sufficient knowledge about the local geology yields a complete overview of the lithologies that are present. In this way, no lithologies are neglected by the model.

3. Full- and angle-stack data analysis

Before analyzing and modelling amplitudes in the pre-stack domain, attention is paid to observations which can be made by analyzing full- and angle-stack seismic data. This chapter gives an overview of the observations made using full- and angle-stack data and it stresses the relevance of using pre-stack seismic data next to full-stack data.

3.1 Observations on full-stack data and drilled anomalies

This section describes both the bright spot observations and the polarity identification using full-stack seismic data. Also the well results, regarding gas readings, of the drilled anomalies within the study area are discussed in this part.

3.1.1 Bright spots

Five shallow amplitude anomalies, or bright spots, were identified in the study area on 3D seismic data (figure 1.1). As mentioned before, a semi-quantitative bright spot characterization scheme was developed by Van den Boogaard and Hoetz (2012) in order to improve the understanding of different types of amplitude anomalies. This characterization scheme identified the highest ranking leads based on geometrical parameters such as size, depth and the amount of stacked layers. This scheme is extended by Van den Boogaard and Hoetz (2014) by the addition of seismic characterizations (e.g. DHIs). An example for an imaginary lead X is shown in figure 3.1.

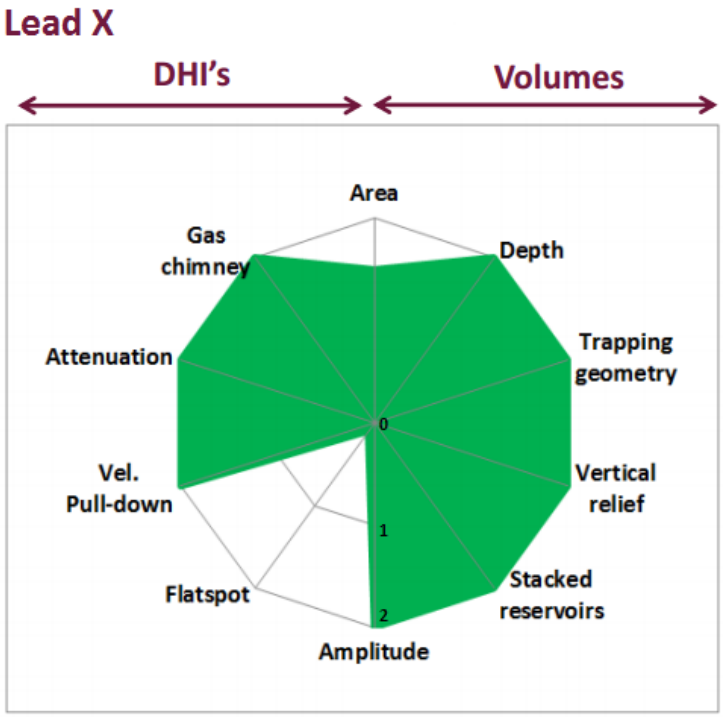

Figure 3.1: The extended characterization scheme of Van den Boogaard and Hoetz (2014) uses various geometrical and seismic features in order to identify the highest ranking leads. The numbers 0-2 represent the degree to which the parameters are present.

The extended characterization scheme identified the following three different types of bright spots with increasing prospectivity: bright spots which contain stratigraphic traps, bright spots with fault dip

closures (FDC) (e.g. the F02a-B-Pliocene field) and bright spots with 4-way dip closures (4WDC) (e.g. the A12-FA field). FDC and 4WDC are the two types of bright spots which have the highest prospectivity since they are analogue to producing fields. Besides the three main types of bright spots, every lead has a characterization as in figure 3.1. In this work, only the main types of bright spots are considered.

The amplitude anomalies in the study area are divided into FDC and 4WDC bright spots based on their geometrical characterizations (table 3.1 and appendix A). The five anomalies can be further divided into two types:

1- Bright spots without a polarity reversal at the edge of the anomaly.
2- Bright spots with a polarity reversal at the edge of the anomaly.

The polarity reversals seen between the assumed water- and gas-bearing sediments is controlled by the effect of hydrocarbons on the seismic signal (figure 2.4, section 2.1.3). The rock properties determine whether a polarity reversal is observed. The type of bright spot (FDC or 4WDC) is extended by adding the numbers 1 or 2.

Table 3.1 gives an overview of the anomaly classification using the anomaly numbers shown in figure 1.1.

Table 3.1: Anomaly classification within the study area using the bright spot types derived in the characterization scheme of Van den Boogaard and Hoetz (2014).

Anomaly number	Prospect/Lead	Type of bright spot	Multiple stacked reservoirs (number)
1	F04-P1	4WDC-1	Yes (3)
2	Legacy	FDC-2	Yes (2)
3	F04/F05-P1	FDC-2	Yes (4)
4	F05/F08-P1	FDC-2	Yes (5)
5	F05-P1	FDC-2	Yes (2)

Appendix A presents seismic sections through the five anomalies. All the potential gas accumulations occur above the Mid-Miocene Unconformity and the gas is often trapped in anticlinal structures above salt domes. Occasionally, velocity pull-down effects are seen (figure 3.2).

3.1.2 Drilled anomalies: well results

A seismic line through amplitude anomaly 4, lead F05/F08-P1, is presented in figure 3.2. The bright spot was drilled by well F05-05. The corresponding final geological evaluation report states that it is apparent that the gas readings over the predicted shallow gas accumulations are relatively low (~0.1%-1% methane gas) and contain minor quantities of gasses heavier than methane. However, the exact gas saturation remains unknown as the mud weight, which was used during drilling, may be large enough to suppress the gas readings.

Figure 3.3 presents a seismic section through anomaly 3, lead F04/F05-P1, which was drilled by well F05-02. The final geological evaluation report belonging to well F05-02 concludes that no hydrocarbon shows were encountered in the drilled shallow amplitude anomalies. However, gas readings of 10%-12% methane gas were recorded in these anomalies. Again, this information shows that there is gas present within these shallow formations, but the exact saturation remains unknown.

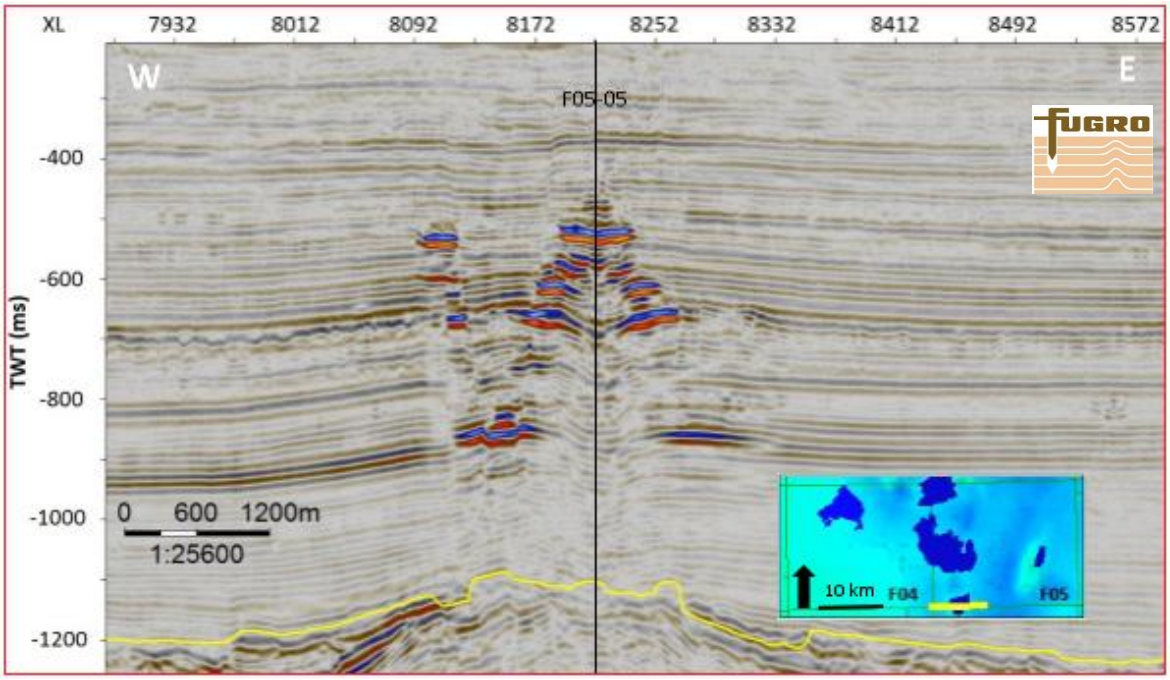

Figure 3.2: A seismic line through lead F05/F08-P1 (anomaly 4). The yellow line represents the Mid-Miocene Unconformity (MMU). Note the multiple stacked reservoirs and the pull-down effect. The anomaly is directly located above a salt dome. The lower right figure presents the location of the line within the study area; colors specify the depth to the MMU where blue means greater depths. The location of well F05-05 is also shown. An enlarged version of this section can be found in appendix A.

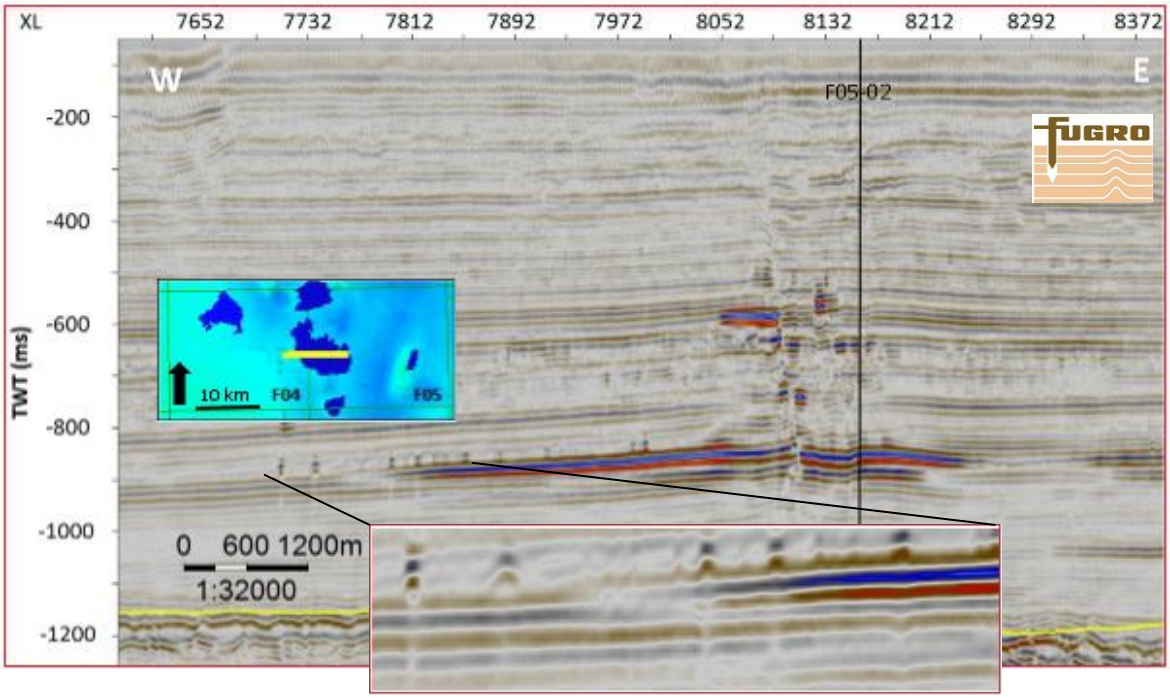

Figure 3.3: Seismic line through lead F04/F05-P1 (anomaly 3). The yellow line represents the Mid-Miocene Unconformity (MMU). Note the multiple stacked reservoirs and the polarity reversal. The left figure presents the location of the line within the study area: colors specify the depth to the MMU where blue represent greater depths. The location of well F05-02 is also shown. An enlarged version of this section can be found in appendix A.

3.1.3 Seismic polarity

As mentioned before, there are two frequently used polarity conventions in the industry: the EU and the US polarity conventions (figure 2.9). Knowledge of the polarity in the seismic data is required in order to keep the polarity convention, in both the modelling work and in the results of the pre-stack data analysis, the same. Figure 3.4 presents a seismic line within the study area with both the Top Chalk and Base Chalk horizons indicated. The strong amplitudes corresponding to these two surfaces are used to identify the polarity scheme of the seismic data.

The Top Chalk horizon represents a relatively high negative amplitude reflector, which results from the transition from soft clays of Tertiary age to hard chalk (an increase in impedance). The Base Chalk surface shows in turn high positive amplitudes, resulting from a shift from faster chalk to softer clastic sediments (a decrease in impedance).

From the above it can be concluded that the polarity norm used in the seismic data (both pre- and full-stack) implies a trough, presented in red, on increasing impedance: the EU polarity convention.

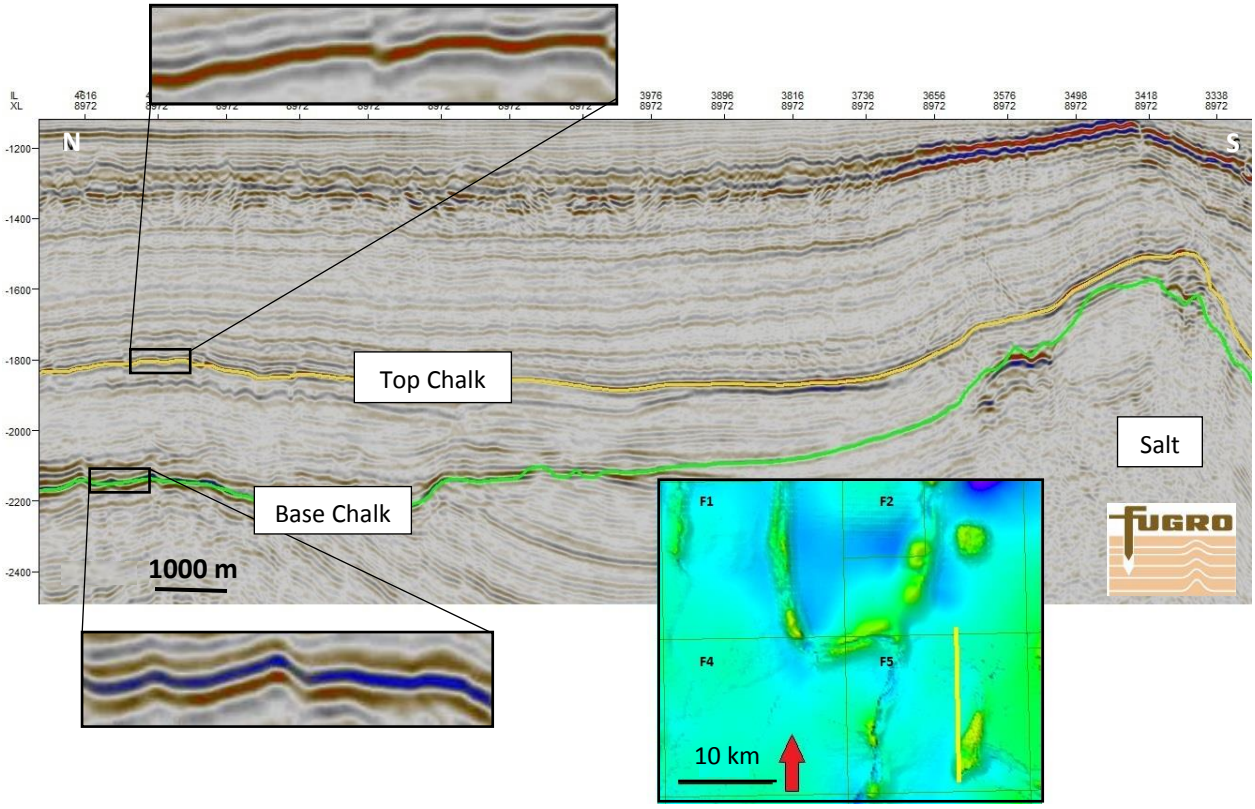

Figure 3.4: Above: a seismic line within the study area. Both the Top Chalk and Base Chalk horizons are displayed. Depth is in TWT (ms). Below: the location of the seismic section within the study area marked by the yellow line. Colors represent depth to Top Chalk: blue means great depths. Note the salt structures within the study area.

As the Top Chalk horizon presents a relatively sharp shift from Tertiary sediments to chalk formations, and the wavelet (which is produced due to this impedance contrast) is assumed to be not influenced by interference with other wavelets/reflective interfaces, this response may be used to identify the used wavelet in the seismic data. A symmetrical seismic response is observed at the Top Chalk horizon (figure

3.4): a clear negative response in red surrounded by positive amplitudes of relatively low magnitude. This behavior is typical for the zero-phase wavelet, which contains symmetrical side lobes (figure 2.10).

Since the AVO classes, which were mentioned in section 2.4.1, are based on the US polarity convention, the US polarity norm is the convention that is used in this study; the analyzed pre-stack data is converted to this polarity norm.

3.2 Full-stack versus pre-stack seismic data

As was stated in section 2.2.1, the pre-stack seismic gathers are stacked in order to increase the signal-to-noise ratio. A disadvantage of stacking amplitudes is that some information, which might be present in the pre-stack domain, is lost. Full-stack seismic data is often the type of data that is used in the industry (e.g. for interpretation purposes). Drilling high-amplitude events seen on full-stack data resulted in significant discoveries of hydrocarbon accumulations in the past (Chopra and Marfurt, 2007). However, not all bright spots are associated with hydrocarbons. Pre-stack data analysis (AVO analysis) may be useful to distinguish between false bright spots (e.g. bright reflections as a result of abnormally high- or low-velocity layers that are not associated with hydrocarbons) and bright spots related to the presence of hydrocarbons.

3.3 Observations on angle-stack data

Near-mid-far angle stacks are common types of seismic datasets available for interpreters. If pre-stack data is not available, or in noisy areas, these datasets are key inputs for calculating AVO attributes such as the intercept and gradient (Nam and Fink, 2008). Differences between near-angle and far-angle stacks may also be used to estimate the amount of velocity pull-down due to the presence of gas. In this work, near-angle data comprises angles of incidence from 0° to 13° and the far-angle stack contains incidence angles from 45° to 55°. This section describes the use of angle-stack seismic data as a pull-down indicator and as an input for calculating the intercept and gradient for AVO purposes.

3.3.1 Angle-stack seismic data as a pull-down indicator

Leakage of gas from a poorly sealed gas accumulation (e.g. a gas chimney) causes lower velocities in the overlying rocks. Velocity pull-downs occur when a shallow layer or feature with a relatively low seismic velocity (such as a gas chimney) is surrounded by rock with higher seismic velocities. In the time domain, this seismic phenomenon causes what appears to be a structural low beneath it. If only the near traces travel through the gas-saturated zone, then travel time differences between near- and far-angle stacks may indicate the amount of pull-down (figures 3.5, 3.6 and 3.7). The use of angle-stack data in order to estimate the amount of velocity pull-down has been studied for a seismic section through lead F05-P1.

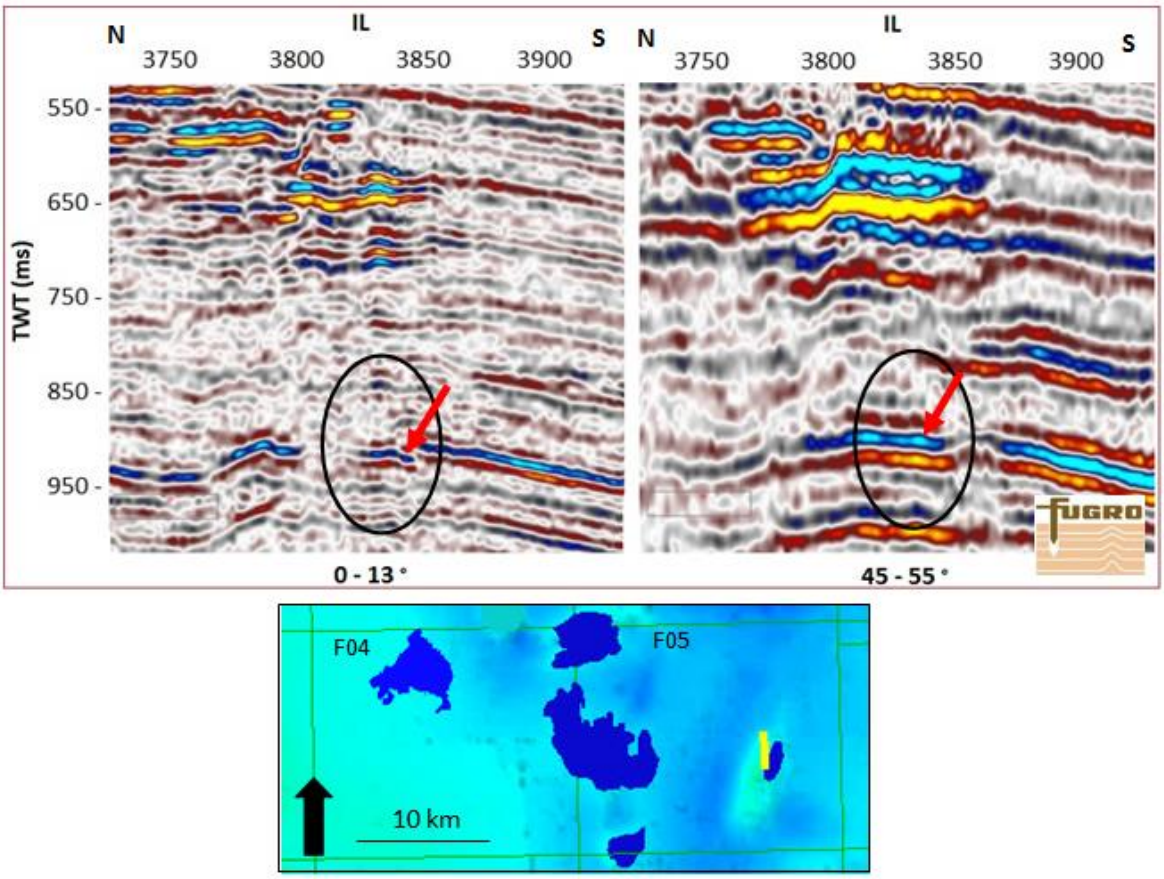

Figure 3.5: Near-angle stack versus far-angle stack seismic data for a seismic section through lead F05-P1 (anomaly 5). Note the relative bright reflectors in the far-angle stack marked by the black circle and the absence of them in the near-angle stack data. Indications of what appears to be a structural low are observed in the circle in the near-angle stack seismic data. The same amplitude scale as in figure 3.7 has been used. Colors in the lower picture represent depths to the Mid-Miocene Unconformity where blue means greater depths.

Figure 3.5 compares near-angle stack (0°-13°) with far-angle stack (45°-55°) data for a seismic section through lead F05-P1. The poor data quality in the near-angle stack, marked by the black circle in figure 3.5, may be the result of wave propagation through a gas-filled overburden. Moreover, it is possible that the far traces propagate along and beneath the gas present in the overburden. In this case, the travel time difference between near- and far-stacks may be an indicative for the amount of velocity pull-down. Figure 3.6 presents a schematic sketch of the described situation.

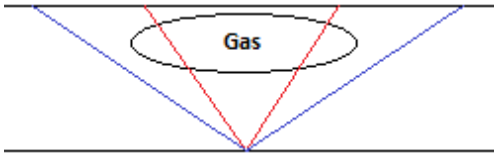

Figure 3.6: A schematic sketch of the described situation. The near trace (in red) propagates through the gas accumulation and corresponding signal is therefore disturbed. Differences between near- and far-stacks may indicate the amount of pull-down.

Figure 3.7 shows that the far traces arrive relatively faster than the near traces. This may be another indicator for the presence of gas in the overburden: the near traces might be slowed down due to the propagation through overlying gas (figure 3.6).

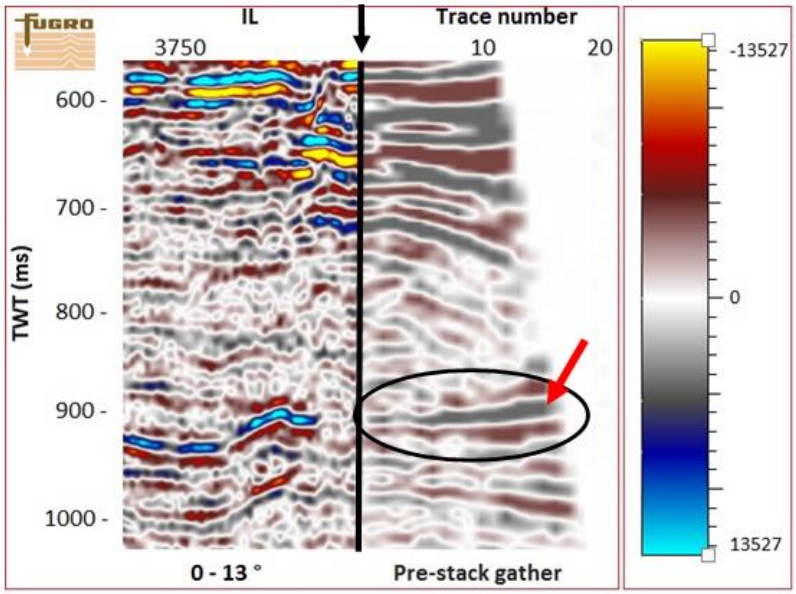

Figure 3.7: Left: near-angle stack data for a part of the section shown in figure 3.5. Right: the pre-stack gather which belongs to the black line on near-angle stack data highlighted by the black arrow. Note the relative fast arrival of the far traces at a depth of ~900 ms.

Figures 3.5 and 3.7 show differences in travel time between the two angle-stacks for a reflector below lead F05-P1. Although there are many reasons for the differences in travel time observed between near- and far-angle stack seismic data (e.g. wrong stacking velocity used during processing and other geological features that cause a relatively slow/fast layer in the subsurface), the travel time difference between near- and far-angle stack data might be a measure for the amount of pull-down in milliseconds;

this is assumed in the following. Figure 3.8 presents the difference between far-angle stack and near angle-stack seismic data in TWT (ms). This figure has been derived by subtracting a near-angle stack horizon (picked through the blue reflector marked by the red arrow in figures 3.5 and 3.7) from the corresponding far-angle stack horizon.

As the synclinal structure in figure 3.8 is located approximately beneath the bright spot at ~650 ms (figure 3.5), this observation might represent the amount of velocity pull-down due to the gas accumulation in the overlying sediments. Figure 3.8 indicates a maximum velocity pull-down of 30 ms (TWT).

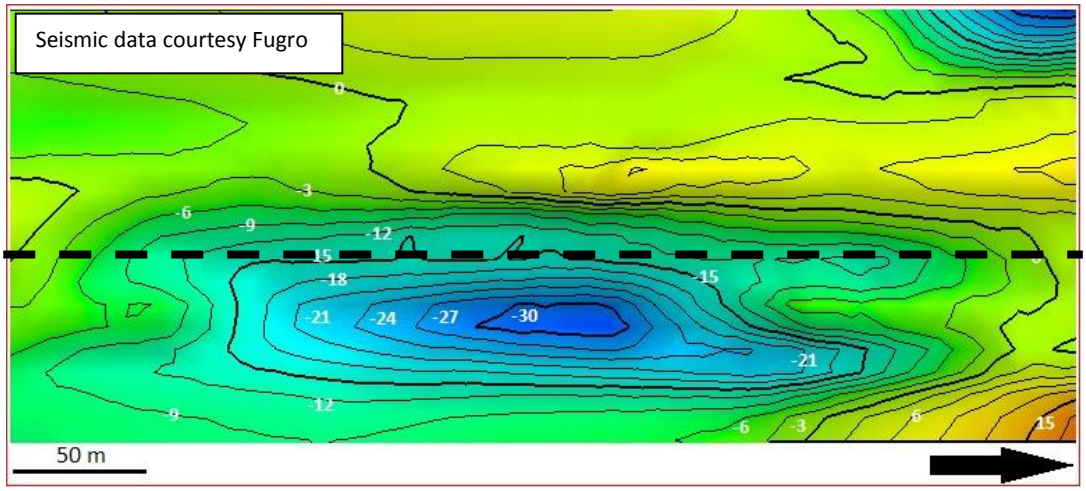

Figure 3.8: A near-angle stack horizon subtracted from the corresponding far-angle stack horizon. The derived differences in TWT (ms) may be a measure for the amount of velocity pull-down. The bright positive reflector, marked by the red arrow in figures 3.5 and 3.7, has been used. Negative values indicate relatively slow propagating near-angle traces. Colors specify depth in TWT (ms) where blue and red represent respectively negative and positive depths. The black dashed line represents the location of the seismic sections shown in figure 3.5.

3.3.2 Angle-stack data as input for the intercept-gradient method

If pre-stack gathers are not available, angle-stack data may also be used to get as many offset information as possible. In general, partial (angle) stacks contain strong seismic responses with the noise greatly reduced from the pre-stack gather and the data require less disk space than the gathers. However, since the data is partially stacked, offset information can be lost. As in this work pre-stack seismic data is available, this type of dataset is used to study the amplitude variation with offset. Nevertheless, the following section describes the use of angle-stack data as an input for the intercept-gradient method with respect to lead F04-P1 (anomaly 1, figure 1.1).

Table 3.2 shows the average amplitudes obtained from the near-mid-far stacks for a crossline (XL) range of 6958-6962 on the seismic section of lead F04-P1 shown in appendix A. The top-reservoir reflector, marked by the white dashed line in appendix A, has been used. The seismic data is converted to the US polarity convention. As the angle-stacks are used for the intercept-gradient method, only angles of incidence up to 35° are used (due to the Shuey approximation, section 2.4.2).

Table 3.2: Amplitudes for the near-mid-far stacks for a small area in the top-reservoir reflector of anomaly 1: lead F04-P1.

Type of stack	Average amplitude magnitude
Near (0-13°)	-17292
Mid (13-24°)	-16205
Far (24-34°)	-13406

It is assumed that the average amplitude magnitude values in table 3.2 correspond to the average angle of incidence per stack. Thus the magnitude of -17292 corresponds to an incidence angle of 6°. Figure 3.9 presents the average amplitudes plotted against the sine squared of the angle of incidence. A linear regression is applied and this results in both the intercept and gradient value of respectively -17663 and 18214. The maximum change in amplitude, between the near- and far-angle stacks, equals (-17292+13406) -3886 and is equivalent to a change of 22.5% with respect to the average amplitude magnitude observed on near-stack seismic data.

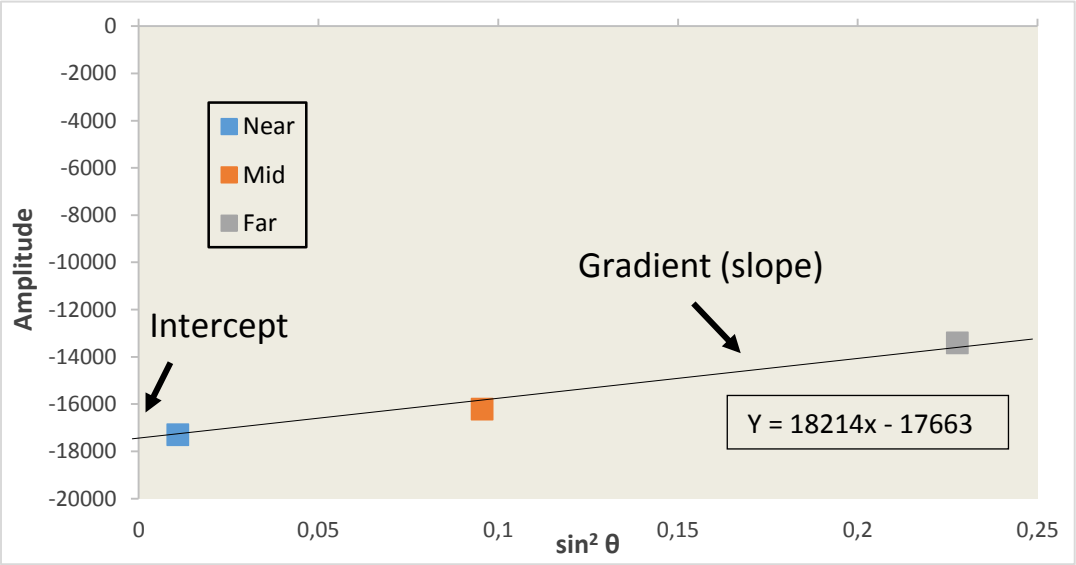

Figure 3.9: Intercept and gradient calculation from a linear regression of the amplitudes across near-mid-far stacks.

The use of near-mid-far stacks as an input for the intercept-gradient method yields a class 4 AVO anomaly corresponding to a small area in the top-reservoir reflector of lead F04-P1 (table 2.1 and figure 3.9).

4. Petrophysical analysis

As mentioned in figure 1.2, the first step in order to model the seismic response of shallow gas in the pre-stack domain is to identify a representative reservoir-seal combination that can be used as a base-case model; corresponding to water-bearing conditions. This chapter describes the performed petrophysical analysis in order to find appropriate values for the elastic properties (V_p, V_s and ρ) for both reservoir and seal in water-bearing conditions by constructing a mineral model. Representative reservoir-seal properties are required when performing fluid substitution (Chapter 5).

In this chapter the term *measured depth* is used. Appendix B presents a schematic section of well F04-01 (figure 1.1) that stresses the difference between various depth measures (e.g. *measured depth (MD)* and *true vertical depth subsea (TVD_{ss})*).

4.1 Logging tools

A petrophysical analysis is often performed using log data such as the gamma ray (GR) log, the density (RHOB) log, the neutron porosity (NPHI) log and the sonic (DT) log. Gamma ray logging is a method of measuring naturally occurring gamma radiation to characterize the rock or sediment in a borehole or drill hole. Shale usually emit more gamma radiation than other sedimentary rocks such as sandstones and limestones. The reason for this is that radioactive potassium is a common component in the clay content. Additional important components are uranium and thorium. These radioactive particles can be absorbed onto clay minerals because of the cation exchange capacity of clay and the organic matter content. The measured difference in radioactivity between shale and other sedimentary rocks allows this tool to distinguish between shale and non-shale (Wahl, 1983). The density logging tool emits gamma rays into a formation from a radioactive Cesium source at the bottom of the tool. Some gamma rays are absorbed by the surrounding formation, and some rays are scattered back and detected by the receiver above the source. The amount of rays arriving at the far receiver is inversely proportional to the electron density of the rock, which correlates strongly with the bulk density (Tittman and Wahl, 1965). The neutron logging tool releases fast neutrons from a chemical Americium/Beryllium source, which may collide with the nuclei of other atoms (especially hydrogen). The detector counts the neutrons which were slowed down due to the collision and were bounced back to the logging tool. This tool gives information about the hydrogen content in the formation. Sonic logs, or slowness logs, measure the travel time of sound through the surrounding rock in microseconds per unit distance. A transmitter emits a sound pulse which is received by two receivers. The travel time within the formation is equal to the difference in travel times corresponding to the far and near receiver. In this way the travel time within the drilling mud is disregarded. Since the distance between the near and far receiver is known, the compressional wave velocity of the formation can be derived.

The first step of the petrophysical analysis is to decide which well data to use. An inventory of the data availability per well in the study area (figure 1.1) is presented in appendix C. Since well F05-04 has by far the best data availability (e.g. density and velocity data) of the shallow subsurface, this well is initially used in the petrophysical analysis. The analysis consists of constructing a mineral model, and subsequently identifying a water-bearing reservoir-seal combination of which the elastic properties can be used as a base-case model.

4.2 Mineral model well F05-04

To identify a water-bearing reservoir, a mineral model is constructed using the GR log, the RHOB log, the NPHI log and the DT log corresponding to well F05-04 (figures 1.1 and 4.1). Although well F05-04 contains more data (e.g. spontaneous potential (SP) and resistivity data), only the four mentioned types of data are used as it is relatively easy to find corresponding mineral parameters for these types of data (section 4.2.1).

The GR response of pure quartz should be equal to zero, since no radioactive minerals are present within pure quartz. However, the GR response of the purest quartz in nature should be between 15 and 25 API as 100% pure quartz does not occur in nature (Crain, 2000). The GR log presented in figure 4.1, which shows a lowest value of 51 API in the interval analyzed, suggest that there are no clean sands within the interval. The depositional setting of this area, see section 1.1, may contradict this as it seems plausible to assume that sand bodies are present in a thick delta system with progradational and retrogradational trends. From the three producing fields (figure 1.3) it is known that its producing reservoirs consist of sand-shale mixtures. Instead of *shaley sands* there are also other explanations possible for the relatively high GR value corresponding to the cleanest sands in this interval: potassium feldspar, glauconite, heavy minerals, the use of potassium chloride (KCL) drilling mud and the deposition of so-called uranium salts in faults nearby. The presence of (radioactive) potassium feldspars in sands results in an increasing value of the GR response, this holds also for the presence of heavy minerals and glauconite in sands. The usage of KCL mud during drilling will also lead to an increasing GR response due to the radioactive potassium minerals. Since uranium is a radioactive mineral too, deposition of uranium salts in a fault nearby might increase the GR response as well. The above means that a spike in the GR data in figure 4.1, for example at a *measured depth* (MD) of ~740 m, does not necessarily correspond to the presence of shale and the lowest GR response measured (of 51 API) may still be a reaction to 'clean' sands although a higher GR value has been measured.

In order to obtain a proper mineral model, the first step is to know the composition of the deposits in the area studied. Most of the shallow gas leads, and all the producing shallow fields, lie in *the Upper North Sea Group* (NU). The group is present over almost the entire Netherlands but it may be absent as a result of local erosion or non-deposition (Boogaert and Kouwe, 1997). It contains sequences of clays, fine-grained to coarse sands and locally gravel. In this work, a mineral model of three components is assumed: sand (quartz), shale (which represents the fraction clay, silt and clay bounded water) and brine. Volume fractions of these three components, the mineral model, are derived from the log evaluation using the following logs: GR, DT, RHOB and NPHI. For an appropriate definition of the petrophysical mineral model the algorithm (section 4.2.2) requires the following input parameters: GR, DT, RHOB and NPHI values corresponding to pure quartz, shale and brine (considering brine as the only pore filling fluid).

4.2.1 Derivation of input parameters

This section describes the derivation of the required input parameters for the petrophysical analysis of well F05-04. It comprises parameters corresponding to quartz, shale and brine.

4.2.1.1 Quartz

The density of pure (clean) quartz is known from literature and is equal to 2.65 g/cm^3. However, most of the quartz particles in nature contain various heavy minerals (Crain, 2000). For this reason a density of 2.67 g/cm^3 corresponding to quartz is chosen. The NPHI log, the neutron response, measures the

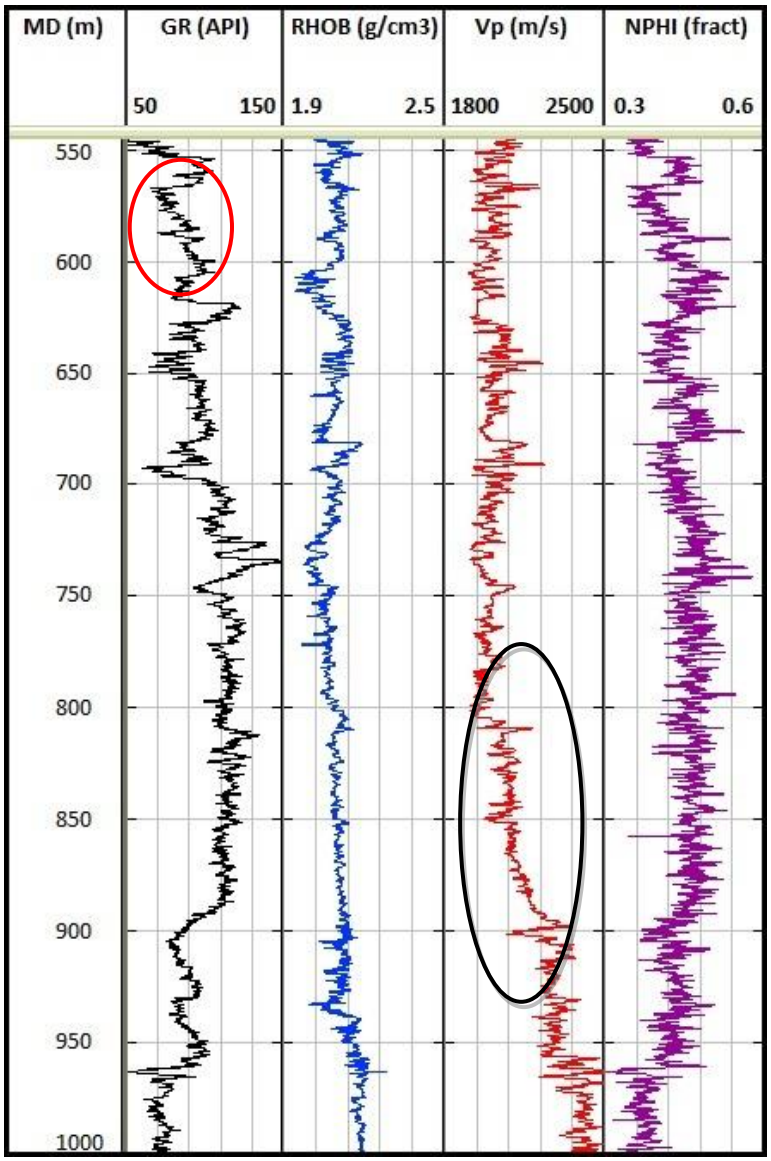

Figure 4.1: Well logs used in the petrophysical analysis of well F05-04. From left to right: gamma ray, density, compressional wave velocity and neutron porosity data. Note both the progradational and compaction trend highlighted by respectively the red circle on GR data and the black circle on V_p data.

hydrogen particles in the formation and presents the results in units of porosity (volume/volume). Since most of the hydrogen particles are present in water, a NPHI value of 0 is taken for the quartz mineral; quartz minerals do not bind any water. The DT value belonging to quartz is taken from literature and is equal to 55.5 µs/ft (Crain, 2000). The log evaluation is performed over a depth range of 550-1000 m (MD) since within this range all the data sources are available (figure 4.1). However, GR data is already available from 100 m depth (appendix D). The final geological evaluation report of well F05-04 shows clean sand intervals within a depth range of 100-200 m (MD). Using this information, a GR response of 20 API has been assumed for quartz.

4.2.1.2 Shale

In order to find appropriate GR, RHOB, DT and NPHI values for shale, log data is interpreted. According to Crain (2000) and because of the expected relatively high content bounded water in the moderately compacted shale of the Dutch North Sea Group mentioned by Boogaert and Kouwe (1997), a typical shale related NPHI value in this interval is assumed to be 0.5 (which is one of the highest values measured). Therefore the rest of the data is filtered on a NPHI value of 0.5, and cross plots are made with respectively DT, RHOB and GR data (for results see appendix E). The obtained relationships are used to derive DT, RHOB and GR values belonging to the neutron value which corresponds to the presence of shale (NPHI=0.5). The sonic slowness of shale depends on compaction, which expels available fluids in the formation. The effects of compaction in shale intervals is observed as a steady decrease in the compressional slowness, thus an increase in the compressional velocity (figure 4.1). On the contrary, when fluids cannot escape, the formation becomes overpressured which results in higher compressional slowness values. Based on the derived relationship a slowness value of 150 µs/ft has been assumed for shale in the analyzed interval. The corresponding RHOB and GR values are respectively 2.06 g/cm^3 and 115 API. For the cross plots, and corresponding relationships, see appendix E.

4.2.1.3 Brine

The last four input parameters needed correspond to the porosity. Here only brine is considered as a pore filling material. The density of brine has been calculated using the Batzle and Wang (1992) equations (section 5.1.3) and is equal to 1.05 g/cm^3. A value of 0.96 is chosen for the NPHI since besides water, salt is also a constituent of brine. Brine has no gamma ray response and a DT value of 195 µs/ft has been obtained from Batzle and Wang's method.

The following table gives an overview of the input parameters used for the petrophysical analysis of well F05-04:

Table 4.1: The input parameters for the petrophysical analysis of well F05-04 resulting from literature and log analysis.

	Φ (=brine)	Quartz	Shale
RHOB (g/cm^3)	1.05	2.67	2.06
NPHI (v./v.)	0.96	0.00	0.50
DT (µs/ft)	195.00	55.50	150.00
GR (API)	0.00	20.00	115.00

4.2.2 Algorithm

When the input parameters, for quartz, shale and brine, are obtained, the system of log response equations shown below is solved for calculating the mineral volume fractions and the effective porosity:

$$GR = \Phi_{effective} * GR_{fluid} + V_{quartz} * GR_{quartz} + V_{shale} * GR_{shale} \quad (36)$$

$$\rho_B = \Phi_{effective} * \rho_{fluid} + V_{quartz} * \rho_{quartz} + V_{shale} * \rho_{shale} \quad (37)$$

$$\Phi_{neutron} = \Phi_{effective} * \Phi_{neutron,fluid} + V_{quartz} * \Phi_{neutron,quartz} + V_{shale} * \Phi_{neutron,shale} \quad (38)$$

$$DT = \Phi_{effective} * DT_{fluid} + V_{quartz} * DT_{quartz} + V_{shale} * DT_{shale} \quad (39)$$

$$1 = \Phi_{effective} + V_{quartz} + V_{shale} \quad (40)$$

where GR_{fluid}, GR_{quartz} and GR_{shale} are respectively the gamma ray responses of the pore fluid (brine), quartz and shale in API and ρ_{fluid}, ρ_{quartz} and ρ_{shale} the densities of the fluid, quartz and shale. The same holds for the neutron porosity ($\phi_{neutron}$) and for the compressional slowness (DT in μs/ft). The parameters on the left hand side of equations 36, 37, 38 and 39 (GR, ρ_B, $\phi_{neutron}$ and DT) are the values obtained by the logging tools. These values consist of parts corresponding to the effective porosity (brine), quartz and shale. Equation 40, also known as '*the unit constraint*', shows that the volume fractions of shale and quartz together with the effective porosity should add up to one. Even though shale is seen as a mineral here, in fact it is a clastic, sedimentary rock composed of mud. However, with the appropriate input parameters, shale can be used as a mineral for this purpose. Since clay bounded water is included in the properties belonging to shale, the derived porosity will be the effective porosity instead of the total porosity (appendix L). There are only three unknowns: the effective porosity ($\phi_{effective}$), the volume fraction quartz (V_{quartz}) and the volume fraction shale (V_{shale}). The method performs constrained optimization in order to derive the three unknowns per log measurement (per 10 cm) in an interval from 550 m to 1000 m. The derived volume fraction set and the obtained effective porosity are shown in figure 4.2.

The results of the petrophysical analysis in well F05-04 show a relatively small fraction sand in the analyzed interval, suggesting that this interval does not contain the best reservoir facies to perform fluid substitution in; results show no representative reservoir-seal combinations. Due to the excellent data availability of well F05-04, initially this well was chosen to perform a petrophysical analysis on. The next step is to repeat the procedure for other wells in the study area in order to find a representative water-bearing reservoir-seal combination.

Final geological evaluation reports suggest that both well F05-01 and well F04-01 (figure 1.1) were drilled through water-bearing sand intervals at shallow depths, and thus may be used to identify a representative reservoir-seal combination for the base-case scenario.

4.3 Mineral models wells F05-01 and F04-01

As seen in appendix C, these two wells only contain useful gamma ray and compressional slowness data at the depth interval of interest (0-1000 m). Although the petrophysical analysis can be performed with only these two data sources, an alternative approach has been chosen. In this alternative approach density values are predicted using a V_p-ρ relationship which is derived from well F05-04, since eventually density data is required in Gassmann's algorithm. The whole depth interval of 550-1000 m in well F05-04 is used in order to establish this relationship. It may be more accurate to derive a V_p-ρ relation for quartz and shale separately, yet with the obtained volume fraction set of F05-04 this is practically not feasible. The derived V_p-ρ relationship is presented in appendix F.

The petrophysical analysis is repeated using equations 36, 37, 39 and 40 with the input parameters shown in tables 4.2 and 4.3 for respectively well F05-01 and well F04-01. The required parameters for brine are exactly the same as in the previous analysis, assuming that the composition of brine remains similar in the study area. The density and compressional slowness values for quartz are again acquired from literature and a gamma ray response of 20 API corresponds to the identified sand intervals, using final geological evaluation reports, in both well F05-01 and well F04-01. Appendix G and appendix H present the well data used for the petrophysical analysis of respectively well F04-01 and well F05-01. As

can be seen in appendix G, well data of F04-01 show relatively low gamma ray responses which may be caused by the presence of kaolinite minerals in clay particles (Crain, 2000).

Table 4.2: The input parameters for the petrophysical analysis of well F05-01 resulting from literature and log analysis.

	Φ (=brine)	Quartz	Shale
RHOB (g/cm^3)	1.05	2.67	2.02
DT (µs/ft)	195.00	55.50	150.00
GR (API)	0.00	20.00	95.00

Table 4.3: The input parameters for the petrophysical analysis of well F04-01 resulting from literature and log analysis.

	Φ (=brine)	Quartz	Shale
RHOB (g/cm^3)	1.05	2.67	2.12
DT (µs/ft)	195.00	55.50	139.00
GR (API)	0.00	20.00	85.00

The shale parameters are again based on the interpretation of log data. Appendix J and appendix I show the derivation of the parameters corresponding to shale for respectively well F05-01 and well F04-01. The volume fraction sets and effective porosities are, together with the results of the petrophysical analysis of well F05-04, presented in figure 4.2.

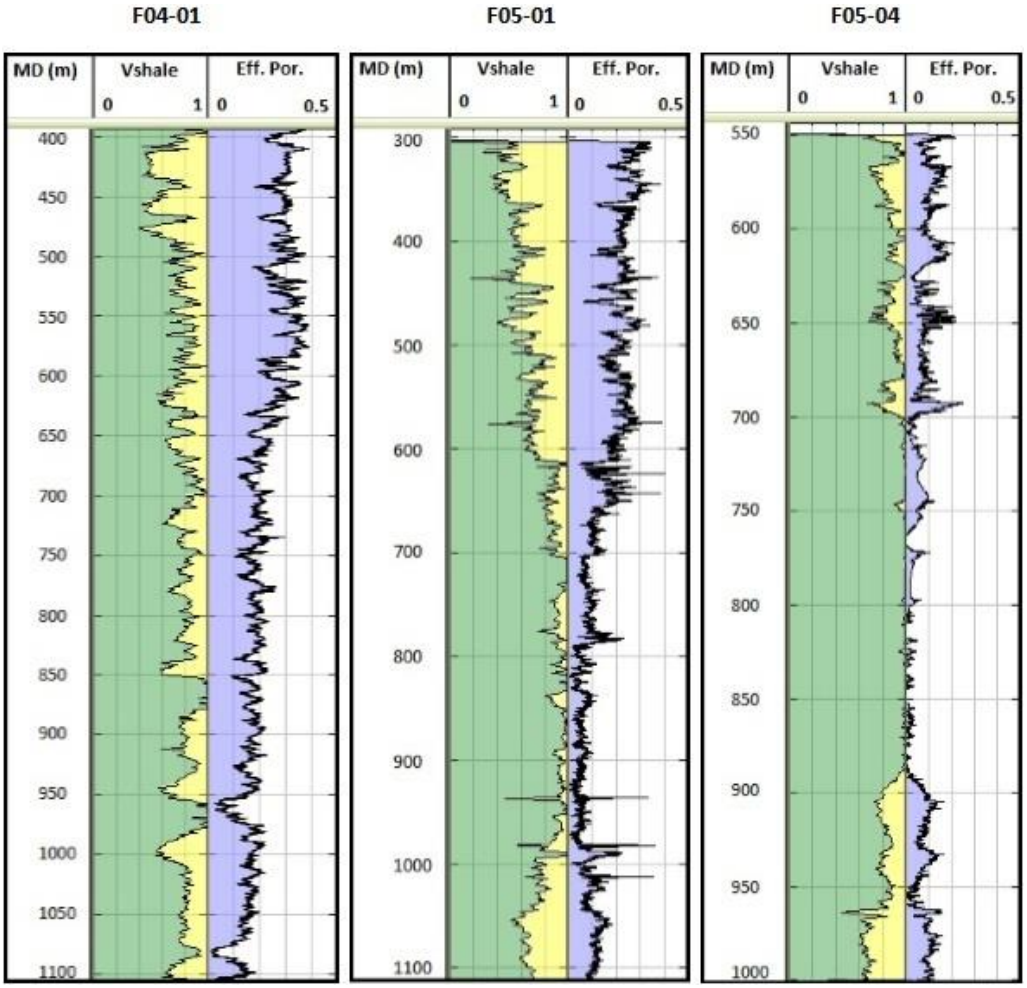

Figure 4.2: The results of the petrophysical analysis: the volume fraction sets and the effective porosities. From left to right: results for wells F04-01, F05-01 and F05-04. The volume fractions shale and quartz are shown in green and yellow respectively. Depth is expressed in measured depth (MD) in m.

4.4 Identification of a representative reservoir-seal combination

Since the volume fractions quartz and shale are known for the three wells studied, a water-bearing reservoir can be identified, which will be used as a base-case model. From figure 4.2 it is concluded that wells F04-01 and F05-01 show the finest data which indicate the best reservoirs. Since the results for well F04-01 show a better alternation between seals and reservoirs, this well is used in order to identify a target in: a water-bearing reservoir with corresponding overlying seal. Figure 4.3 presents the water-bearing reservoir with corresponding seal that is used as a base-case model in this study.

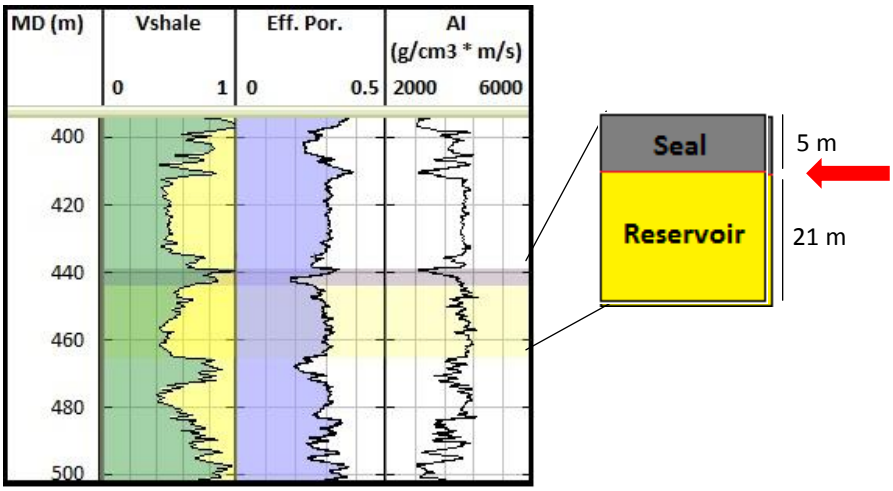

*Figure 4.3: The identified target in well F04-01. The reservoir and seal are marked in yellow and grey respectively. The top-reservoir reflector is the reflector of interest, highlighted by the red arrow in the right figure. From left to right: volume fraction shale in green, effective porosity (fraction) and the acoustic impedance (g/cm^3*m/s). Density data has been estimated using the empirical relationship from well F05-04.*

Because of the derived net-to-gross ratios of ~50% and ~20% for the reservoir and seal respectively, this reservoir-seal combination is chosen. Note that the shale layer is relatively thin (~5 m thick), but as stated by Verweij et al. (2014), thin sealing layers may have sufficient sealing capacity. Studying additional drilling information (e.g. the final geological evaluation report corresponding to well F04-01) confirms that the reservoir consists of a mixture of water-bearing shale and sand of Tertiary age (1971, report on www.nlog.nl). In this work, the reflectivity corresponding to the top-reservoir reflector will be modelled for varying angles of incidence, for different gas saturations in the reservoir, using Zoeppritz equations in a simple 2D model. For this purpose, the elastic parameters of both the identified seal and reservoir will be used. Fluid substitution, in order to find the elastic properties corresponding to different gas saturations, will be applied to the reservoir only.

Since performing fluid substitution and Zoeppritz modelling requires various input parameters, the next step is to find appropriate values for these parameters.

5. Rock physics

In chapter 4, a representative reservoir-seal combination has been identified from which the elastic properties (V_p, V_s and ρ) will be used to model the reflective interface between the seal and the reservoir (figure 4.3). In order to perform fluid substitution in the reservoir and to model reflectivities as a function of the angle of incidence, complete sets of elastic parameters, for the two layers, are required. As complete sets of elastic parameters are often unavailable, rock physics methods can be used to derive predictions for any missing data. In this work, various methods have been used to estimate appropriate density and shear wave velocity values, for the identified reservoir-seal combination, as initially only compressional velocities are available (section 4.3 and appendix C). The derivation of density and shear wave velocity values, the evaluation of mineral and fluid properties, a comparison between the use of theoretical models and the use of well data for deriving elastic parameters and the results of Gassmann's fluid substitution are described in this chapter.

5.1 Estimated input parameters

A common problem in modelling seismic responses corresponding to shallow gas using well data is the scarce data availability of the shallow subsurface. This holds also for this study, as most wells in the study area were drilled aiming for deeper targets (>1000 m depth). Mineral and fluid properties and a complete initial V_p-V_s-ρ set have to be known in order to perform Zoeppritz modelling in combination with fluid substitution (section 2.3). Since information about these parameters is not always available, several methods are used in order to derive appropriate values for these properties. These methods, along with other required input parameters, are described here.

5.1.1 Density

For the base-case model a water-bearing reservoir, and its overlying shale layer, have been identified in well F04-01 using the petrophysical analysis (section 4.4). For this analysis, density data was predicted using an empirical V_p-ρ relationship which was derived from well data of well F05-04. The derivation of this relationship is shown in appendix F.

5.1.2 Shear wave velocity

Information about the shear wave slowness is not available at all in the study area (appendix C). A reason for this may be the fact that the majority of the wells are relatively old, suggesting the usage of traditional logging tools which contain monopole sources. Monopole sources produce spherical outgoing compressional waves, which in turn stimulate compressional and shear waves in the formation (Crain, 2000). The produced shear headwave in the formation travels upward and is only measurable in fast formations. In formations which are slower, the shear component may be 'buried' in the tail of the compressional wave and can therefore not be measured (Schmitt, 1988).

As the shear wave velocity is one of the three elastic properties (V_p, V_s and ρ) with major importance, alternative approaches were studied to obtain shear wave velocity data: using empirical relationships of Han (1986) and Blangy (1992), using an established V_p-V_s relationship based on well data outside the study area and using Xu-White's (1995) clay-sand mixture model.

5.1.2.1 Empirical V_p-V_s relationships from literature

The empirical relationship of Han (1986), presented by equation 41, is one of the few relationships available:

$$V_s = 0.7936 * V_p - 786.8 \qquad (R^2 = 0.94) \tag{41}$$

where V_p and V_s are respectively the compressional and the shear wave velocity in m/s. Han (1986) used an extensive sandstone dataset with large ranges in porosity and clay content. The measurements were conducted on consolidated wet rock. Since the sediments in this work are poorly consolidated, this relationship might be a poor approximation for these conditions.

Blangy (1992) measurements were performed on wet, poorly consolidated sandstones and are given by the following formula:

$$V_s = 0.61088 * V_p - 314.59 \qquad (R^2 = 0.90) \tag{42}$$

As this equation only accounts for pure, poorly consolidated sandstones, mixtures of sand and shale are not taken into account. Since the identified reservoir within the study area contains both sand en shale, equation 42 may not result in reliable values corresponding to the shear wave velocity.

5.1.2.2 Empirical V_p-V_s relationships from well A15-04

Instead of using an empirical relationship from literature to derive shear wave velocities, it may be more accurate to derive a V_p-V_s relationship using a nearby well which does contain shear wave velocity data. This has been done using well A15-04 (appendix K). First, a distinction between sand and shale is made based on a gamma ray cut-off. Using the gamma ray data and the geological evaluation report of well A15-04, the following cut-off has been derived:

- <110 API = sand (reservoir);
- >120 API = shale (seal).

The transition zone of 10 API makes sure that only the cleanest sands and shale are taking into account. All the data of well A15-04, between 500 m and 1000 m depth, is now divided into two groups. For each group, sand and shale, an empirical relationship has been established and this is applied to the data of the well of interest (F04-01). In order to apply these empirical relationships, the dataset of well F04-01 is divided into seals and reservoirs according to the following conditions:

- $V_{shale}/V_{quartz} < 1.0$ = reservoir;
- $V_{shale}/V_{quartz} > 10$ = seal.

The mentioned conditions make use of the results of the petrophysical analysis of well F04-01 (V_{shale} and V_{quartz}). The application of the derived empirical relationships to the dataset of well F04-01 has a significant uncertainty level due to lateral variations in lithology, temperature and pressure between the locations of wells A15-04 and F04-01 (see figure 15 in appendix K). The derivation of the empirical relationships, the application of it to the reservoirs in well F04-01 and the comparison with both Han's (1986) and Blangy's (1992) relationships are presented in appendix K.

5.1.2.3 Xu-White's clay-sand mixture model

Instead of using empirical relationships, Xu-White's (1995) clay-sand mixture model might be used to derive shear wave velocity values. This method uses the Kuster and Toksoz (1974) differential effective medium (DEM) equations to estimate the density and the P- and S-wave velocities. The DEM equations use a solid mineral matrix (with no porosity) of known elastic parameters as a starting point in the iterative process: the host material. Next, small porosity fractions are added and for each new situation the elastic parameters are recalculated. Final V_p, V_s and ρ values, associated with the porosity of interest, are produced after all porosity fractions are added.

A key feature in modelling the clay-sand mixture is that the shape of the porosity inclusions is specified through the use of a shape factor. In this way, the effect of changing the pore geometry on V_p, V_s and ρ can be investigated; thus the clay/shale fraction is taken into account. The clay-sand mixture is modelled with ellipsoidal inclusions of two different aspect ratios (Xu and White, 1995):

- Sand fraction: $\alpha \approx 0.1\text{-}0.15$;
- Clay fraction: $\alpha \approx 0.02\text{-}0.05$.

The α represents the long-axis to short-axis aspect ratio which needs to be assigned using this method. The quartz fraction has stiffer pores, and therefore a higher aspect ratio, whereas the clay-related pores are much flatter and softer. In this work aspect ratios of 0.03 and 0.12 have been used for respectively clay and sand minerals.

The method uses the following porosity-related equations:

$$\Phi_{tot} = \Phi_{sand} + \Phi_{\text{clay}} \tag{43}$$

$$\Phi_{\text{sand}} = V_{sand}\frac{\Phi_{tot}}{1-\Phi_{tot}} \tag{44}$$

$$\Phi_{\text{clay}} = V_{clay}\frac{\Phi_{tot}}{1-\Phi_{tot}} \tag{45}$$

where V_{sand} and V_{clay} represent the volume fractions sand and clay respectively. Note that in the above equations the total porosity is required. Mavko et al. (1998) state that although the shale volume, derived using log-based analyses, includes silts and thus overestimates the clay content, results obtained by Xu and White justify the usage of the log-derived shale volume in this matter. However, for completeness, in this study the volume fraction shale and corresponding effective porosity (figure 4.3) are converted to the volume fraction clay and the total porosity using equations described by Connolly and Kemper (2007) (appendix L). Since now V_{sand}, V_{clay} and the total porosity are known, equations 43, 44 and 45 can be used. Knowing the aspect ratios and porosities for both sand and clay, an appropriate shear wave velocity value can be predicted for the clay-sand mixture using Xu-White's method. The way in which the defined aspect ratios are incorporated in the porosities of both sand and clay is described in the work of Xu and White (1995). Note that the properties belonging to the sand fraction correspond to the properties of quartz.

As mentioned before, the elastic properties of the solid mineral mixture (the host material) has to be known in order to use the DEM equations. These properties are estimated by a Wyllie time average of the quartz and the clay mineral velocities (Wyllie *et al.,* 1956) and an arithmetic average of their densities using the following formulas:

$$\frac{1}{V_{Psm}} = \frac{V_{quartz}}{1-\Phi_{tot}}\frac{1}{V_{Pquartz}} + \frac{V_{clay}}{1-\Phi_{tot}}\frac{1}{V_{Pclay}} \tag{46}$$

$$\frac{1}{V_{Ssm}} = \frac{V_{quartz}}{1-\Phi_{tot}}\frac{1}{V_{Squartz}} + \frac{V_{clay}}{1-\Phi_{tot}}\frac{1}{V_{Sclay}} \tag{47}$$

$$\rho_{sm} = \frac{V_{quartz}}{1-\Phi_{tot}}\rho_{quartz} + \frac{V_{clay}}{1-\Phi_{tot}}\rho_{clay} \tag{48}$$

where V_{Psm}, V_{Ssm} and ρ_{sm} denotes respectively the compressional wave velocity, the shear wave velocity and the density corresponding to the solid mineral mixture. Note that the above equations require elastic parameters corresponding to quartz and clay; Xu-White's model should be used in a total porosity system with (dry) clay as a mineral. Tables 5.2 and 5.3 show the required mineral and fluid properties (sections 5.1.3 and 5.1.4). The effective porosity obtained from the petrophysical analysis is converted to total porosity values using the shale porosity, as described in appendix L.

Equations 46, 47 and 48 estimate the elastic parameters for the solid mineral. When the porosity is set to zero, the elastic parameters form the starting point in the Kuster-Toksoz (DEM) method. Next the pores, for both sand and clay, are added incrementally in small steps; the aspect ratios and porosities for both quartz and clay are incorporated in the total porosity. Saturated velocities are calculated by using fluid-filled ellipsoidal inclusions in the Kuster-Toksoz (DEM) method. In this way, this clay-sand mixture model can be used to predict saturated shear wave velocities (Xu and White, 1995).

Xu-White's method has been used in this work because of the fact that this method considers the clay/shale content within the reservoir studied. The formulas and a detailed explanation of the method is given by Keys and Xu (2002). Although this method produces compressional wave velocity, shear wave velocity and density data, only the predicted V_s data is used in this study. The results, and a comparison with the empirical V_p-V_s relationships from well A15-04, are shown in appendix K.

5.1.3 Fluid properties

The fluid substitution method used, Gassmann's (1951) equations (section 2.3.1), requires elastic parameters corresponding to the pore fluids. In order to predict values for these properties, Batzle and Wang's (1992) equations are used.

Properties of pore fluids vary with composition, pressure and temperature. Batzle and Wang (1992) described these variations for three primary types of reservoir fluids: hydrocarbon gases, oils and brines. In this study only the relations for brines and gases are considered.

5.1.3.1 Gas

Mixtures of natural gas are characterized by its specific gravity (G), which is the ratio of gas density to air density at a temperature of 15.6 °C and at atmospheric pressure. According to GasTerra (www.gasterra.nl), natural gas from the Groningen field consists of the following constituents:

- 82% Methane (G = 0.56);
- 15% Nitrogen (G = 0.97);
- 3% Ethane (G = 1.04).

Which yields a specific gas gravity of 0.63 for natural gas of the Groningen field. Since the exact composition of the shallow gas in the study area is unknown, the gas gravity corresponding to gas of the Groningen field is used in this study. With a rough estimate of the gas gravity, a reasonable prediction for both the bulk modulus and the density can be made at a specific pressure and temperature.

The first step is to calculate the absolute temperature T_a in Kelvin:

$$T_a = T + 273.15 \tag{49}$$

with T in °C.

Properties of mixtures can be made more systematic when the temperature and the pressure are normalized by the critical values, resulting in the pseudo temperature and pseudo pressure (Katz, 1959). When the properties of the gas and liquid phase have been merged, the critical temperature and pressure has been reached. Since Batzle and Wang's algorithm uses the pseudo pressure P_r and the pseudo temperature T_r, the next step is to calculate these parameters using equations obtained by Thomas et al. (1970):

$$P_r = \frac{P}{4.892 - 0.4048G} \tag{50}$$

$$T_r = \frac{T_a}{94.72 + 170.75G} \tag{51}$$

where P, T_a and G are the pressure (MPa), absolute temperature (K) and the gas gravity (G) respectively.

The gas density, ρ_G in g/cm^3, can be predicted as follows:

$$\rho_G \approx \frac{28.8GP}{ZRT_a} \tag{52}$$

where

$$Z = [0.03 + 0.00527(3.5 - T_r)^3]P_r + (0.642T_r - 0.007T_r^4 - 0.52) + E \tag{53}$$

and

$$E = 0.109(3.85 - T_r)^2 \exp\left\{-\left[0.45 + 8\left(0.56 - \frac{1}{T_r}\right)^2\right]\frac{{P_r}^{1.2}}{T_r}\right\} \tag{54}$$

and R is the gas constant (8.3144 J/K/mol).

The above approximation of the density is valid as long as P_r and T_r are not both within 0.1 of unity (Batzle and Wang, 1992). The same restriction holds for the estimation of the adiabatic bulk modulus, K_G, in GPa:

$$K_G \approx \left(\frac{P}{1 - \frac{P_r}{Z} f} y \right) 10^{-3} \tag{55}$$

where

$$y = 0.85 + \frac{5.6}{P_r + 2} + \frac{27.1}{(P_r + 3.5)^2} - 8.7 \exp[-0.65(P_r + 1)] \tag{56}$$

and

$$f = 0.109(3.85 - T_r)^2 \exp\left\{ -\left[0.45 + 8\left(0.56 - \frac{1}{T_r}\right)^2 \right] \frac{{P_r}^{1.2}}{T_r} \right\} 1.2 \left\{ -\left[0.45 + 8\left(0.56 - \frac{1}{T_r}\right)^2 \right] \frac{P_r^{0.2}}{T_r} \right\} + 0.03 + 0.00527(3.5 - T_r)^3 \tag{57}$$

thus

$$f = \frac{\partial Z}{\partial P_r} \tag{58}$$

Both the gas density (ρ_G) and bulk modulus (K_G) increase with pressure and decrease with temperature. Note that the derived values for ρ_G and K_G are equal to ρ_{hyc} and K_{hyc} in equations 33 and 34 (section 2.3.1).

As the pore filling material in this study only consists of brine, gas or a mixture of the two, the next step is to derive the elastic properties for brine.

5.1.3.2 Brine

The most common pore fluid is brine. Compositions can range from almost pure water to saturated saline solutions. Using simple relations between the water resistivity and the formation pressure, the salinity of brine can be determined (Crain, 2000). However, local salinity may be perturbed by ground water flow or shale dewatering (Batzle and Wang, 1992).

Since the wells in the study area were all drilled aiming at relatively deep targets (>1000m depth), no water analysis was performed in the shallow subsurface. For this work a salinity of 0.076 (fraction NaCl), which was measured at a depth of ~775 m (TVD_{ss}) in well MKP-14, has been used. It is assumed that this salinity is also valid for the water-bearing reservoir of interest in well F04-01. Appendix M shows additional information about the salinity measurement in well MKP-14.

The density of brine increases with salinity. Batzle and Wang derived a polynomial in temperature, pressure and salinity, using data provided by Zarembo and Fedorov (1975) and Potter and Brown (1977), in order to calculate the density of brine with salinity S:

$$\rho_B = \rho_W + S\{0.668 + 0.44S + 10^{-6}[300P - 2400PS + T(80 + 3T - 3300S - 13P + 47PS)]\} \tag{59}$$

where ρ_W is the density of pure water, and is given by:

$$\rho_W = 1 + 10^{-6}(-80T - 3.3T^2 + 0.00175T^3 + 489P - 2TP + 0.016T^2P - 1.3 * 10^{-5}T^3P - 0.333P^2 - 0.002TP^2) \quad (60)$$

where S is the salinity of sodium chloride (NaCl) in fractions, P the pressure in MPa and T the temperature in °C. The densities, ρ_B and ρ_W, are given in g/cm^3.

The acoustic velocity in brine, V_B in m/s, can be obtained by:

$$V_B = V_W + S(1170 - 9.6T + 0.055T^2 - 8.5 * 10^{-5}T^3 + 2.6P - 0.0029TP - 0.0476P^2) + S^{1.5}(780 - 10P + 0.16P^2) - 1820S^2 \quad (61)$$

where the acoustic velocity in pure water, V_W in m/s, is given by:

$$V_W = \sum_{i=0}^{4}\sum_{j=0}^{3} \omega_{ij}\, T^i P^j \quad (62)$$

with again the pressure P in MPa and the temperature T in °C. The coefficients ω_{ij} are shown in appendix N.

Since the density and compressional wave velocity of brine, ρ_B (g/cm^3) and V_B (m/s), can be derived, the following formula is used to estimate the bulk modulus of brine (K_B) in GPa:

$$K_B = \left(\rho_B {V_B}^2\right)10^{-6} \quad (63)$$

Mavko et al. (1998) define the gas-water ratio, R_G, as the ratio of the volume of dissolved gas (at standard conditions of 15.6 °C and at atmospheric pressure) to the volume of brine. For temperatures below 250 °C, the maximum amount of methane that can go into solution in brine is:

$$\log_{10}(R_G) = \log_{10}(0.712P|T - 76.71|^{1.5} + 3676P^{0.64}) - 4 - 7.786S(T + 17.78)^{-0.306} \quad (64)$$

They also provide a relationship between the bulk modulus of gas-free brine, K_B, and the bulk modulus of brine that contains a gas-water ratio R_G (K_G):

$$\frac{K_B}{K_G} = 1 + 0.0494R_G \quad (65)$$

The above equation shows that K_G decreases linearly with increasing gas saturation. On the other hand, the density is almost independent of the amount of dissolved gas (Mavko *et al.,* 1998).

As earlier mentioned, the elastic properties of brine can range from nearly pure water to saline solutions of approximately 50 percent sodium chloride (Crain, 2000). Density and acoustic velocity values can be dramatically altered if a considerable amount of gas is absorbed.

Since in this work the focus is on the shallow subsurface (< 1000 m depth below mean sea level) and the provided algorithm (equations 64 and 65) only considers the maximum amount of methane that can go

into solution, no dissolved gas is assumed. This seems a valid assumption as the amount of dissolved gas is substantially higher in deeper brines than in shallower brines, as the solubility of gas in brine increases with pressure:

$$p = kC \tag{66}$$

where p is the pressure in atmosphere (atm), k a temperature dependent constant in L atm/mol and C the amount of dissolved gas in the liquid in mol/L. The above equation is also known as *Henry's law*.

Note that the derived density (ρ_B) and bulk modulus (K_B) for brine, by respectively equations 59 and 63, is equal to ρ_{brine} and K_{brine} in equations 33 and 34 (section 2.3.1).

5.1.3.3 Input parameters

Usage of Batzle and Wang's equations requires information on the gas gravity G, the salinity of brine, the temperature and the pressure. The derivation of the gas gravity and salinity has been discussed earlier and the temperature and pressure values are estimated using the following gradients:

- Temperature gradient: 25 °C/km. When a temperature of 5 °C is assumed at the sea floor, a temperature of 15.6 °C is obtained for a depth of 425 m below the sea floor (which corresponds with the location of the identified water-bearing reservoir (figure 4.3 and appendix B)).
- Hydrostatic pressure gradient: 1.02 bar/10 m. This gradient differs from the gradient for pure water because of its salinity. By using the hydrostatic gradient, all pores are assumed to be connected. This seems a valid assumption since in this work the focus is on the shallow subsurface; unconsolidated sediments. Including a water depth of 48 m, a depth of 452 m (TVD_{ss}) is used (figure 4.3 and appendix B), resulting in a formation pressure of 46.1 bar, thus 4.6 MPa.

The following table gives an overview of the required input parameters for Batzle and Wang's method when applying it to the reservoir of interest in well F04-01:

Table 5.1: The input parameters used in Batzle and Wang's method.

Temperature (°C)	Pressure (MPa)	Gas gravity	Salinity NaCl (fraction)
15.6	4.6	0.63	0.076

The calculated fluid properties, for both brine and gas, are shown in table 5.2. Compressional velocities can be derived using equation 1 where μ equals zero.

Table 5.2: The calculated fluid properties using Batzle and Wang's (1992) method.

Fluid Type	K_{fluid} (GPa)	μ (GPa)	ρ (g/cm^3)	V_p (m/s)	V_s (m/s)
Brine	2.57	0.00	1.05	1558.70	0.00
Gas	0.01	0.00	0.04	407.27	0.00

5.1.4 Mineral properties

Except fluid properties, mineral properties are also required for performing fluid substitution in combination with Zoeppritz modelling (section 2.3.1). The petrophysical analysis is performed in the effective porosity system whilst the total porosity system has to be used for predicting shear wave velocities and might be used for performing fluid substitution. Elastic properties for quartz, shale and dry clay are essential for converting between the total and effective porosity system (appendix L). For both quartz and shale assumptions of their properties have been made during the petrophysical analysis of well F04-01 (section 4.3 and table 4.3).

5.1.4.1 Quartz

Values for the density, compressional and shear wave velocities corresponding to quartz were taken from the work of Crain (2000).

5.1.4.2 Shale

As mentioned earlier, the properties belonging to shale are based on interpretation of log data (section 4.3). Corresponding shear wave velocity has been obtained by plotting the derived V_s data (with Xu-White's method) as a function of the volume fraction shale, which has been obtained during the petrophysical analysis (figure 5.1).

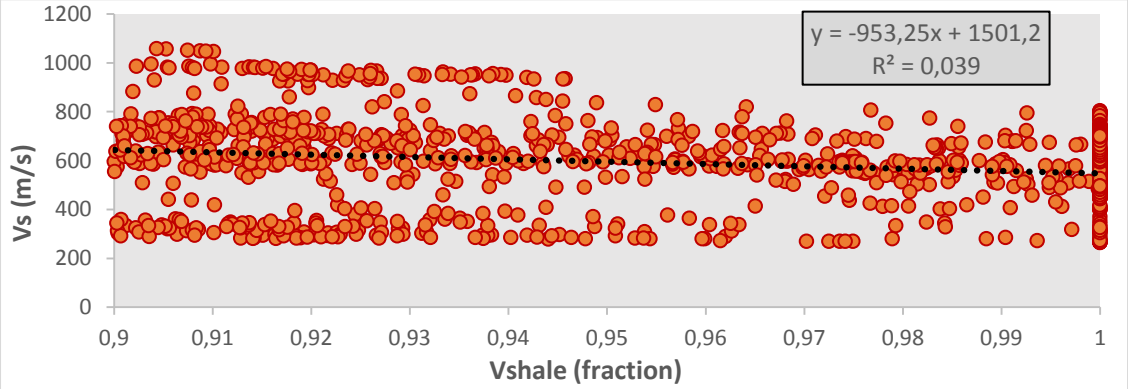

Figure 5.1: The relationship between V_s and the volume fraction shale in well F04-01. Note that, for well F04-01, the whole depth interval of 400-1100 m (MD) has been used here.

Based on figure 5.1, a shear wave velocity of 548 m/s has been used for the shale fraction.

5.1.4.3 Dry clay

The elastic properties of dry clay are highly variable (Wang *et al.,* 2001). The values used in this work are average values based on the work of Wang et al. (2001) and the work of Castagna et al. (1993).

The mineral properties are presented in table 5.3. Conversion between bulk and shear moduli and seismic velocities is done by using equations 1 and 2.

Table 5.3: The mineral properties for quartz, shale and dry clay.

Mineral Type	$K_{mineral}$ (GPa)	μ (GPa)	ρ (g/cm^3)	V_p (m/s)	V_s (m/s)
Quartz	38.59	31.46	2.67	5491.96	3432.47
Shale	9.35	0.64	2.12	2192.83	548.00
Dry Clay	27.00	17.00	2.68	4304.92	2518.59

Figure 5.2 presents an overall scheme which emphasizes the contributions of the various rock physics methods.

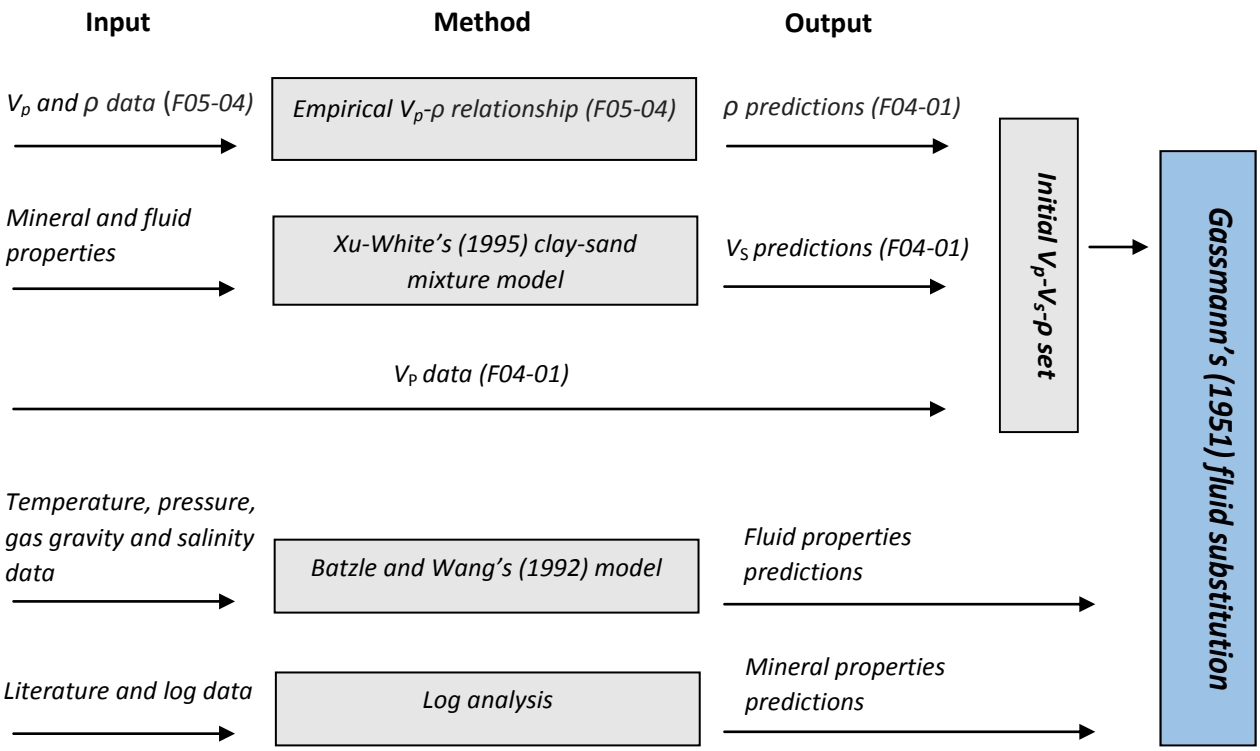

Figure 5.2: The overall rock physics methods scheme that is used in this study. Note that Xu-White's (1995) clay-sand mixture model requires the output of both Batzle and Wang's (1992) method and the log analysis (e.g. fluid and mineral properties). When the initial V_p-V_s-ρ set and the fluid and mineral properties are known, Gassmann's equations can be used to derive estimations of elastic properties corresponding to different gas saturations.

As the fluid and mineral properties are known, and a complete set of elastic properties is available, fluid substitution can be applied to the water-bearing reservoir. But before Gassmann's equations are used, attention is paid to the use of theoretical models instead of well data in order to estimate the elastic parameters.

5.2 Theoretical model versus well data

In this study, well data (V_p) and predicted density and shear wave velocity are used to derive an initial V_p-V_s-ρ set for the seal and water-bearing reservoir (figure 4.3). Instead of using well data, one may also use theoretical models in order to estimate the elastic moduli (bulk modulus (K) and shear modulus (μ)) of the sediments of interest. This section describes the use of both the *Hashin-Shtrikman bounds* (Hashin and Shtrikman, 1963) and *Berryman's approach* (Berryman, 1995) in order to derive estimations for the elastic moduli.

5.2.1 The Hashin-Shtrikman bounds

Theoretical estimates of the effective bulk and shear modulus depend on:

1- the volume fractions of the components;
2- the elastic moduli of the individual constituents;
3- the geometric details of the shape distribution of the components.

When only the volume fractions and the constituent moduli are specified it is possible to predict the upper and lower bounds, which represent respectively cemented and unconsolidated rocks. The *Hashin-Shtrikman* (Hashin and Shtrikman, 1963) bounds is the most commonly used method in order to predict the effective elastic moduli of a mixture of two materials.

The Hashin-Shtrikman bounds "provide the narrowest possible range of elastic moduli without specifying geometries of constituents" (Mavko *et al.,* 1998, page 414). At any given volume fraction of constituents the effective modulus will fall between the two bounds, but its exact location depends on the geometric specifics. The bounds are given by (Mavko *et al.,* 1998):

$$K_{HS\pm} = K_1 + \frac{f_2}{(K_2 - K_1)^{-1} + f_1(K_1 + \frac{4}{3}\mu_1)^{-1}} \tag{67}$$

$$\mu_{HS\pm} = \mu_1 + \frac{f_2}{(\mu_2 - \mu_1)^{-1} + \frac{2f_1(K_1 + 2\mu_1)}{5\mu_1(K_1 + \frac{4}{3}\mu_1)}} \tag{68}$$

where

K_{HS} and μ_{HS} = bulk and shear moduli calculated using the Hashin-Shtrikman bounds;

K and μ = bulk and shear moduli of the individual constituents;

f = volume fraction of the individual phases.

The expressions above show that the Hashin-Shtrikman bounds consider a mixture of two materials, subscribed with either a 1 or a 2. If the stiffest material is subscribed with 1 and the softest material with 2, the formulas give the upper bound which is used for cemented rocks. On the other hand, the lower bound, used for unconsolidated rocks, is given by equations 67 and 68 if the stiffest material is termed 2 and the softest material 1. The bounds can be used to compute the upper and lower bounds for a mixture of mineral and pore fluid, thus predicting corresponding elastic moduli for the two extreme situations: unconsolidated or cemented conditions. The method assumes isotropic and elastic

constituents. Since in this study the focus is on unconsolidated sediments, only the lower bound is discussed further in this section.

5.2.1.1 Lower bound

The base-case model consists of three constituents: quartz, shale and brine (section 4.3). As shown by the equations for the Hashin-Shtrikman bounds, bulk and shear moduli are required for the soft (brine) and the stiff (quartz-shale mixture) materials. The properties corresponding to brine are obtained using Batzle and Wang's (1992) method, described in section 5.1.3.2, and shown in table 5.2. In order to estimate bulk and shear moduli values for the quartz-shale mixture, equation 32 from section 2.3.1 is used (the Voigt-Reuss-Hill average) for volume fractions of 0.45 and 0.55 for respectively shale and quartz (e.g. the average volume fractions in the reservoir; figure 4.3). The quartz and shale moduli (section 5.1.4) are shown in table 5.3. The density corresponding to the stiff material is estimated by:

$$\rho_{stiff} = V_{quartz}\rho_{quartz} + V_{shale}\rho_{shale} \tag{69}$$

Table 5.4 presents the required elastic parameters for both the soft and stiff material.

Table 5.4: Input parameters (K and μ) for the calculation of the Hashin-Shtrikman lower bound shown in figure 5.3. Volume fractions used are 0.45 and 0.55 for respectively shale and quartz. The corresponding densities, used to convert between elastic moduli and seismic velocities, are also shown.

	Soft material (brine)	Stiff material (shale – quartz mixture)
K (GPa)	2.57	12.75
μ (GPa)	0	9.16
ρ (g/cm^3)	1.05	2.42

The volume fraction brine is equal to the effective porosity which has been obtained during the petrophysical analysis, thus $1 - \phi_{effective}$ equals the volume fraction of the stiff material. The derived elastic moduli using the Hashin-Shtrikman lower bound is converted to compressional and shear wave velocities using equations 1 and 2 and an arithmetic average of both the brine and shale-quartz mixture densities:

$$\rho = \phi_{effective}\rho_{brine} + (1 - \phi_{effective})\rho_{stiff} \tag{70}$$

Note that the Hashin-Shtrikman lower bound in figure 5.3 is derived assuming the mentioned volume fractions for shale and quartz; reducing its validity to only this combination of volume fractions.

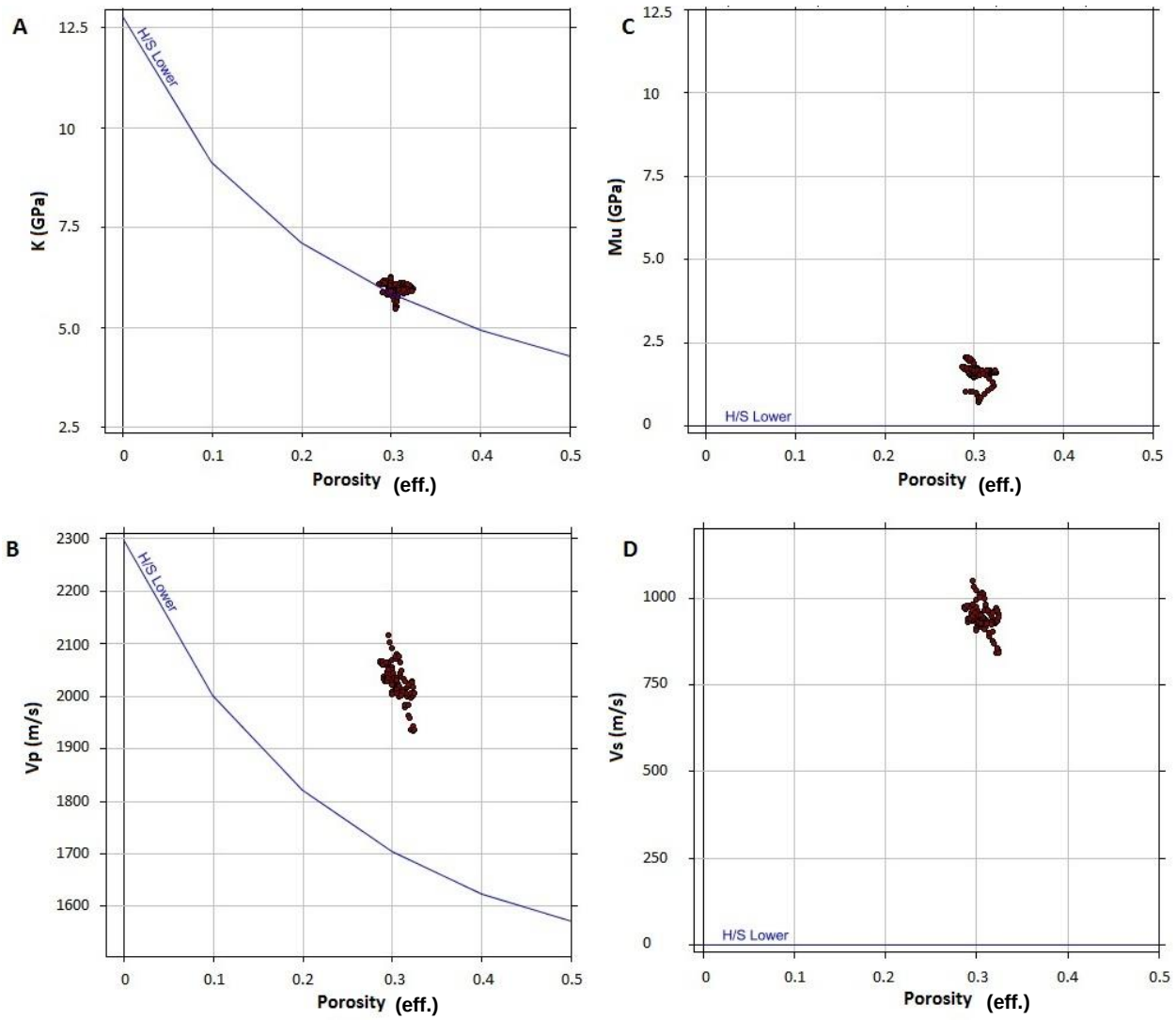

Figure 5.3: Comparison between (partly derived) well data of well F04-01 and the calculated Hashin-Shtrikman lower bound for a shale and quartz fraction of respectively 0.45 and 0.55: A) bulk modulus versus effective porosity, B) compressional wave velocity versus effective porosity, C) shear modulus versus effective porosity and D) shear wave velocity versus effective porosity. The data points shown in dark red belong to the area within the identified water-bearing reservoir (figure 4.3) where V_{shale} is within 0.4-0.5 range and V_{quartz} within 0.5 – 0.6 range (figure 5.6 in section 5.3). The derived lower bound is presented by the blue line.

The bulk moduli, based on the use of well data (V_p) and predicted density and shear wave velocity, match very well with the derived lower bound. Since the shear modulus for the soft material (brine) equals zero, the Hashin-Shtrikman lower bound describes the moduli of a suspension of grains in a pore fluid exactly, which results in the zero-trend for the shear wave velocity and shear modulus. As the shear modulus is underestimated, the lower bound underestimates the compressional wave velocity as well (figure 5.3).

Based on the above it is concluded that the Hashin-Shtrikman lower bound theory may be used to predict bulk moduli regarding the unconsolidated sediments studied in this thesis work, whilst it underestimates corresponding shear moduli.

5.2.2 Berryman's approach

Berryman (1995) derived a more general form for the bounds. An advantage of this approach is that it can be applied to more than two phases. These adapted bounds are given by Mavko et al. (1998) and corresponding formulas are presented in appendix O. The lower bound of Berryman's approach might be used to predict effective elastic moduli for unconsolidated sediments consisting of more than two components. This has been applied to the water-bearing reservoir in well F04-01 (figure 4.3) and the calculation, with corresponding results, are shown in appendix O.

For an effective porosity of 0.31, which equals the volume fraction soft material in the Hashin-Shtrikman expressions, Berryman's approach results in a bulk modulus of 6.11 GPa for the lower bound. When the traditional equations are used, which are valid for two components only, a bulk modulus of 5.72 GPa has been obtained (figure 5.3). Again, as the shear modulus of the softest material equals zero, the predicted shear modulus equals to zero as well.

The predicted bulk moduli, for both methods shown in this section, correspond very well with the bulk moduli based on well data (figure 5.3). However, using theoretical models in this case results in an underestimated shear modulus, thus an underestimated compressional wave velocity.

Instead of using theoretical models, well data (e.g. velocity data) is used in this study in order to determine the initial elastic moduli for the rock of interest. The initial elastic moduli are required input parameters for Gassmann's algorithm, which derives new values for the elastic moduli corresponding to various gas saturations in the reservoir. The next section describes the application of Gassmann's equations to the reservoir of interest.

5.3 Fluid substitution: dry rock modelling

The theory behind Gassmann fluid substitution is described in section 2.3. Here a description is given of the dry rock modelling process which is used. It involves the estimation of the dry rock bulk modulus from the initial bulk modulus, and the derivation of the final bulk modulus (corresponding to different gas saturations in the reservoir) from the dry rock bulk modulus. When using Gassmann fluid substitution, it is important to decide in advance which porosity system is being used and ensure that all input parameters are consistent with the selected porosity system. First, the differences between the total and effective porosity systems are discussed.

5.3.1 Effective versus total porosity approach

Two porosity systems can be distinguished: the effective and the total porosity systems (appendix L). The petrophysical analysis, discussed in Chapter 4, has been done using the effective porosity system with shale as a mineral whilst prediction of V_s with Xu-White's method (1995) assumes the total porosity system (section 5.1.2.3). This section discusses the differences between the two porosity systems.

When working in an effective porosity system, several assumptions are made:

- The effective porosity, which excludes the pore space containing clay bound water, is used.
- The 'mineral' shale is used in order to represent the clay rich fraction of the rock frame. The mineral properties should correspond to this fraction including the clay bounded water.
- The saturations of the mobile fluid component are used for both the initial and final fluids. Only the mobile fluids are mixed (equations 33 and 34 in section 2.3.1); the clay bound water is not included.

Using this approach in Gassmann's equations, the process of calculating the dry bulk modulus from the initial bulk modulus removes only the mobile fluids.

The total porosity refers to the total void space, including the fraction occupied by clay bounded water. When working in a total porosity system the following assumptions are made:

- The total porosity is used.
- The 'mineral' dry clay is used instead of the 'mineral' shale. The mineral properties should be those of the dry clay mineral, excluding the clay bounded water.
- The used saturations should correspond to the total saturations for both the initial and final fluids. The water saturation used includes the clay bounded water. In this case also the clay bounded water is mixed with any hydrocarbons.

In this approach the clay bound water is treated as being mobile and is removed during the calculation of the dry rock bulk modulus from the initial bulk modulus.

As will be mentioned later in this section, the total porosity approach is used in this study (figure 5.5).

5.3.2 From initial to dry bulk moduli

The first step using Gassmann's approach is to obtain the dry rock bulk modulus from the initial bulk modulus based on the log data used. Gassmann dry rock modelling requires V_p, V_s and density data of

the in-situ situation: the elastic moduli of the original situation. The logged V_p and the derived density and V_s data, by using respectively an empirical V_p-ρ relationship from well F05-04 and Xu-White's (1995) method, are used. For the initial situation, a water saturation (S_w) of 100% is used: all pores are filled with brine.

The initial mineral modulus is calculated using the Voigt-Reus-Hill average (equation 32 in section 2.3.1). Note that this equation can be used with shale or clay as an input parameter. The required volume fractions shale and quartz are derived during the petrophysical analysis and the elastic properties for shale and quartz are respectively obtained by log interpretation and literature study (section 5.1.4). Dry clay properties and volume fractions (required when using the total porosity approach) are acquired from literature study and the total-effective porosity system converter (appendix L) respectively. Equations 1 and 2, shown in section 2.1.1, are used to convert seismic velocities and densities to elastic bulk and shear moduli for shale, dry clay and quartz minerals. Properties of the initial and final fluids are determined using Batzle and Wang's method (1992) (section 5.1.3). Tables 5.2 and 5.3 give an overview of all the properties of both the minerals and the fluids.

Since at this stage the volume fractions and elastic moduli for quartz, dry clay and shale, the (initial and final) fluid properties and the effective and total porosity have been obtained, dry rock data can be derived from Gassmann inversion using the following steps:

1- Derive the initial bulk modulus and density of the mineral matrix, $K_{mineral}$ and $\rho_{mineral}$, by respectively using equation 32 and weighted averaging the densities of the individual minerals.
2- Estimate the initial bulk modulus and density of brine, K_{brine} and ρ_{brine}, from Batzle and Wang's (1992) method (section 5.1.3.2). Since in the initial situation only brine is considered, the parameters for brine equals the parameters for the initial fluid in the pore space ($K_{brine} = K_{fl}$).
3- Evaluate the initial saturated bulk and shear modulus, $K_{sat}^{initial}$ and $\mu_{sat}^{initial} = \mu_{sat}^{final}$, from equations 1 and 2. Logged V_p and estimations of ρ and V_s are used as input parameters here.
4- Estimate the dry rock bulk modulus, K_{dry}, from Gassmann's equation using the initial saturated bulk modulus derived in step 3 (equation 30).

Before performing fluid substitution with the dry rock data corresponding to the investigated sediments, attention is paid to dry rock data from laboratory measurements. Figure 5.4 shows a cross plot with dry rock data from the following laboratory studies: Blangy (1992), Strandenes (1991), Domenico (1977) and Han (1986) and derived dry rock data corresponding to the identified water-bearing reservoir in well F04-01 (total porosity approach used). In the plot, normalized bulk moduli (dry bulk modulus divided by the bulk modulus of the mineral matrix) is plotted against the total porosity. Also lines of constant normalized pore stiffness are shown. The dry pore space stiffness, K_ϕ, is defined as the ratio of the fractional change in pore volume to a growth of applied external hydrostatic stress (Mavko *et al.,* 1998). The lines of constant normalized pore stiffness in figure 5.4 are the Voight-Reuss-Hill bounds and represent different ways of mixing rock and fluid (Reuss, 1929). The softest possible mix is the Reuss bound (lower bound) and the stiffest is the Voigt bound (upper bound); at any given porosity, the normalized bulk modulus will fall between the bounds (Mavko *et al.,* 1998). It is expected that two sandstones with the same porosity, but different (normalized) pore stiffness, will show different sensitivity to the fluid substitution effect on their compressional wave velocity. Due to this difference in

the compressibility of the pores, the change in V_p in stiffer (e.g. better cemented) sand is expected to be far less than in the softer (e.g. unconsolidated) sand.

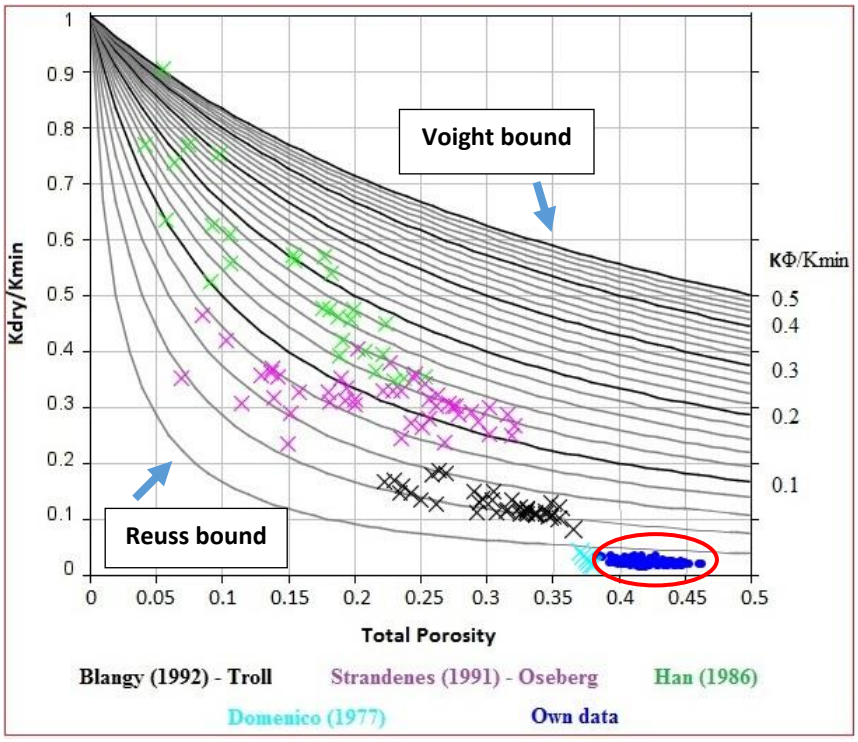

Figure 5.4: Dry rock data from both laboratory measurements and the data corresponding to the target reservoir in well F04-01 (marked by the red circle), when the total porosity approach is used. $K_{dry}/K_{mineral}$ represents the normalized bulk modulus. The black lines represent lines of constant normalized pore stiffness. Note that $K_{min}=K_{mineral}$.

Variations in stiffness in sandstones can be related to a number of factors such as the grain-to-grain contacts, the amount and type of cement, the shale content and the distribution of pore shapes throughout the rock (Simm, 2007). The purpose of the $K_{dry}/K_{mineral}$ plot is to check the quality of the derived dry rock moduli in the Gassmann process, since data points outside the Reuss and Voigt bounds are assumed to be physically impossible.

Han's (1986) measurements were performed on a set of consolidated sandstones with varying clay content (<5% - >50%). Samples which contain clay contents between <5% and 10% have porosities higher than 0.15. It is evident from figure 5.4 that these consolidated sandstones show a linear trend which cross-cuts the lines of constant normalized pore space stiffness, with varying porosity. The data set from the Oseberg field (Strandenes, 1991) consists of high-porosity rock samples which contain shale and have strong intrinsic anisotropy. These (semi-) consolidated shaley sands tend to follow, more or less, the trend of the normalized pore space stiffness lines. Blangy's (1992) set represents poorly consolidated sands from the Troll field with porosities between 0.22 and 0.38. The same trend is observed here as in the Strandenes (1992) dataset. Domenico (1977) performed laboratory measurements on unconsolidated porous sand reservoirs with total porosities of approximately 38%. It is expected that the sediments analyzed in this study correspond to the plotted samples of Domenico

(1997), due to the unconsolidated nature of the reservoir, and to Strandenes' (1991) data set because of the fraction shale in the reservoir studied.

The data points from the reservoir studied in this work show indeed major similarities with both Domenico's (1977) and Strandenes' (1991) datasets, which suggests the usage of the total porosity approach in this work. Figure 5.5 compares the derived normalized bulk moduli obtained by using both the total and effective porosity approach. The effective porosity approach results in negative bulk moduli values only. The negative values are physically impossible and according to Simm (2007) this is a common result when using the effective porosity approach. Although dry clay properties are obtained from literature and therefore not specified to the area of interest, while shale properties are derived from local log data, the total porosity approach is used in this study.

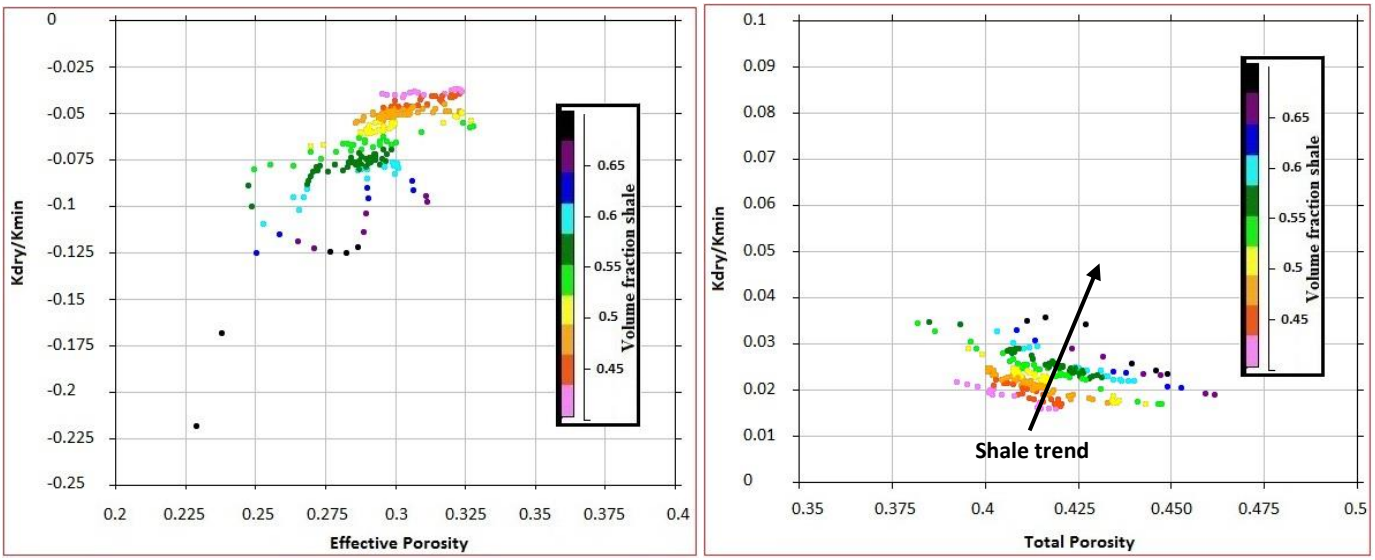

Figure 5.5: Left: dry rock data obtained from Gassmann inversion using the effective porosity approach. Right: dry rock data obtained from Gassmann inversion using the total porosity approach. Data points correspond to the reservoir of interest in well F04-01 and are colored by shale volume fraction.

A clear shale trend can be defined in the right plot of figure 5.5. All the points in this plot are located below the Reuss bound (figures 5.4 and 5.6) suggesting that the sediments are in suspension, which seems unrealistic. These erroneous low dry bulk modulus values will lead to large saturated bulk modulus changes (equation 30 in section 2.3.1). In order to solve this issue, a lower bound of a constant normalized pore stiffness of 0.02 is added: the Reuss bound. Every data point beneath this line is clipped, projected onto, the boundary at equal porosity and the fluid substitution will occur based on this revised dry rock modulus. Another important remark is the fact that shale may violate Gassmann's assumptions (section 2.3.2). In order to account for this, a cut-off has been applied to the volume fraction shale: only data with shale fractions between 0 and 0.5 are taken into account. In this way, fluid substitution is applied only to the cleanest sands within the reservoir. Figure 5.6 presents the new results: the final values for the dry bulk modulus obtained from Gassmann inversion using the cut-off.

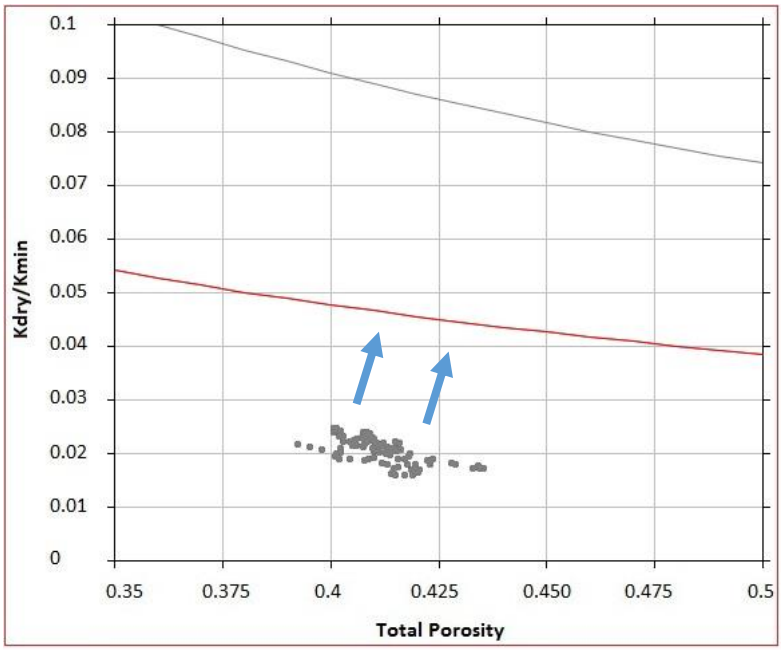

Figure 5.6: The final dry rock data obtained from Gassmann inversion using the total porosity approach after applying a cut-off to the volume fraction shale. The points, in grey, are 'clipped' to the lower bound of constant pore stiffness; the Reuss bound shown in red. The data points correspond to the area within the reservoir where fluid substitution has been applied; the red area in figure 5.7.

5.3.3 From dry to final bulk moduli

Since at this point values for the dry bulk modulus are derived from equation 30 in section 2.3.1, the same equation can be used to estimate the bulk modulus of the saturated rock after fluid substitution (K_{sat}^{final}) using the following steps:

1- Estimate the bulk modulus and density of the desired hydrocarbon (gas in this study), K_{hyc} and ρ_{hyc}, using Batzle and Wang's (1992) method described in section 5.1.3.1.
2- Evaluate the bulk modulus and density of the desired fluid, K_{fl} and ρ_{fl}, using equations 33 and 34 in section 2.3.1. Use the obtained bulk moduli and densities of brine (step 2 in section 5.3.2) and hydrocarbon (step 1 in this section) as input parameters.
3- Estimate the density of the saturated rock after fluid substitution, ρ_{sat}^{final} (g/cm^3), using the following formula:

$$\rho_{sat}{}^{final} = \Phi\,\rho_{fl} + (1 - \Phi)\rho_{mineral} \qquad (71)$$

where $\rho_{mineral}$ is the density of the mineral matrix (step 1 in section 5.3.2) and ϕ is the total porosity (as the total porosity system is chosen).

4- Estimate the bulk modulus of the saturated rock after fluid substitution, K_{sat}^{final}, using equation 30 in section 2.3.1. Using the bulk modulus of the desired fluid (step 2 in this section), the bulk

modulus of the mineral matrix (step 1 in section 5.3.2), the dry bulk modulus (step 4 in section 5.3.2) and the total porosity as input parameters.

5- Finally, derive the seismic velocities after fluid substitution (V_p and V_s in m/s) using equations 1 and 2 in section 2.1.1. Use the bulk modulus and density of the saturated zone after fluid substitution (steps 3 and 4 in this section) and the initial shear modulus, which remains constant during fluid substitution (step 3 in section 5.3.2).

The mentioned methodology (e.g. Gassmann dry rock modelling) has been performed using RokDoc software.

5.3.4 Fluid substitution results

The method described above is repeated for different gas saturations and figure 5.7 shows the effect of fluid substitution on the elastic parameters (V_p, V_s and ρ) for gas saturations of 1% and 60% in the reservoir. The main differences, between the water-bearing case and the gas-bearing situation, are observed in both the compressional wave velocity and the density. At gas saturations between 0%-5% the compressional wave velocity shows a dramatically decreasing trend, between 5%-15% it slightly decreases and between 15%-100% it shows a marginally increasing trend. The density decreases linearly with increasing gas saturation and the shear wave velocity remains more or less constant as fluids and gasses do not shear. Figures 5.8 and 5.9 present respectively the theoretical behavior of the velocities (both V_p and V_s) and the density as a function of gas saturation.

Seismic reflections depend on the contrast in V_p, V_s, and ρ across an interface (section 2.1.1). In the following a constant shear wave velocity is assumed. The compressional wave velocity has a major influence, on the fluid substitution effect, at very low gas saturations. However, in the interval where V_p slightly increases (~15%-100% gas), the density has a relatively large impact due to its decreasing linear trend. Table 5.5 presents the relative contribution of both V_p and ρ on the fluid substitution effect.

Table 5.5: Relative contribution of V_p and ρ on the fluid substitution effect for intervals 0%-100% gas and 15%-100% gas. Minimum V_p is found at a gas saturation of 15%. The maximum change is defined as the difference between the maximum and minimum value of the elastic parameter in the analyzed interval.

Elastic parameter	Maximum change 0%-100% gas	Relative contribution 0%-100% gas	Maximum change 15%-100% gas	Relative contribution 15%-100% gas
V_p	665.97 m/s (~33%)	~62%	129.03 m/s (~9%)	~35%
ρ	0.416 g/cm^3 (~20%)	~38%	0.353 g/cm^3 (~17%)	~65%

For each gas saturation, average sets of elastic parameters for the reservoir are derived (table 5.6). These average sets of elastic properties are derived over the intervals where fluid substitution took place (the intervals marked in red in figure 5.7). For the seal, only one average set has been derived since no fluid substitution is performed here.

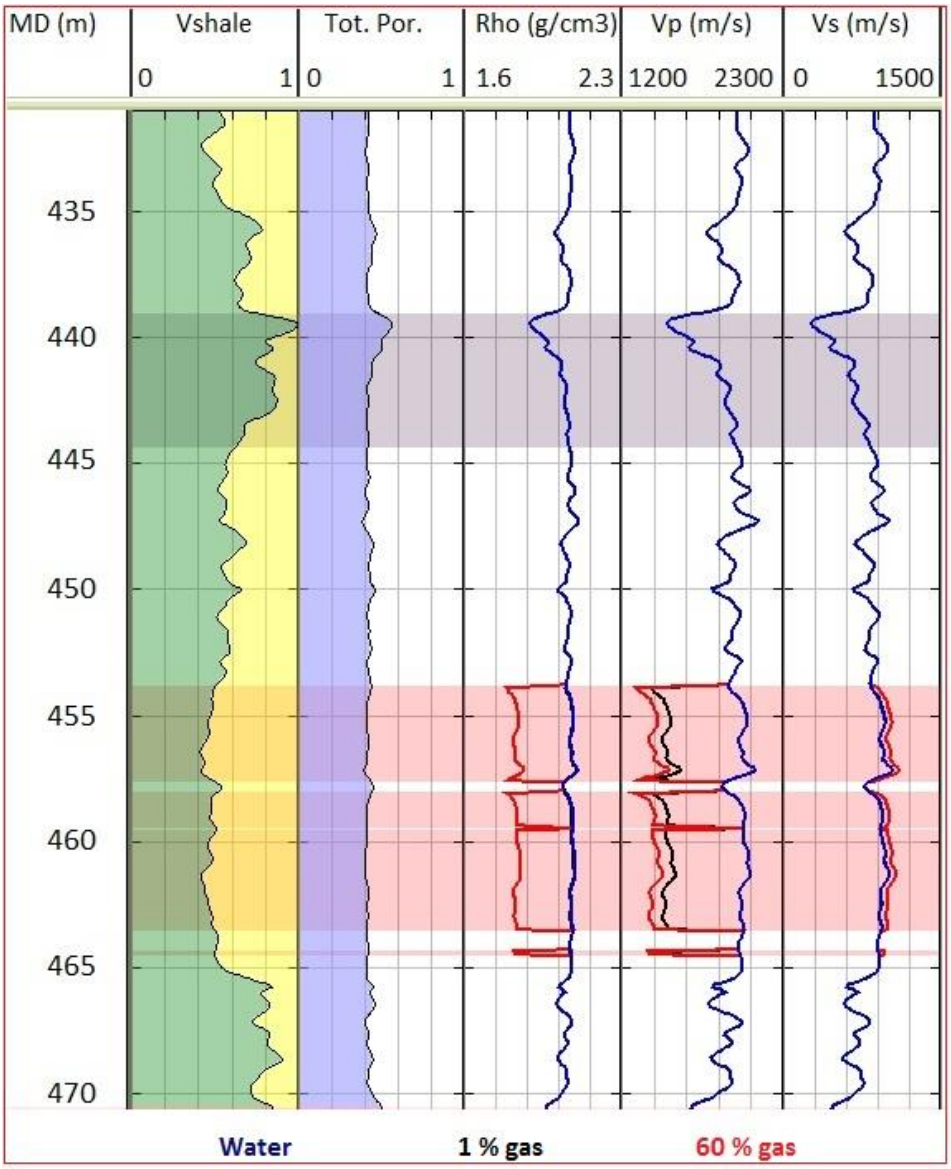

Figure 5.7: The effects of fluid substitution on the three elastic properties for the total porosity approach. From left to right: volume fraction shale in green, total porosity (fraction), density (g/cm^3), compressional wave velocity and the shear wave velocity (m/s). Fluid substitution to gas is applied to the intervals within the reservoir where the volume fraction shale is smaller than 0.5; shown in red. The seal is marked in grey. The blue, black and red lines represent respectively the water-bearing case, 1% gas in the reservoir and a gas saturation of 60% in the reservoir.

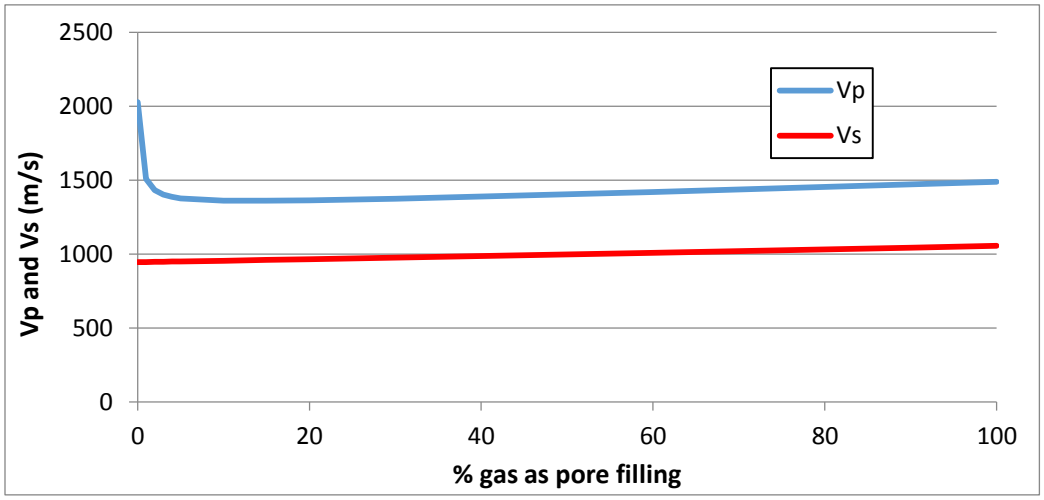

Figure 5.8: Effect of gas saturation on both the compressional and shear wave velocity. Note the decreasing trend in compressional wave velocity at low gas saturations.

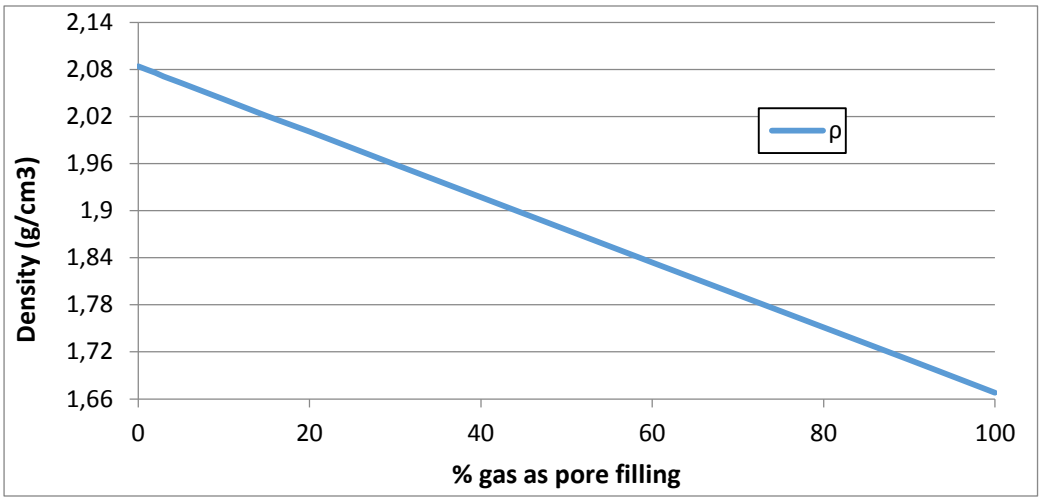

Figure 5.9: Effect of gas saturation on the density.

Table 2.6: Fluid substitution results. The average sets of elastic properties for the reservoir are calculated over the intervals marked in red in figure 5.7. The averages and the standard deviations are the input values for the stochastic Zoeppritz (1919) approach.

Gas saturation reservoir	V_p mean (m/s)	V_s mean (m/s)	Rho mean (g/cm^3)	V_p std. dev. (m/s)	V_s std. dev. (m/s)	Rho std. dev. (g/cm^3)
0 %	2027.70	946.49	2.084	33.68	37.53	0.009
1 %	1604.55	947.38	2.080	50.86	37.49	0.009
2 %	1514.07	948.29	2.076	57.40	37.52	0.009
3 %	1475.02	948.29	2.072	60.38	37.55	0.010
4 %	1453.62	950.11	2.068	62.05	37.58	0.010
5 %	1440.38	951.03	2.064	63.10	37.60	0.010
10 %	1415.59	955.65	2.044	65.11	37.75	0.010
15 %	1411.18	960.34	2.024	65.51	37.90	0.011
20 %	1412.38	965.10	2.004	65.47	38.05	0.013
30 %	1420.80	974.84	1.964	64.91	38.38	0.015
60 %	1460.62	1005.94	1.845	62.10	39.51	0.025
90 %	1509.22	1040.27	1.726	58.67	40.89	0.035
100 %	1526.89	1052.53	1.686	57.44	41.42	0.039

	V_p mean (m/s)	V_s mean (m/s)	Rho mean (g/cm^3)	V_p std. dev. (m/s)	V_s std. dev. (m/s)	Rho std. dev. (g/cm^3)
Seal	1826.26	619.94	2.018	149.59	165.01	0.055

As now complete V_p-V_s-ρ sets for varying gas saturations within the reservoir are obtained for the intervals in the reservoir where fluid substitution took place, Zoeppritz (1919) modelling (section 2.1.2) is used to model the reflection coefficients per angle of incidence in a simple 2D model consisting of 2 layers: the seal and the reservoir. Average V_p, V_s and ρ values (table 5.6) are used as an input in the *deterministic* model. In the *stochastic* model, Monte Carlo simulation is performed on the elastic properties for both the seal and the reservoir.

6. AVO modelling

As described in chapter 5, average sets of elastic parameters for the seal and the reservoir, for different gas saturations, are obtained (table 5.6). In order to model the amplitude behavior with varying angles of incidence for different gas saturations in the reservoir, the Zoeppritz (1919) equations (equation 6) are used in a simple 2D model consisting of a reservoir layer overlain by a seal (figure 6.1). The average V_p-V_s-ρ sets are used in this deterministic approach. Additionally, these equations are solved in a stochastic way by performing Monte Carlo simulation on the three parameters, for seal and reservoir separately, assuming normal distributions.

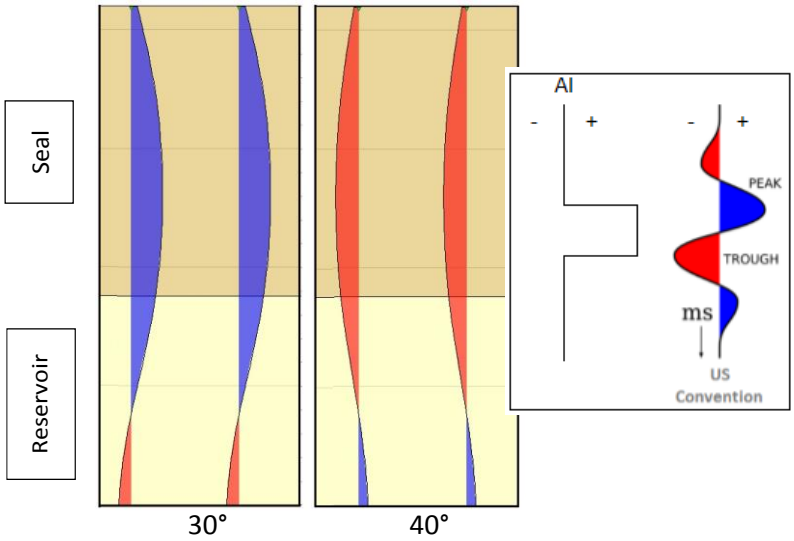

Figure 6.1: The 2D model used for amplitude modelling. The seismic responses for angles of incidence of 30° and 40° are shown. The extracted wavelet from near-angle stack seismic data has been used here. The used V_p-V_s-ρ set corresponds with the water-bearing case (table 5.6).

This chapter presents the AVO modelling results, but first the difference between deterministic and stochastic modelling and the importance of the critical angle are explained.

6.1 Deterministic versus stochastic modelling

In deterministic models, the output is fully determined by fixed, chosen parameter values. Stochastic models possess some inherent randomness by defining distributions for the input parameters. A range of parameter values and initial conditions will lead to an ensemble of different outputs. In the deterministic case, the average values for the elastic parameters for seal and reservoir are used as input in a simple 2D model. This yields only the mean solution (e.g. AVO trend) per gas saturation. To solve the Zoeppritz equations in a stochastic way, Monte Carlo simulation is performed on the parameters (V_p, V_s and ρ) for both the seal and the reservoir using the standard deviations shown in table 5.6. In this study the simulation is repeated 1000 times per gas saturation. This results in 1000 random V_p-V_s-ρ combinations, for seal and reservoir per gas saturation, which meet the specified input parameter distribution type. Since the distribution type of V_p, V_s and ρ in nature is not known, normal distributions are assumed (figure 6.2). As the parameters are mutually correlated with each other, for seal and reservoir separately, correlation coefficients have to be derived and applied to the Monte Carlo simulation.

6.1.1 V_p-V_s-ρ correlations

It is observed from seismic surveys that seismic velocities, as well as rock densities, generally increase with depth; the parameters are mutually positively correlated. Considering equations 1 and 2, this implies that the bulk and shear moduli should increase faster than the density.

Since well F04-01 only contains V_p data, and ρ and V_s data have been predicted, the correlation coefficients in this dataset are all close to 1. More realistic V_p-ρ and V_p-V_s correlation coefficients (for seal and reservoir separately), are obtained from the dataset of well A15-04. This dataset is divided into seals (shale) and reservoirs (sands) using the GR cut-off described in section 5.1.2.2. The V_s-ρ correlation coefficient could not be derived due to the fact that density measurements were performed at different depths than measurements of the shear slowness. Therefore it is assumed that the V_s-ρ correlation coefficient is equal to the V_p-ρ coefficient, which seems to be a credible assumption according to measurements performed by Miller and Stewart (1991) on clastic sedimentary rocks. The Monte Carlo simulation is performed using both the correlation coefficients of well F04-01 and well A15-04. Tables 6.1 and 6.2 give an overview of the derived correlation coefficients.

6.1.1.1 F04-01 data

The data (figure 5.7) has been filtered with respect to depth in order to establish cross plots for the seal and reservoir separately. In this way, correlation coefficients are derived corresponding to gas saturations of 0%, 1% and 100% (table 6.1). Although a gas saturation of 100% may not be a realistic assumption, these gas saturations are used as they represent extreme conditions.

Table 6.1: Correlation coefficients obtained from well F04-01.

	V_p-ρ	V_p-V_s	V_s-ρ
Seal	0.9958	0.9774	0.9724
Reservoir (Water)	0.9996	0.9041	0.9045
Reservoir (1% Gas)	0.9951	0.9438	0.9085
Reservoir (100% Gas)	0.9407	0.9703	0.8345

6.1.1.2 A15-04 data

Since no fluid substitution was performed in well A15-04, only coefficients for the water-bearing case could be derived as this is a dry well. Therefore it is assumed that the coefficients for the reservoir are constant with varying gas saturation. Results are shown in table 6.2.

Table 6.2: Correlation coefficients obtained from well A15-04.

	V_p-ρ	V_p-V_s	V_s-ρ
Seal	0.4140	0.5215	0.4140
Reservoir (Water)	0.4879	0.3627	0.4879

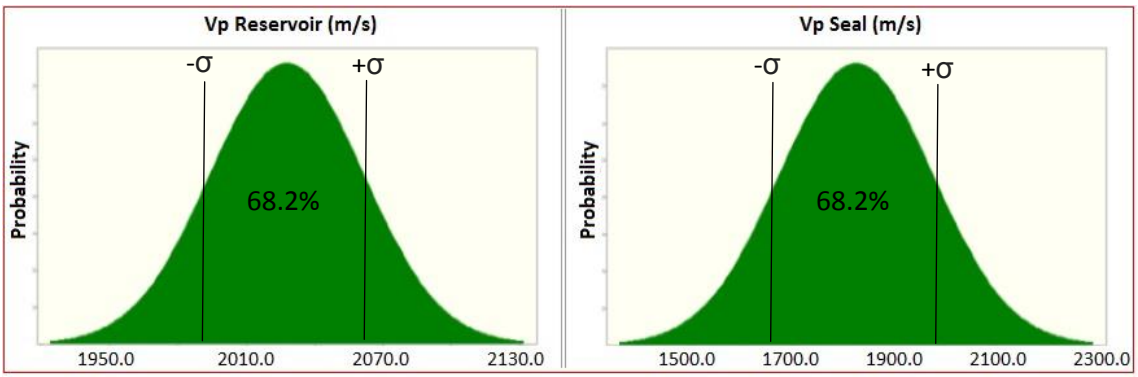

Figure 6.2: Normal distributions are used for the elastic parameters. Distributions for the compressional wave velocity, for the water-bearing situation, for both the reservoir and the seal are shown in respectively the left and right figure. The chance that a value is picked, during Monte Carlo simulation, between the mean – standard deviation and the mean + standard deviation equals 68.2%. Appendix P shows the normal distributions for all the parameters for gas saturations of 0%, 1% and 100%.

This stochastic methodology results in two sets of 1000 $(V_p\text{-}V_s\text{-}\rho)_{Reservoir}$-$(V_p\text{-}V_s\text{-}\rho)_{Seal}$ combinations per gas saturation, one using F04-01 correlation coefficients and one using A15-04 correlation coefficients. Only gas saturations of 0%, 1% and 100% are considered. The result is a distribution function which displays a range of possible outcomes, thus a bundle of AVO trends per gas saturation, which represents the rock property uncertainty (figures 6.5 and 6.6).

6.2 Critical angles

As the Zoeppritz equations used yield amplitudes that are accurate up to the critical angle, it is important to have an understanding of these critical angles corresponding to the combinations of elastic parameters modelled. The critical angle can be obtained with Snell's law (equation 5 in section 2.1.2) by assuming that the transmitted P-wave propagates along the interface (θ_2 = 90°). In this case, the corresponding angle of incidence (θ_1 in equation 5) equals the critical angle. Figures 6.3 and 6.4 present histograms of the calculated critical angles for the two sets of 1000 $(V_p\text{-}V_s\text{-}\rho)_{Reservoir}$-$(V_p\text{-}V_s\text{-}\rho)_{Seal}$ combinations obtained using Monte Carlo simulation. Only the water-bearing case has been considered.

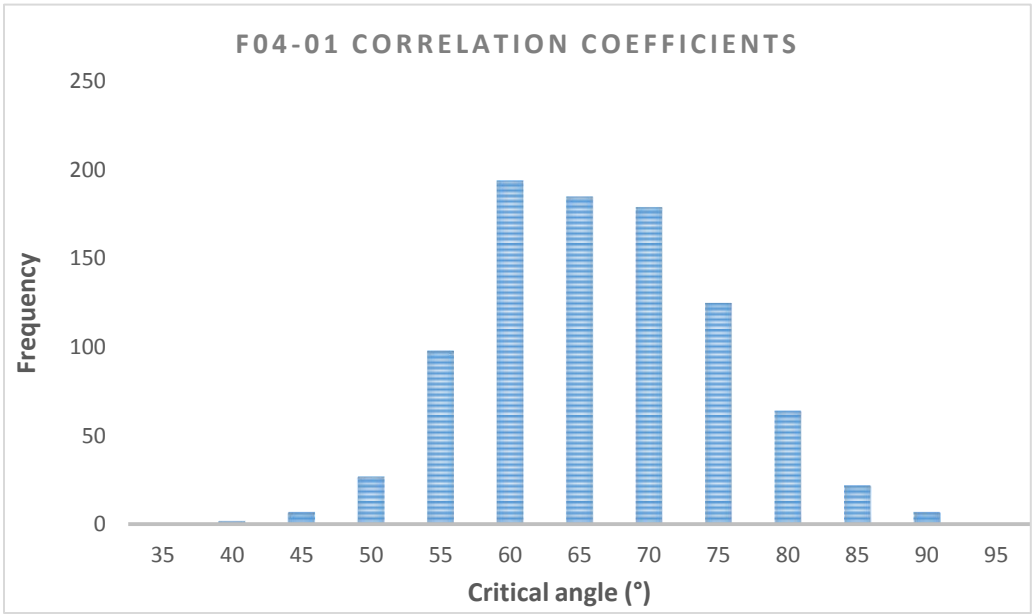

Figure 6.3: Critical angles for the dataset which was obtained using F04-01 correlation coefficients.

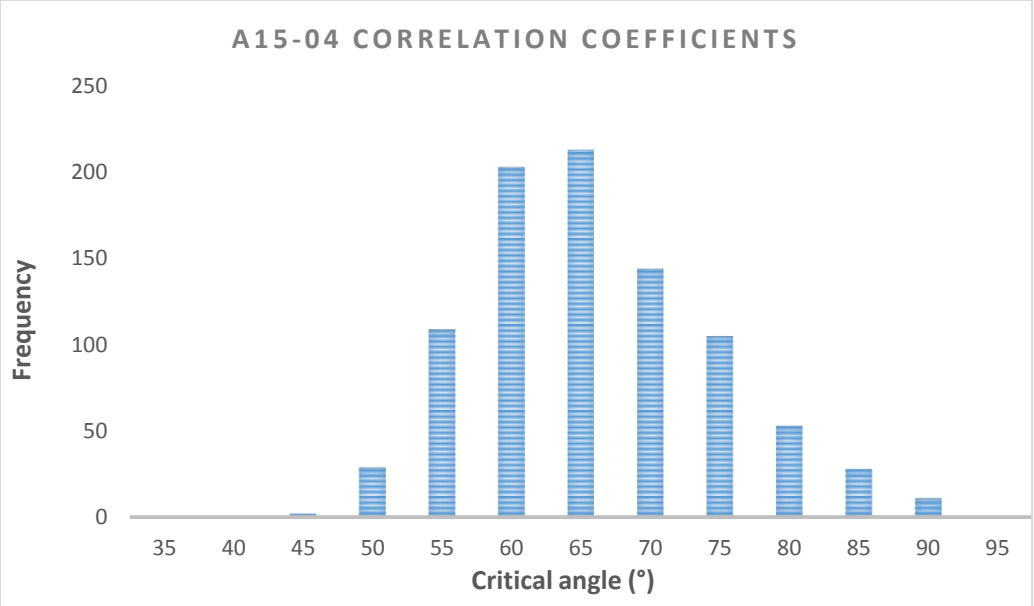

Figure 6.4: Critical angles for the dataset which was obtained using A15-04 correlation coefficients.

In both cases, most situations show critical angles of 60°-65°, but the Zoeppritz equations may fail already at 40° (figure 6.3). Therefore an angle of incidence of 40° is chosen to be the maximum angle of incidence used in this work.

6.3 Results

Figures 6.5 and 6.6 show respectively the bundle of AVO trends obtained using F04-01 correlation coefficients and A15-04 correlation coefficients (tables 6.1 and 6.2).

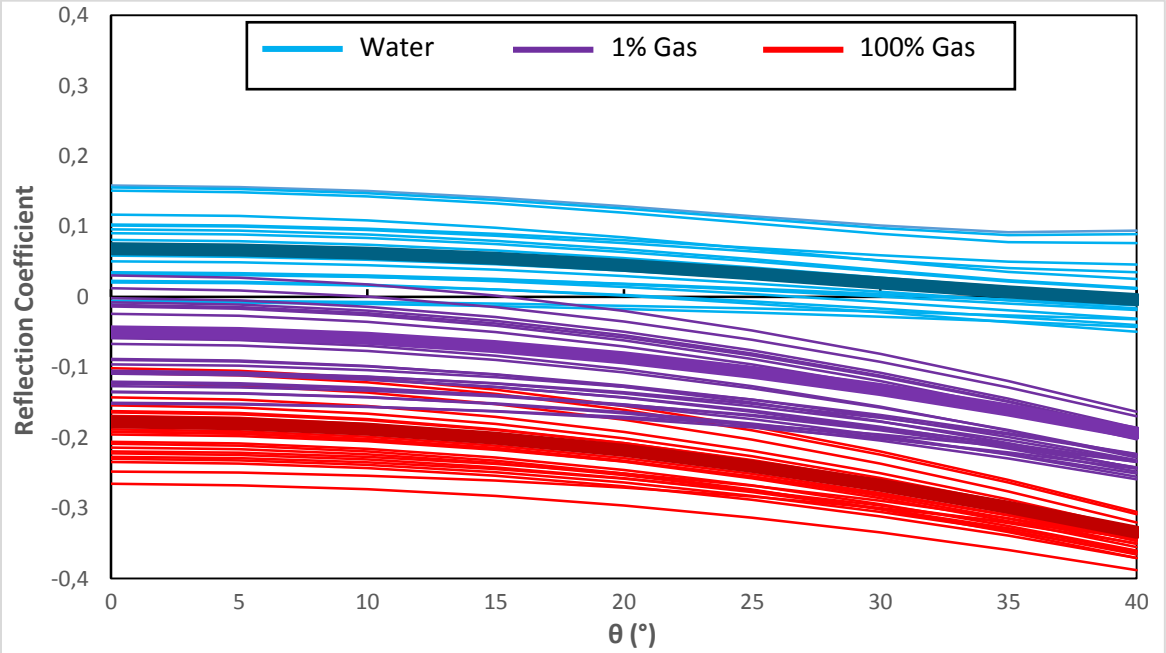

Figure 6.5: Results stochastic Zoeppritz approach using correlation coefficients of well F04-01: reflection coefficients as a function of the angle of incidence. Note that only 25 AVO trends per gas saturation are plotted. The three lines in bold correspond to the average AVO trend for water, 1 % gas and 100 % gas: deterministic solution using the mean values for the elastic properties.

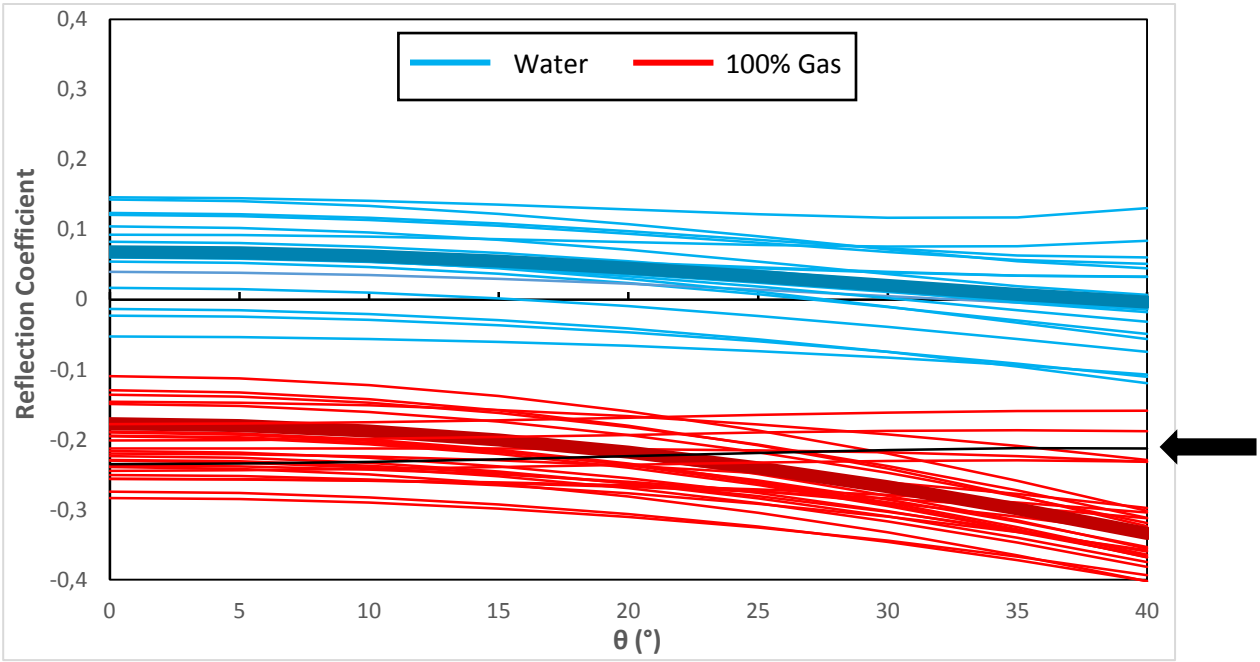

Figure 6.6: Results stochastic Zoeppritz approach using correlation coefficients of well A15-04: reflection coefficients as a function of the angle of incidence. Note that only 25 AVO trends per gas saturation are plotted. The two lines in bold correspond to the average AVO trend for water and 100% gas: deterministic solution using the mean values for the elastic properties. For clarity, only the water and the 100% gas cases are shown. The black AVO trend, marked by the black arrow, is further elaborated in figure 6.7.

The bundles of AVO trends in figures 6.5 and 6.6 represent the rock property uncertainty. The water-bearing AVO response might have a positive or a negative magnitude at zero-offset, and it may show a polarity reversal at angles of incidence of 30°-35°. Most of the time the water-bearing response has an opposite polarity with respect to the modelled gas-bearing responses (figures 6.5 and 6.6 and see section 3.1.1 for full-stack seismic observations). In order to distinguish low from high gas saturations, the AVO trend is analyzed instead of the absolute reflectivity as differences in absolute reflectivity values are often too small to be observed on real seismic data, due to the relatively large amplitude variations. The AVO curves for 1% and 100% gas have more or less the same trend, which makes it challenging to distinguish between low and high gas saturations based on the AVO trend. If the rock properties, which correspond to a particular seismic signal, are exactly known, then distinguishing low from high gas saturations might be possible by looking at the zero-offset response only, as they show differences in reflection coefficients. But, due to the rock property uncertainty, an observed seismic response may belong to both a gas saturation of 1% and a saturation of 100% gas within the reservoir (note the overlapping bundles of AVO trends in figure 6.5). However, even if the rock properties are not known exactly, and the seismic data shows no amplitude variation within amplitude anomalies, then distinction between 1% and 100% gas might be possible by looking at the far-angles since the two AVO bundles are separated from each other at these angles (figure 6.5). Nevertheless, as mentioned earlier, these differences in absolute reflectivities are often far too small to be observed on seismic data (this is further explained in section 7.2.1 and figure 7.9).

6.3.1 Positive AVO gradients

Most of the time negative AVO gradients are observed for all gas saturations. When the correlation coefficients of well A15-04 are used, 4 out of 1000 situations show positive gradients. In all of these cases the seal contains a relatively high value for the shear wave velocity (approximately two times as high as the average value; figure 6.7 and table 5.6). In order to investigate whether, in case of the positive AVO trends, distinction between low and high gas saturations is possible, Gassmann's equations are used to convert the elastic properties belonging to a gas saturation of 100% (the positive gradients in figure 6.6) back to properties which belong to 0%, 1% and 20% gas. Subsequently, the Zoeppritz equations are used to obtain reflection coefficients for the reflected P-wave. This has been done for the black AVO trend in figure 6.6 and figure 6.7 presents the results. More details about this calculation are presented in appendix Q.

In case of a positive AVO gradient (figure 6.7), the AVO curves for gas-bearing sediments still show approximately the same trend, which makes it very challenging to distinguish low gas saturations from high gas saturations.

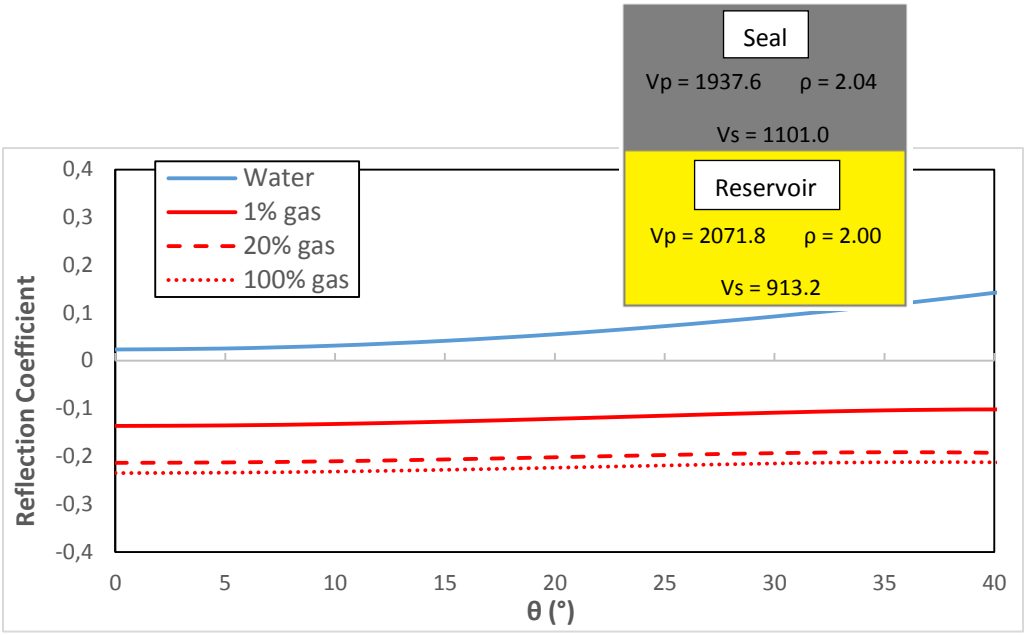

Figure 6.7: AVO curves corresponding to the 100 % gas-filled situation shown by the black arrow in figure 6.6. Gassmann's equations (total porosity approach) are used to convert back from 100 % gas to 0 %, 1 % and 20 % gas. The elastic parameters shown in the top right figure correspond to the water-bearing case (blue line).

6.3.2 Intercept-gradient cross plot

The modelling results could also be presented in an intercept-gradient cross plot. Figure 6.8 presents the average results (the bold lines in figures 6.5 and 6.6) in an intercept-gradient cross plot. Appendix R presents the derivation of the intercept and gradient values.

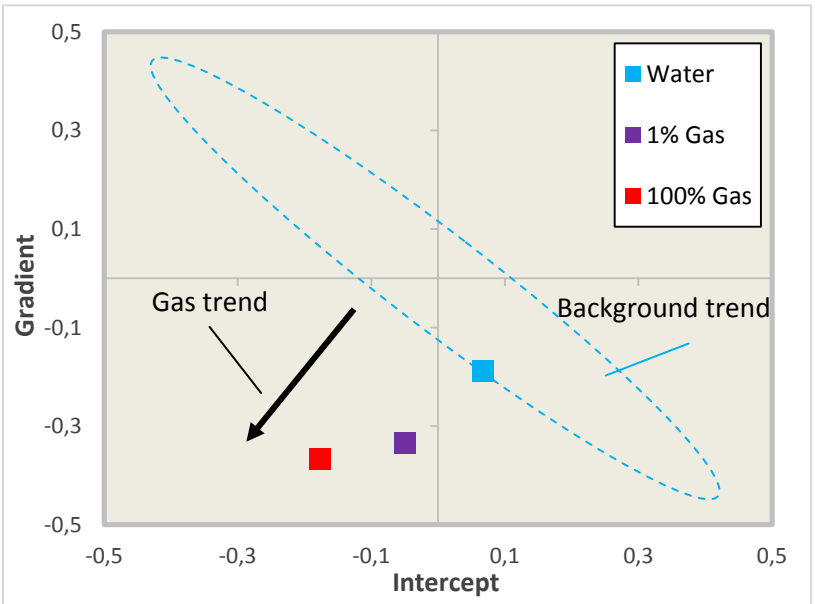

Figure 6.8: Average results presented in an intercept-gradient cross plot. Note that a gas trend can be identified which is perpendicular to the assumed background trend.

As gas saturation is the only variable in figure 6.8, a gas trend can be identified in the above figure. This trend seems to be perpendicular to the assumed background trend. Figures 6.5, 6.6 and 6.8 show that the average AVO behavior results in class 3 AVO anomalies for both 1% and 100% gas (figure 2.14). As mentioned before, very few positive gradients (class 4 AVO anomalies) were also modelled. Note that these results correspond to the top-reservoir reflector in the identified reservoir-seal combination only (figure 4.3).

7. Pre-stack data analysis

Since now the results of the forward modelling work are known, attention is paid to observations which can be made by analyzing pre-stack seismic data. The pre-stack data analysis part contains the initial AVO screening of the study area, by using the intercept-gradient approach, and an AVO refinement by tracking pre-stack gathers in more detail.

7.1 Initial AVO screening

First the anomalous regions within the study area are identified by cross plotting the amplitudes of a gradient stack with amplitudes of an intercept stack (section 2.4.2). As previously mentioned, brine-saturated clastic rocks, within a limited depth range, may show a well-defined relationship between the intercept and gradient. Deviations from the background trend may be indicative of hydrocarbons. Figure 7.1 presents the intercept-gradient cross plot with the identified background trend in white.

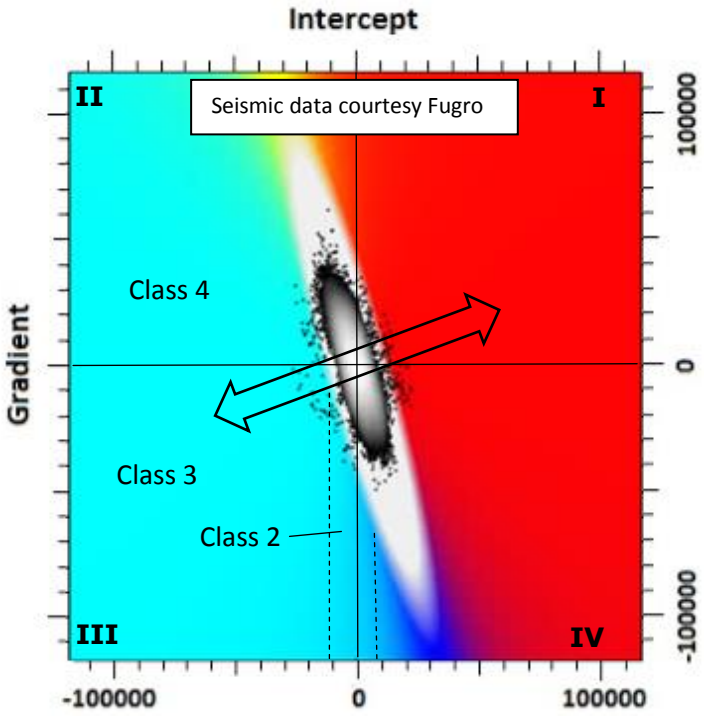

Figure 7.1: The intercept-gradient cross plot over a depth range of 400-950 m below MSL. Each black data point represents one single reflection on full-stack data, thus an alignment of traces in the pre-stack domain. The well-defined background trend is shown in white and the anomalous areas in red and light blue. Some AVO classes and the quadrant numbering system are shown as well. The big arrow presents the expected gas trend (gas effect).

As the depth interval chosen for cross plotting the intercept and gradient attributes should not be too large, because of the variation in rock properties with depth (section 2.4.2), an interval of 400-950 m below MSL was selected. This resulted in a well-defined background trend, which is assumed to be corresponding to brine-saturated clastic sediments. The points that lie off of the background trend result in the AVO anomalies shown in figure 7.2.

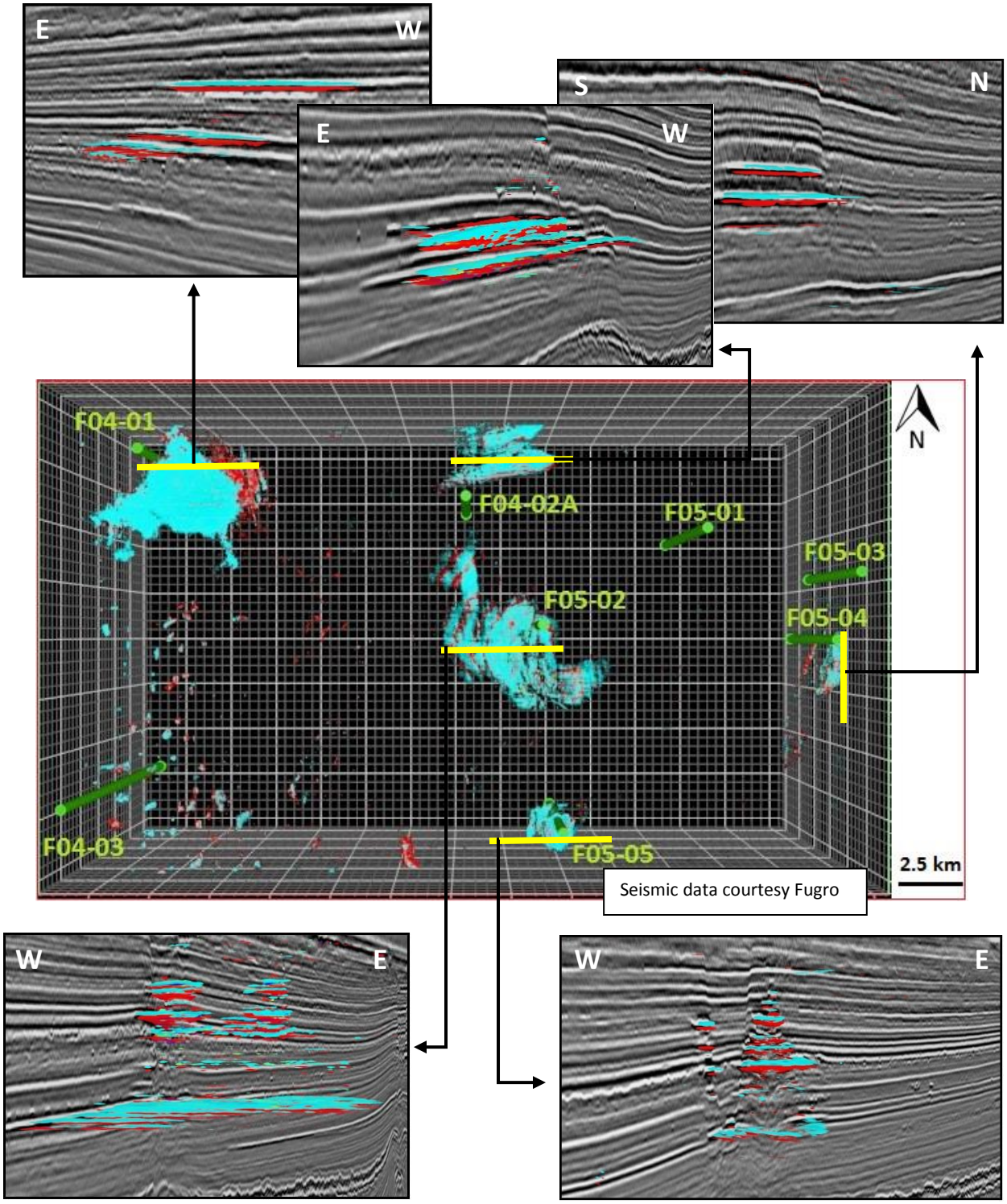

Figure 7.2: The results of the intercept-gradient approach. Five different AVO anomalies are identified, all with class 2, 3 or 4 assumed top-reservoir AVO responses. All the wells within the study area are shown in green. In the cross sections, AVO anomalies are plotted on full-stack seismic sections. The full-stack seismic data is shown in the black-white template where white represents negative amplitudes.

Figure 7.2 shows the five AVO anomalies with corresponding cross sections. These AVO anomalies correspond exactly with the bright spots observed on full-stack seismic data (section 3.1.1). Each AVO anomaly contains multiple stacked reservoirs and exhibits the light blue colored anomaly with respect to the assumed top-reservoir reflector, suggesting AVO class 2, 3 or 4 responses (figure 7.1).

Note that this method tracks amplitudes at a constant time/depth on a pre-stack gather. If the amplitudes are not horizontally aligned, for instance due to the use of a wrong stacking velocity (section 2.2.1), then this method yield erroneous results. As the amplitudes seems to be horizontally aligned within the bright reflections (figure 7.3), it is assumed that the results (figure 7.2) are reliable.

In order to investigate which exact AVO class (class 2, 3 or 4) matches with the anomalous areas within the study area, further research is done by analyzing amplitude behavior as a function of angle of incidence.

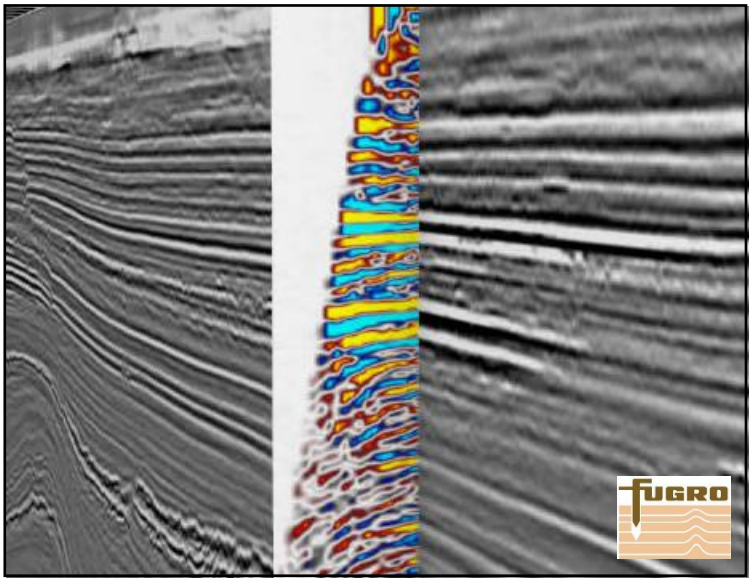

Figure 7.3: A pre-stack gather perpendicular to a full-stack line in lead F04-P1 (anomaly 1, see section 3.1.1). White and red represent negative amplitudes. Note that, in the bright reflections, the amplitudes are horizontally aligned in the pre-stack domain. Therefore it is assumed that the intercept-gradient method yields reliable AVO anomalies.

7.2 AVO refinement

As now the interesting areas within the study area are identified, some AVO anomalies are studied in more detail by tracking amplitudes on pre-stack gathers. The following workflow is applied:

1- Identify the brightest reflector in the AVO anomaly.
2- Pick the corresponding horizon/surface in Petrel software and import it in Headwave software.
3- This horizon is the input for the *gather tracker* algorithm. This algorithm performs autotracking of amplitudes in the pre-stack domain through either peaks or troughs. The outcome yields amplitude values per trace/angle of incidence.
4- For each AVO anomaly, two subsets are used: one within the anomaly and one off-structure. In this way the AVO behavior between presumed gas- and water-filled sediments is compared.

The default parameters for the gather tracker algorithm ensures that it tracks through the closest peaks or troughs. If the amplitudes have very low magnitudes, or in a noisy area, the tracker might find alternative peaks or troughs and will continue tracking along those amplitudes: this may introduce uncertainties in the results.

Due to time limitations, only three AVO anomalies have been studied. Both the assumed top- and bottom-reservoir reflectors for leads F04-P1, F04/F05-P1 and F05-F08-P1 (section 3.1.1) have been analyzed and the results are shown in figure 7.4. The areas in the three anomalies that have been investigated are shown in appendix A. Note that the seismic lines in appendix A use the EU polarity convention where increasing impedance yields negative amplitudes. The data is converted to the US polarity convention (figure 2.9) in order to compare it with the modelling results.

Figure 7.4 shows that the bottom-reservoir reflectors have more or less the same AVO trend as the top-reservoir reflectors, in opposite polarity. As the AVO classification, discussed in section 2.4.1, only assumes top-gas sand reflectors, attention is paid to the presumed top-reservoir reflectors only. The three anomalies show the same AVO behavior with respect to the top-reservoir reflector: decreasing amplitudes with increasing angles of incidence (e.g. AVO class 4 anomalies). Next, leads F04-P1 and F04/F05-P1 are discussed in more detail.

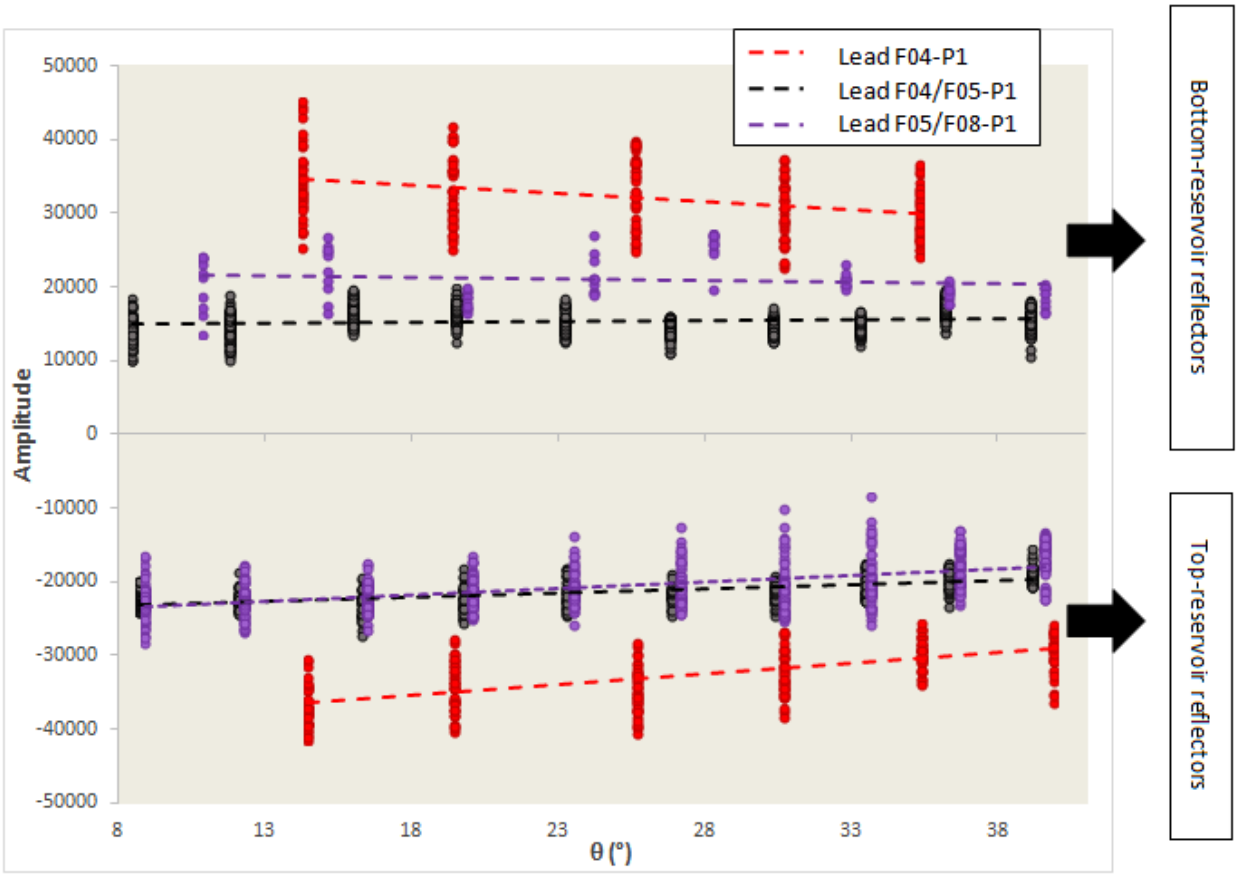

Figure 7.4: The AVO response of the top- and bottom-reservoir reflectors for leads F04-P1, F04/F05-P1 and F05-F08-P1. The exact locations within the amplitude anomalies are shown in appendix A.

7.2.1 Lead F04-P1

Figure 7.5 shows a seismic line through Lead F04-P1 (anomaly 1). The AVO response has been analyzed in areas 1 and 2, respectively the presumed water-bearing and gas-bearing sediments. Amplitude extraction is performed using the reflector of interest, and is presented in figure 7.6.

Before analyzing the AVO responses in both the presumed water-bearing and gas-bearing areas, the amplitude behavior along the seismic section which is shown in figure 7.5 is studied for angles of incidence of 14.5°, 35.8° and 57.1° using the horizon of interest (the white dashed line in figure 7.5). The results are shown in figure 7.8. The magnitude of amplitude shows a rather gradually increasing trend in the western part of the bright spot. At the eastern edge of the anomaly the magnitude of amplitude decreases relatively dramatically, which suggests a sharp transition between hydrocarbon-filled and non-hydrocarbon saturated sediments. In general, amplitude magnitudes decrease with increasing angle of incidence.

Next, the AVO behavior in area 1 and 2 is analyzed. Figure 7.9 compares the AVO response of lead F04-P1 (area 2) with the AVO response off-structure where no brightening is observed (area 1). In the water-filled area, amplitude magnitudes remain more or less constant with increasing angle of incidence whilst the gas-bearing sediments show a decreasing trend of amplitude magnitudes with increasing offset. This difference in AVO behavior might suggest that distinguishing water-bearing sediments from gas-filled sediments is possible by looking at the AVO behavior. Note that the amplitude range per angle of

incidence is relatively large, especially for the gas-bearing case, depending on the location within the anomaly. A class 4 AVO anomaly (section 2.4.1) has been observed in lead F04-P1 corresponding to the assumed top-gas sand reflector.

Within the analyzed areas (area 1 and 2) the angle of incidence, which corresponds to one particular seismic trace, varies with location. Only for the study of lead F04-P1 the variation in angles of incidence per trace is included in the analysis. Appendix S shows that the variation in angles of incidence per trace, for both area 1 and 2, is more or less negligible. As the lowest critical angle modelled equals ~40° (section 6.2), only data up to and including angles of incidence of 40° is used in this work. Figure 7.7 presents pre-stack seismic gathers from both the gas- and water-filled areas.

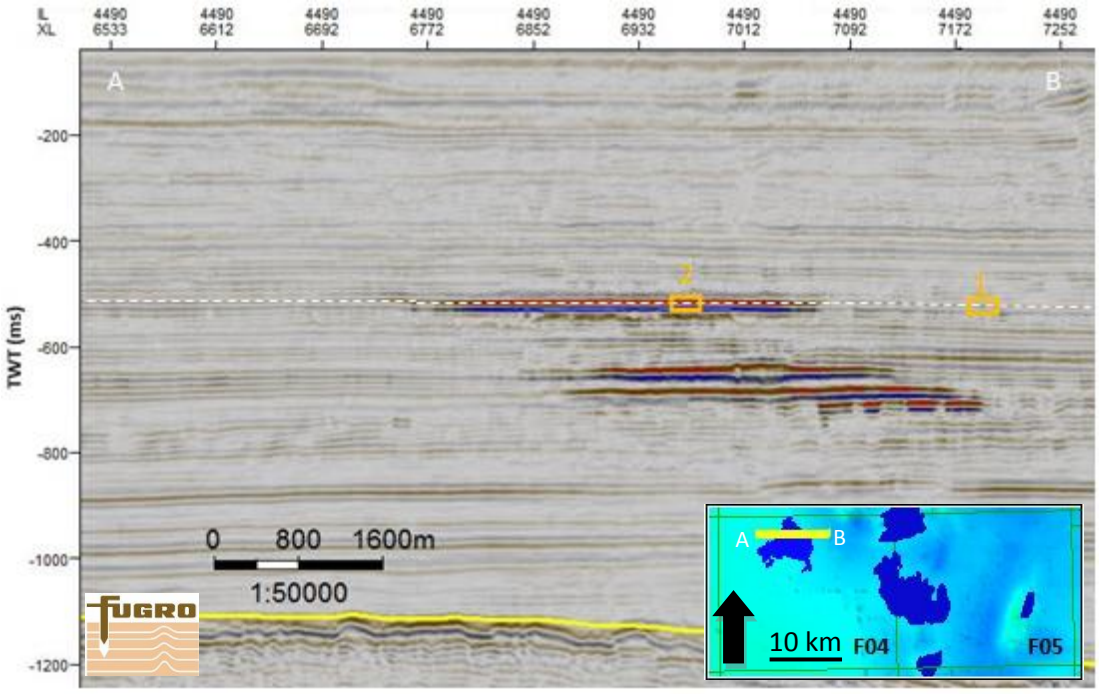

Figure 7.5: Seismic line through lead F04-P1 (anomaly 1) showing the reflector of interest at ~520 ms. The yellow boxes present the positions of the assumed water-filled area (1) and gas-filled area (2). The Mid-Miocene Unconformity is shown by the yellow line. The lower right figure shows the location of the line within the study area. An enlarged version of this figure can be found in appendix A.

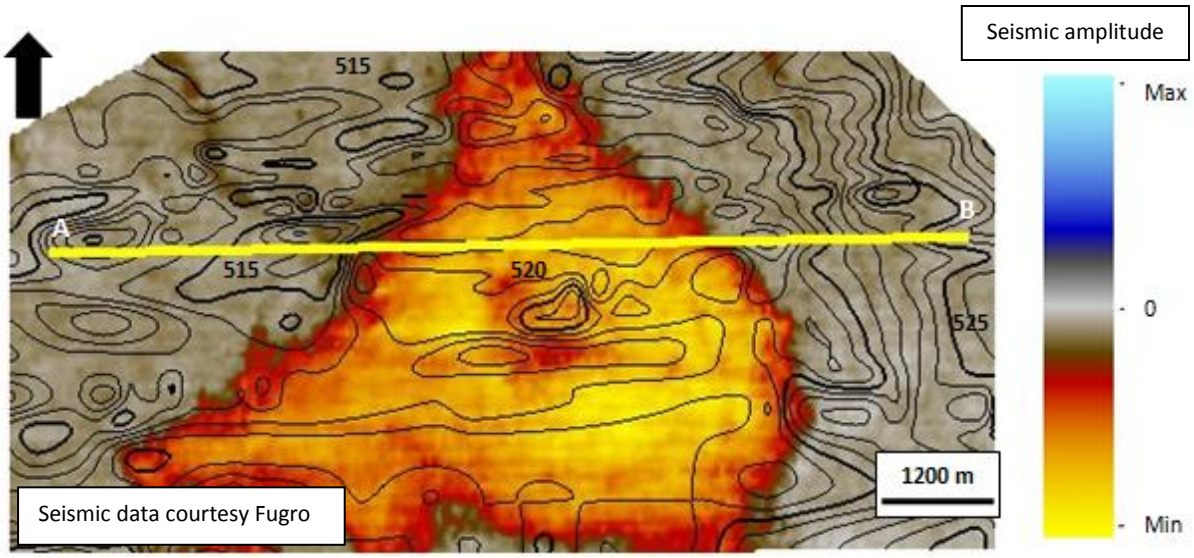

Figure 7.6: Amplitude map obtained from maximum amplitude extraction on full-stack data +/- 5ms around the horizon indicated by the white dashed line in figure 7.5. Contour lines indicate depth in TWT (ms).

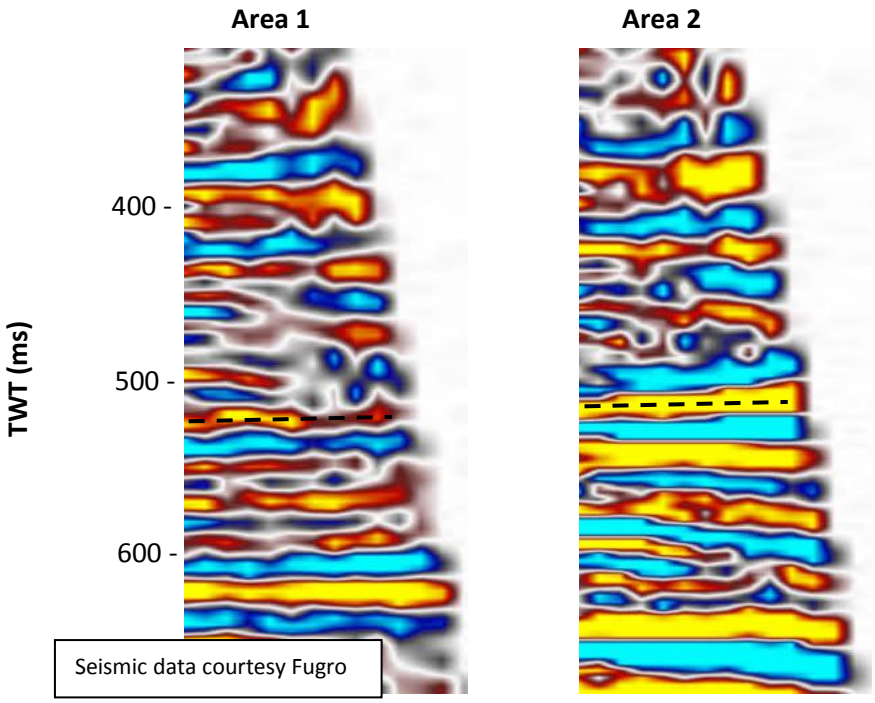

Figure 7.7: Pre-stack seismic gathers from area 1 and 2 (figure 7.5). The analyzed reflector is presented by the black dashed line.

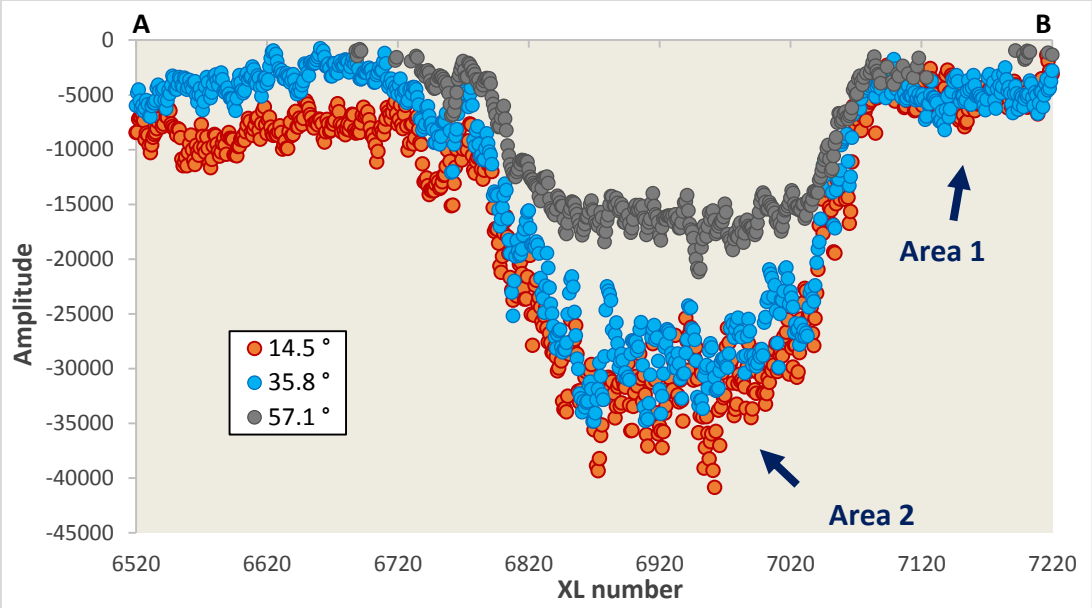

Figure 7.8: Amplitude behavior along the seismic line shown in figure 7.5 for angles of incidence of 14.5°, 35.8° and 57.1°. The assumed water- and gas-filled areas are also indicated. The reflector of interest shown in figure 7.5 has been used for this analysis. Note the decreasing trend in amplitude with increasing angle of incidence.

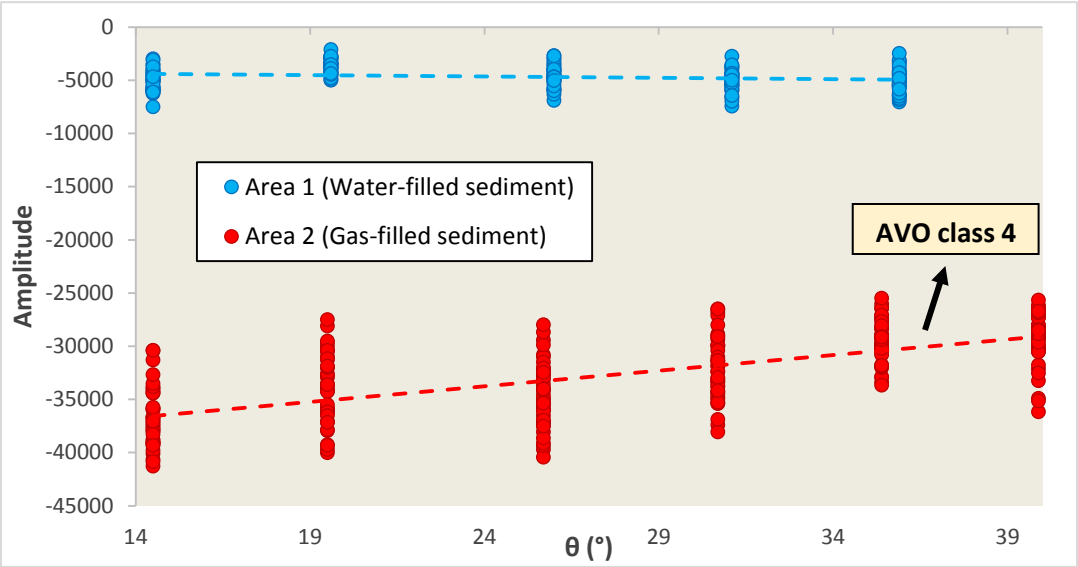

Figure 7.9: AVO data within and outside anomaly F04-P1. The locations of areas 1 and 2 are shown in figure 7.5. Each data point presents one single inline-crossline combination; one location within the investigated area.

7.2.2 Lead F04/F05-P1

A seismic line through the western part of lead F04/F05-P1 (anomaly 3) is shown in figure 7.10. Again, the AVO behavior is analyzed in both presumed water-bearing and gas-bearing sediments, respectively areas 1 and 2. The amplitude map, obtained from amplitude extraction on the reflector of interest, is presented in figure 7.11.

The amplitude behavior along the seismic line shown in figure 7.10 is studied for angles of incidence of 8.8°, 30.4° and 54.7° using the horizon of interest. The results are shown in figure 7.13. Far angle (54.7°) data is only accessible within the bright spot and is not used in the analysis due to the lowest critical angle modelled (section 6.2). The water-bearing sediments show opposite polarities with respect to the gas-filled sediments. A rather gradually increasing trend in amplitude magnitudes is observed at the edge of the anomaly. The same AVO trend is observed as in lead F04-P1: decreasing amplitude magnitudes with increasing angle of incidence.

Comparison between the AVO response of the assumed gas-bearing sediments (area 2) with the AVO behavior observed off-structure (area 1) is presented in figure 7.14. Since the variation in angles of incidence per seismic trace is more or less negligible (appendix S), fixed values for the angles of incidence, per trace, are assumed during the analysis of lead F04/F05-P1. The constant angle per trace is defined as the average incidence angle, corresponding to one particular seismic trace, within the studied area (area 1 or 2). It is striking that the water-filled sediments, area 1, show positive amplitude values whereas gas-filled sediments, area 2, show negative amplitudes; causing a clear distinction between the two AVO trends observed. Again, a class 4 AVO anomaly has been observed with respect to the top-reservoir reflector of the presumed gas-bearing sediments.

Since this anomaly is located at greater depths in the subsurface than lead F04-P1, more traces are available and the angle of incidence per trace here is smaller than at the assumed top-reservoir reflector through lead F04-P1. Figure 7.12 presents pre-stack seismic gathers for the assumed gas- and water-filled areas.

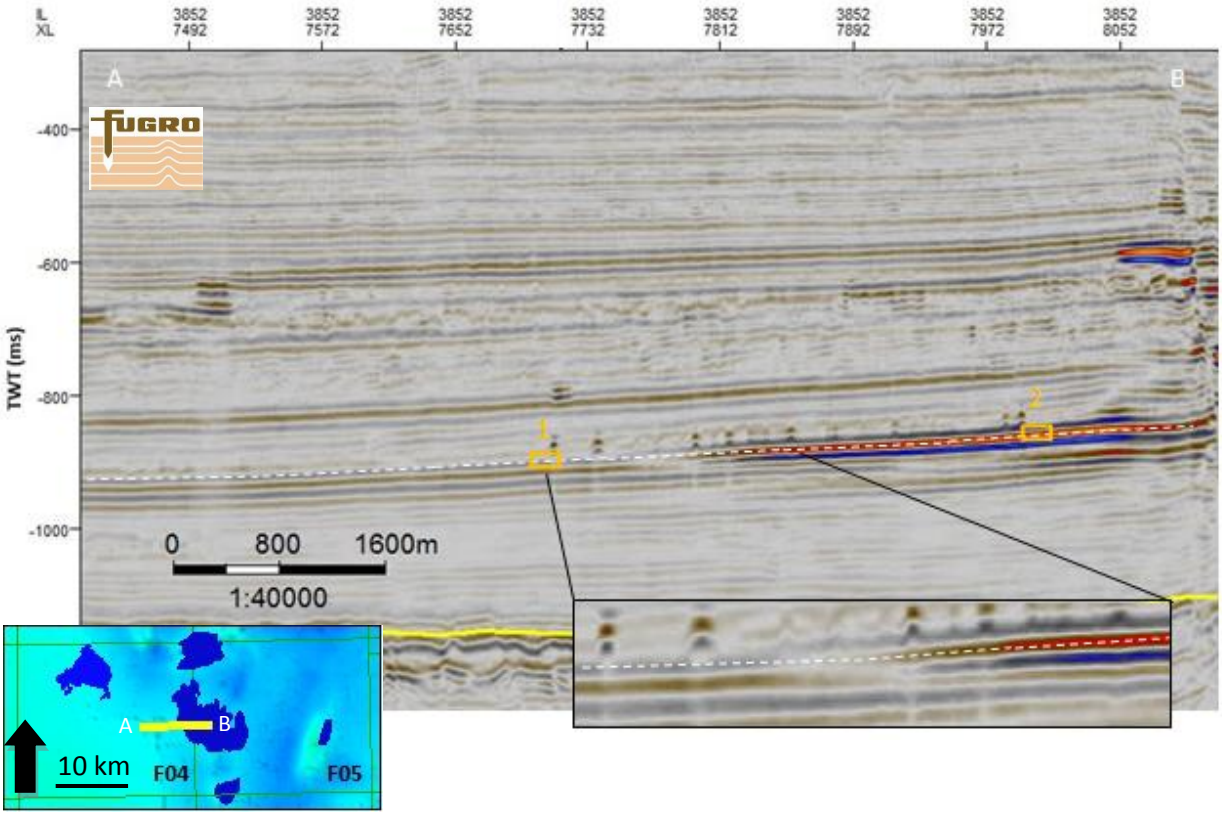

Figure 7.10: Seismic line through the western part of lead F04/F05-P1. The reflector of interest, at ~920 ms depth, is marked by the white dashed line. The yellow boxes showing the positions of the assumed water-filled area (1) and gas-filled area (2). The Mid-Miocene Unconformity is shown by the yellow line and the lower right section zooms in on the polarity reversal at the edge of the anomaly. The lower left figure shows the location of the line within the study area. An enlarged version of this figure can be found in appendix A.

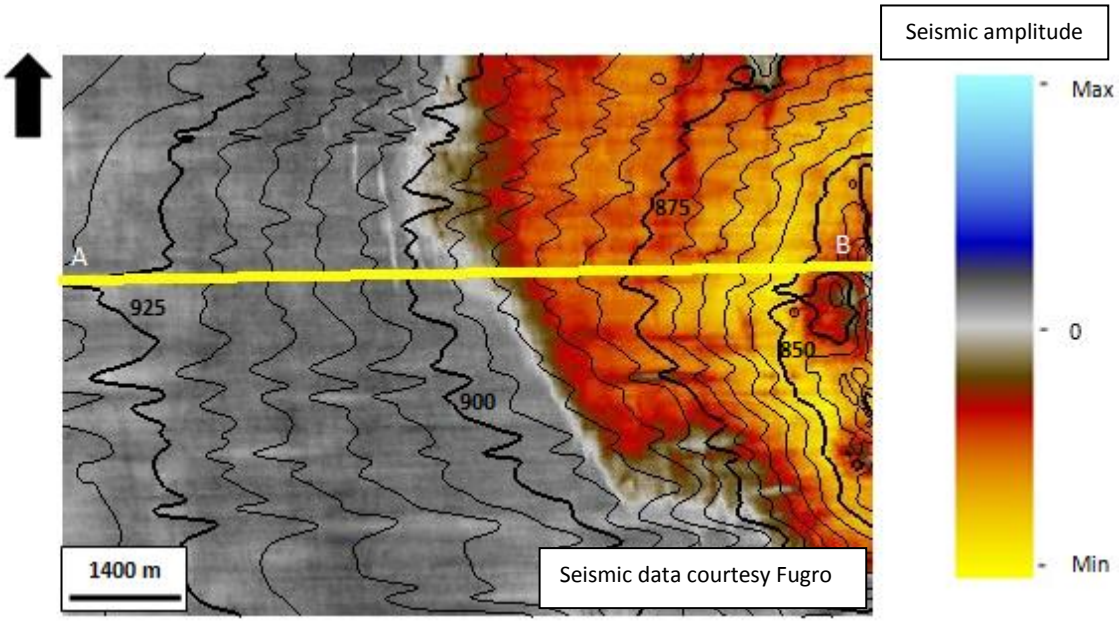

Figure 7.11: Amplitude map obtained from maximum amplitude extraction +/- 5ms around the horizon indicated by the white dashed line in figure 7.10. Contour lines indicate depth in TWT (ms).

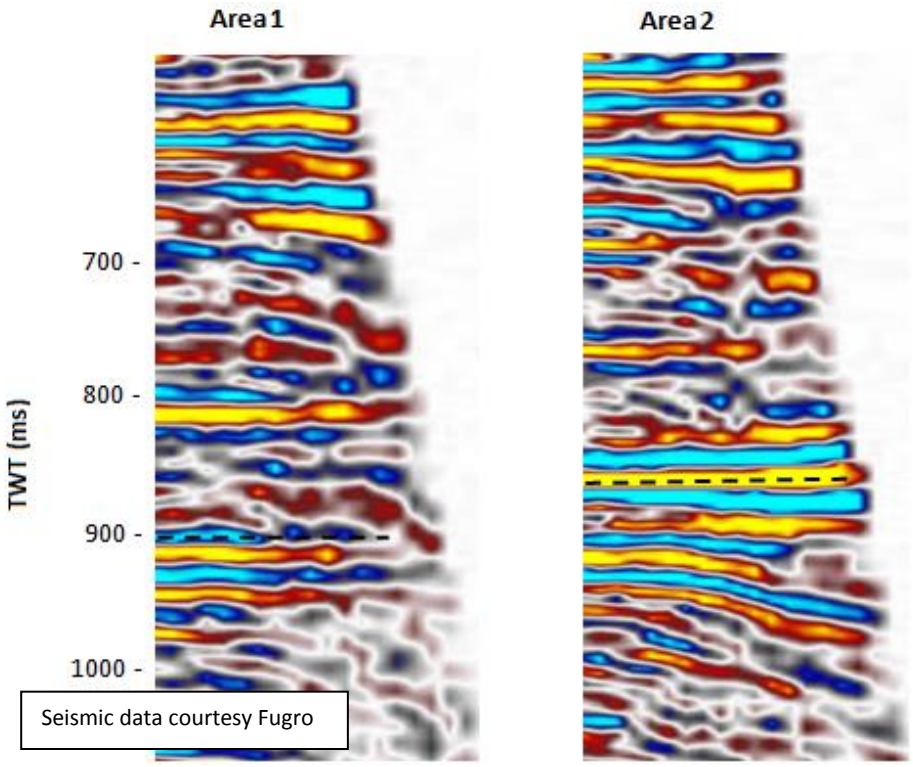

Figure 7.12: Pre-stack seismic gathers for area 1 and 2 (figure 7.10). The analyzed reflector is presented by the black dashed line.

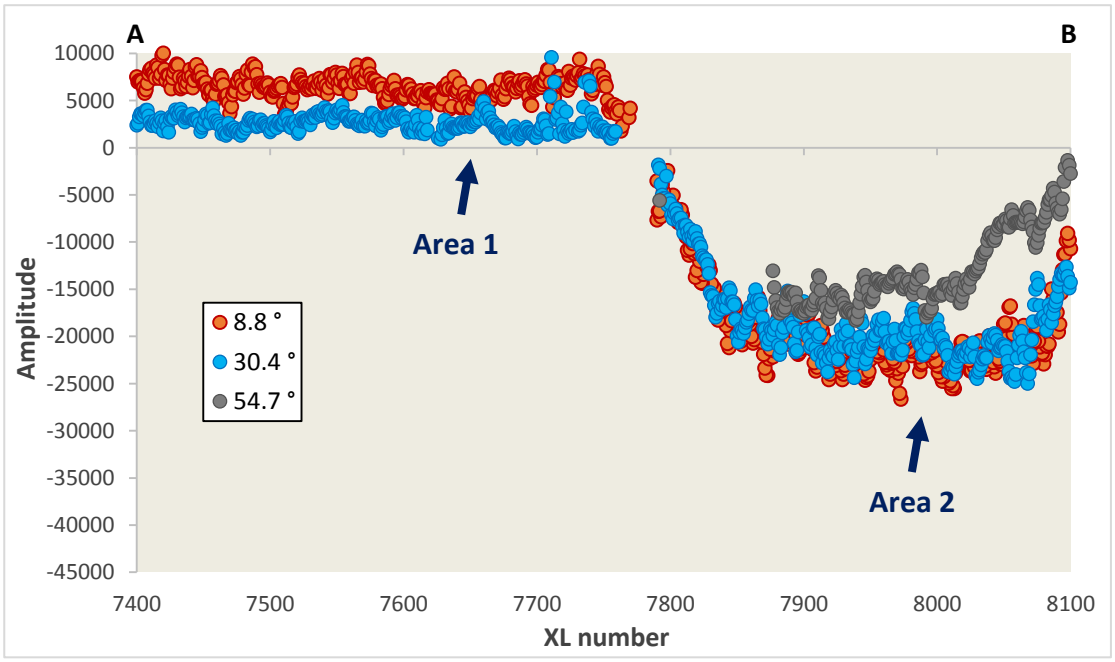

Figure 7.13: Amplitude behavior along the seismic line shown in figure 7.10 for angles of incidence of 8.8°, 30.4° and 54.7°. The reflector of interest shown in figure 7.10, and corresponding gathers in the pre-stack domain, were used for this analysis. The water- and gas-filled areas are also indicated. Note the decreasing amplitudes with increasing angle of incidence for both positive and negative magnitudes.

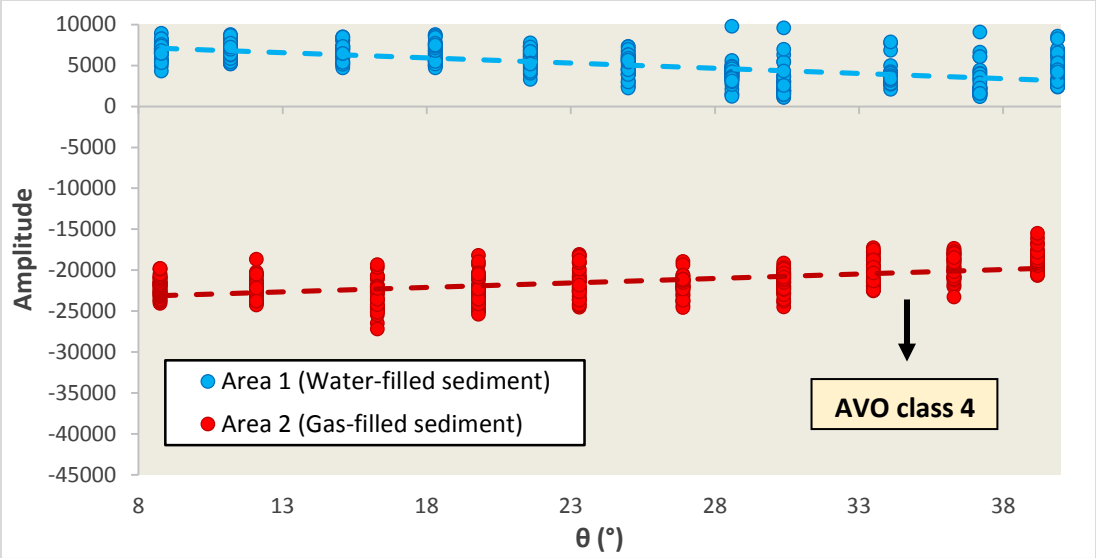

Figure 7.14: AVO data within and outside anomaly F04/F05-P1. The locations of areas 1 and 2 are shown in figure 7.10. Each data point presents one single inline-crossline combination; one location within the investigated area.

7.2.3 Results leads F04-P1 and F04/F05-P1 in intercept-gradient plot

Figure 7.15 shows the results of the AVO analysis of leads F04-P1 and F04/F05-P1 in an intercept-gradient cross plot. Since this approach assumes the two-term Shuey approximation to the Zoeppritz equations (section 2.4.2), only angles of incidence of 0°-35° are used (appendix T).

In figure 7.15 an assumed gas effect, perpendicular to the identified background trend (figure 6.8), is observed. The shift parallel to the background trend might be a lithological effect (e.g. the quartz/shale ratio).

The results of the pre-stack data analysis show AVO class 4 anomalies with respect to the assumed top-gas sand reflectors in leads F04-P1 and F04/F05-P1. The main difference between the results of these leads is the observed polarity reversal at the edge of lead F04/F05-P1. In most cases, the modelling results (figures 6.5 and 6.6) also show this polarity reversal between water-filled and gas-bearing sediments.

Whether a polarity reversal is observed between water-filled and gas-filled sediments is initially fully determined by the rock properties. However, wavelet interference (e.g. tuning effect) might disturb the seismic signal and thus influences the observations made on seismic data. In this way, interference of wavelets might control whether the polarity reversal is observed. As often relatively thin seals and reservoirs are observed in the shallow subsurface of the northern part of the Dutch offshore (section 1.1), tuning may occur and results in wavelet interferences (section 2.1.4). The modelled tuning thickness (appendix U) of ~12 m suggests that interference of the wavelet occurs when the reservoir or shale layer is thinner than 12 m. Considering seals and/or reservoirs thinner than the tuning thickness, seismic observations might lead to erroneous conclusions (e.g. no polarity reversal between water-filled and gas-filled sediments is observed whilst the rock properties suggest otherwise). Hence, the thickness of the seal and/or reservoir might have a major influence on whether polarity reversals are

observed. Wavelet interferences may also introduce an uncertainty with respect to the identified top-reservoir reflectors during the analysis.

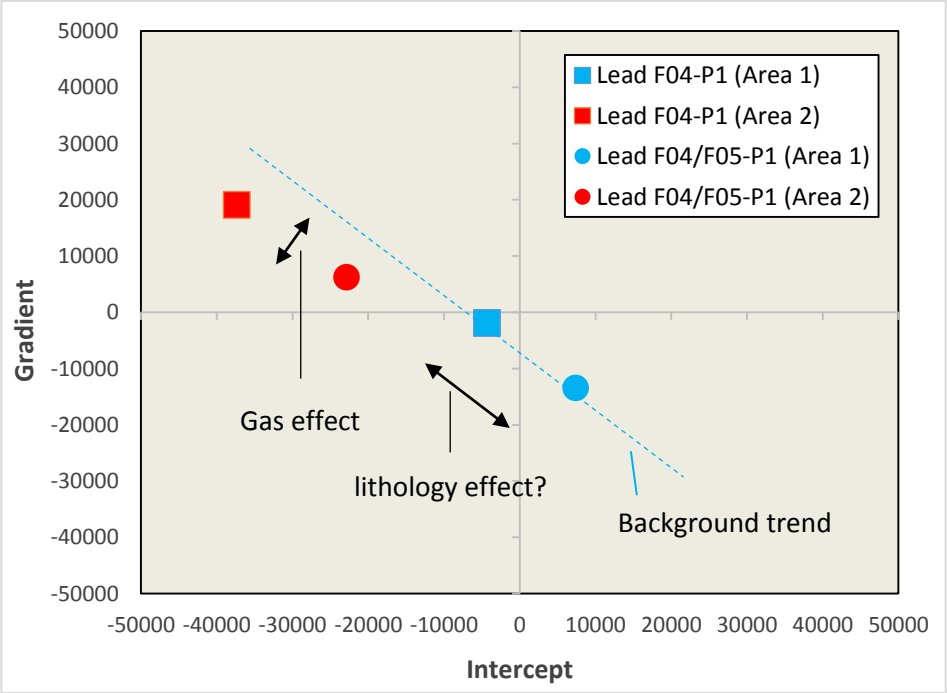

Figure 7.15: The intercept-gradient cross plot showing data from the assumed water- and gas-bearing sediments in leads F04-P1 and F04/F05-P1. Note that only angles of incidence of 0-35° were used (appendix T). A gas effect, perpendicular to the assumed background trend, might be observed.

8. Discussion

This discussion section describes the various aspects which introduce a certain level of uncertainty with reference to the final results and corresponding conclusions.

8.1 Petrophysical analysis

In order to obtain representative reservoir and seal parameters for the modelling part, petrophysical analyses are performed using data from three different wells within the study area.

8.1.1 Mineral properties

During the petrophysical analysis of wells F05-04, F05-01 and F04-01, constant mineral parameters are assumed for the analyzed interval of ~300-1100 m. Uncertainties, with respect to the results, are significantly reduced when the whole interval is divided into multiple zones of constant mineral properties; as mineral properties of shale and sands vary with depth due to compaction (figure 8.1). Compaction results in a decrease of the amount of clay bounded water, changing the density and seismic velocity of shale.

As shale is one of the constituents in the assumed mineral model, clay bounded water within shale is included in the petrophysical analysis (section 4.2). Possible presence of unmovable water in quartz is not included, which may result in ambiguous values with respect to the derived effective porosity.

8.1.2 Data

Since wells with adequate log data of the North Sea Group are extremely scarce, representative datasets regarding the shallow subsurface in the study area are rare as well. In this work, datasets of wells F05-04, F05-01 and F04-01 are used in the analysis. The derived volume fractions sets with respect to wells F05-01 and F04-01 are based on gamma ray, compressional slowness and predicted density data only. The quality of the estimated density data is questionable, as a linear relation between the compressional velocity and the density is assumed. Calibration of sonic logs generally occurs with respect to the deeper, consolidated sediments, causing inaccurate measurements of unconsolidated sediments in the shallow subsurface. Together with the fact that the linear V_p-ρ relationship holds only for well F05-04, this yields significant uncertainties in the predicted density values. Instead of using only gamma ray, compressional slowness and predicted density data, it is desired to use more log data in order to construct a mineral model (e.g. neutron porosity) as more data increases the quality of the results.

In this study, the petrophysical analysis consists of solving a system of log response equations by performing constrained optimization (section 4.2.2). The algorithm requires gamma ray, compressional slowness and density values corresponding to pure quartz, shale and brine. The required parameters with respect to shale are obtained from log analyses. As mentioned earlier, both the sonic log and the predicted density values contain uncertainties, therefore these uncertainties are reflected in the derived shale parameters (e.g. density and slowness values corresponding to shale). Sonic slowness values of ~150 µs/ft are used for shale. These values are very close to the slowness of brine: ~180 µs/ft (Crain, 2000). This suggests shale particles in suspension, which seems to be unrealistic.

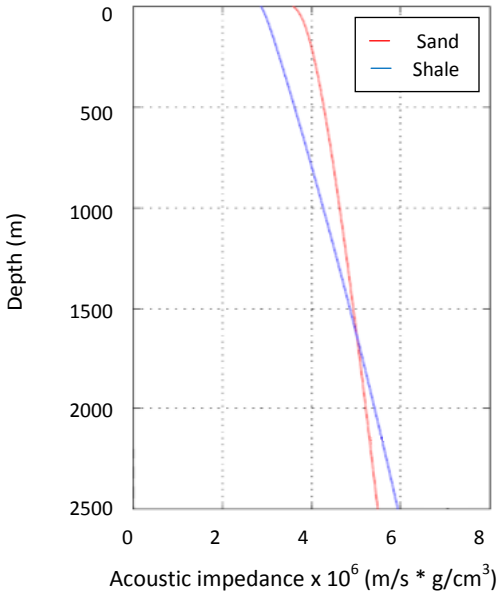

Figure 8.1: Acoustic impedance versus depth trends for sands and shale modelled by Avseth et al. (2001) using the Hertz-Mindlin theory (Mindlin, 1949). According to Avseth et al. (2001), these trends correspond well with North Sea well log data from the Glitne Field.

8.2 Rock physics

The rock physics part in this thesis contains estimates of the density and the shear wave velocity, and it covers the fluid substitution process using Gassmann's equations.

8.2.1 Density prediction

An empirical V_p-ρ relationship has been derived using data from well F05-04 and is used to predict density values corresponding to well F04-01. An interval of 550-1000 m has been used to establish this relationship. Since mineral properties vary with depth, the use of smaller depth intervals would increase the quality of the predicted density values. The reliability of the results might also be increased when distinction is made between shale and quartz minerals. However, due to the calculated volume fractions quartz and shale in well F05-04 (e.g. the absence of a clean sand interval), this was not possible.

8.2.2 Shear wave velocity prediction using Xu-White's (1995) model

Xu-White's (1995) sand-clay mixture model has been used to predict shear wave velocities since this method accounts for the volume fraction shale/clay within the reservoir. Estimates of the shear wave velocity are obtained from predicted mineral properties, porosity and clay content. Due to the fact that elastic properties of dry clay are highly variable (Wang *et al.,* 2001) and the assumptions made in the petrophysical analysis (e.g. estimated mineral properties), the reliability of the derived shear wave velocity values is debatable.

8.2.3 Prediction of fluid properties using Batzle and Wang's (1992) equations

Using Batzle and Wang's (1992) equations, brine and gas properties are derived for a particular temperature and pressure. In order to predict the temperature in the modelled reservoir, a temperature

gradient of 25 °C/km is used, which is the average geothermal gradient. This gradient, combined with an estimated temperature of 5 °C at the sea floor, may yield erroneous results as the temperature gradient varies with location. However, due to the absence of temperature measurements, this approach has been used to predict temperature values for the reservoir of interest. The hydrostatic pressure gradient, which has been used to predict the pressure in the modelled reservoir, assumes that all pores are connected. This seems a valid assumption since the shallow subsurface (e.g. unconsolidated sediments) is studied in this work. In order to obtain elastic properties of gas, the gas gravity (G) is required. In this work, the gas gravity of the Groningen gas has been used. As the shallow gas in the study area most likely has a different composition of molecules, the gas gravity in the study area would be different from the gas gravity of the Groningen gas. Yet, as an alternative, the composition of the gas produced from the A12-FA field (~99% methane) could be used in order to calculate the gas gravity. However, due to time limitations, this was not feasible in this study. The brine-related equations require salinity data. In this work, salinity data has been obtained from measurements at a depth of 774 m in well MKP-14. The salinity of brine in the study area may be different from the one that has been measured in well MKP-14, this might increase the uncertainty in the results. The elastic properties of brine, which have been used in the modelling work, are based on the assumption that no gas is in solution. Although this seems a valid assumption, as attention is paid to the shallow subsurface only (relatively low pressures), it remains uncertain whether brine in the study area contains dissolved gas.

8.2.4 Mineral properties

Quartz properties were taken from the work of Crain (2000) and seem to be reliable as pure quartz properties do not vary with depth or location. As earlier mentioned, the derivation of shale properties is based on log interpretation. As the quality of the sonic slowness data is questionable, and the density and shear wave velocity data are estimated, the shale properties contain significant uncertainties. Elastic properties of dry clay are highly variable. The dry clay properties used in this work are average values based on the work of Wang et al. (2001) and the work of Castagna et al. (1993). Different modelling results are expected when other shale and/or dry clay properties are used.

8.2.5 Fluid substitution

The use of Gassmann's (1951) equations in order to perform fluid substitution in unconsolidated sediments is debatable. Although unconsolidated sediments do not expressly violate any of Gassmann's assumptions, the equations were derived for porous sandstones and not for unconsolidated sand-shale mixtures. This introduces uncertainties with respect to the results of this thesis.

The presence of shale in the reservoir might violate one of Gassmann's assumptions. In order to account for this, a cut-off has been applied to the volume fraction shale: only depth intervals with shale fractions between 0 and 0.5 are taken into account. In this way, fluid substitution is applied only to the cleanest sands within the reservoir. Although a cut-off has been applied to the volume fraction shale, fluid substitution is still taking place in a sand-shale mixture, which makes the efficiency of the applied cut-off arguable.

The total porosity approach is used in order to perform fluid substitution in the reservoir of interest as the effective porosity approach yields negative, physically impossible, bulk moduli values. As explained in sections 5.1.4 and 5.3.1, it is important to note that the total porosity approach uses dry clay properties which are obtained from literature and thus not specified towards the studied area, whilst

the effective porosity approach would use shale properties that are derived from log data and therefore specified towards the area of interest.

In this work, it is assumed that the shale layer, which acts as a seal, is 100% water-saturated. However, it seems more realistic to assume that the unconsolidated shale layer also contains a certain amount of gas when the reservoir is gas-bearing (figure 8.2).

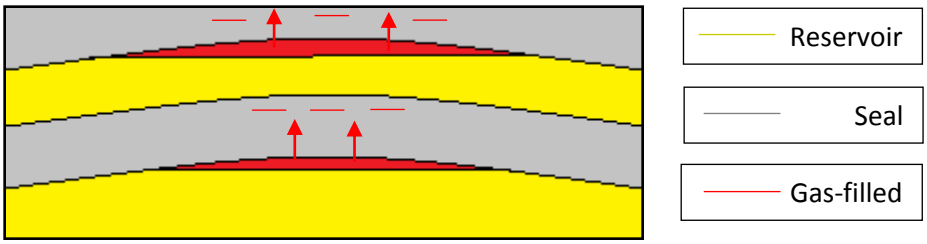

Figure 8.2: A schematic section of a typical shallow gas related trap in the studied area: multiple stacked reservoirs with flat anticlinal structures. Due to the unconsolidated nature of both the seal and the reservoir, it seems realistic to assume that some gas, which is accumulated in the reservoir, is able to migrate upwards and subsequently is accumulated within the seal.

8.3 AVO modelling

In order to model the reflection coefficients for the reflected P-wave as a function of the angle of incidence, the Zoeppritz (1919) equations are used in this study. The Zoeppritz equations assume a planar, non-slip boundary between two isotropic half-spaces. Considering these assumptions, the obtained reflection coefficients for the reflected compressional wave might be not accurate enough to describe real amplitude variations with offset for the shallow sediments studied.

A stochastic approach has been applied in which Monte Carlo simulation is performed on the distributions of the elastic properties for the seal and the reservoir for varying gas saturations. Since corresponding distributions in nature are not known, normal distributions are assumed for V_p, V_s and ρ. This may be an invalid assumption that increases the uncertainty with respect to the results, and therefore, the obtained rock property uncertainty bounds (e.g. the bundles of AVO trends in figures 6.5 and 6.6) might be invalid.

Concerning the mutual correlation between V_p, V_s and ρ (for seal and reservoir separately), correlation coefficients are derived from well data of wells F04-01 and A15-04. As the V_s-ρ correlation coefficient could not be established in well A15-04, it is assumed that it is equal to the V_p-ρ correlation coefficient. According to the work of Miller and Stewart (1991) on clastic sedimentary rocks, this seems a reasonable assumption. However, their work also shows that higher correlation coefficients could be obtained when the dataset is divided into categories based on the clay content. In this work, correlation coefficients for seal and reservoir separately are derived by dividing the A15-04 dataset into seals and reservoirs through the application of a gamma ray cut-off (section 5.1.2.2). When this dataset was filtered on the clay content, higher values with respect to the correlation coefficients are expected. This would have a big impact on the modelling results as the correlation coefficients determine which combinations of rock properties are modelled. Yet, filtering the A15-04 dataset with respect to the clay content was not possible in this study as clay content information was not available.

Angles of incidence up to 40° are investigated in this study. This is due to the fact that the lowest critical angle modelled equals 40°. However, most combinations of rock properties show critical angles of 60°-65° (section 6.2). In order to analyze more data, it is most likely more realistic to use another statistical parameter as a criteria. For instance, one may use the P90 value regarding the critical angles modelled instead of the minimum value.

In order to present the modelling results in an intercept-gradient cross plot, the Zoeppritz (1919) equations are used up to angles of incidence of 35° and subsequently a linear fit is applied. However, the two-term Shuey (1985) approximation should be used for this matter (section 2.4.2). Nevertheless, it is expected that the use of the Zoeppritz (1919) equations instead of the two-term Shuey (1985) approximation does not yield any complications as both methods show approximately the same results (figure 8.3).

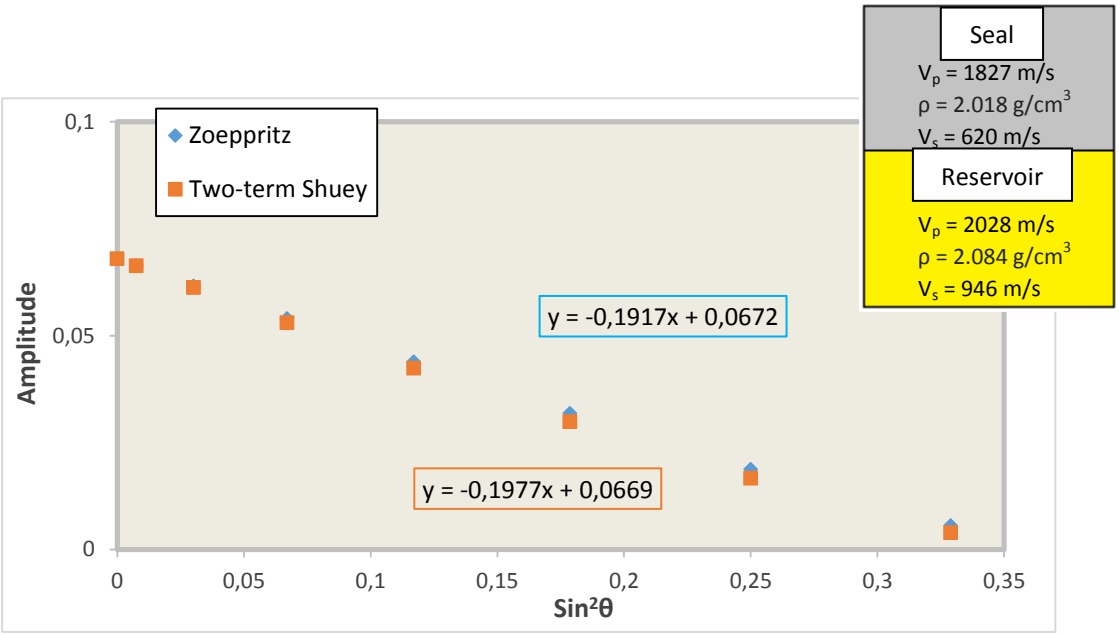

Figure 8.3: Comparison between reflectivities obtained using the Zoeppritz (1919) equations (in blue) and the two-term Shuey (1985) approximation (in orange). The elastic properties used are shown in the upper right picture. A Ricker 25 Hz wavelet has been used. Note the minor differences in intercept and gradient values.

8.4 Pre-stack data analysis

The pre-stack data analysis comprises the initial AVO screening using the intercept-gradient approach, and an AVO refinement using the gather tracker algorithm.

8.4.1 Initial AVO screening

As mineral properties of clay and shale, and thus the background trend, vary with depth as a result of compaction, the intercept-gradient method should be applied to a limited depth range. In this work, the method has been applied to a depth interval of 400-950 m. However, it would be more accurate to use a smaller interval.

As mentioned in section 2.4.3, a common problem in applying the intercept-gradient cross plot is the fact that one given point in the cross plot does not correspond to an unique combination of rock

properties (Avseth, 2005). As a result of this, the AVO anomalies observed on the data might have a lithological origin instead of a hydrocarbon-related origin. Nevertheless, this is not likely as the AVO anomalies are often conform to structure.

8.4.2 AVO refinement: gather tracker algorithm

Additional uncertainty comes from the gather tracker algorithm that is used in Headwave software to pick amplitudes as a function of offset. This algorithm only picks either peaks or troughs, thus a polarity reversal in the pre-stack domain cannot be observed. Also, it may pick wrong loops in areas where there is ample noise and/or very low amplitude magnitudes.

Top-reservoir reflectors are identified on seismic data and analyzed in more detail using the gather tracker algorithm. As the sealing shale layer may be relatively thin (~5 m thick), even thinner than the modelled tuning thickness of ~12 m, interference of the seismic wavelet might occur. This introduces inaccuracy with respect to the identification of the top-reservoir reflectors which, in his turn, results in questionable AVO observations.

8.5 Angle-stack versus pre-stack data

In the absence of pre-stack gathers, angle-stack data might be used to compute the intercept and gradient attributes from (section 3.3.2). An advantage of using angle-stack data is that it contains strong seismic responses with the noise greatly reduced from the pre-stack gathers. The results in section 3.3.2, for the top-reservoir reflector of lead F04-P1, show a decrease in amplitude magnitudes of 22.5% from an angle of incidence of 6° to an angle of 29°. When using pre-stack data, an average decrease in amplitude magnitudes of 11.1% has been observed in the same range of angles of incidence for the exact same area. Despite the difference in gradient, both methods yield the same AVO trend for the top-gas sand reflector of lead F04-P1: an AVO class 4 anomaly. As both approaches show the same type of AVO anomaly, the advantage of using pre-stack data instead of angle-stack data is debatable.

8.6 Model versus pre-stack data observations

Major uncertainty comes from the large offsets between the modelled reservoir and the analyzed amplitude anomalies. As the model parameters are based on one reservoir-seal combination in well F04-01, the obtained modelling results are representative for that particular reservoir-seal combination only. Comparison with pre-stack data observations yields high ambiguities as the AVO anomalies are located at different depths and locations within the studied area, and thus may contain other mineral combinations and rock properties.

9. Conclusions

The northern part of the Dutch offshore area shows many possibilities regarding the production of shallow gas. Therefore, a better understanding of its seismic signature is essential. The main challenge in evaluating corresponding shallow amplitude anomalies is that amplitude brightening already occurs at very low, non-producible, gas saturations. Hence, gas saturation is seen as the largest pre-drill uncertainty. In this thesis, a detailed forward model is compared with the amplitude versus offset (AVO) behavior of pre-stack seismic data of the F04/F05 licence blocks in the Dutch offshore section. The relationship between the AVO response and the gas saturation is studied: is distinction between low and high gas saturations possible by analyzing the seismic response of shallow gas in the pre-stack domain?

The dataset of well F04-01 is used, due to its data accessibility for shallow sand and shale layers, in order to obtain representative reservoir and seal parameters for the modelling work. Once a model of elastic properties for the water-bearing situation has been constructed, Gassmann's (1951) algorithm is applied to derive new elastic properties for different gas saturations within the reservoir. Subsequently, the Zoeppritz (1919) equations are used, in a stochastic approach, to model the reflectivity as a function of the angle of incidence for various gas saturations. Generally, modelling results show that the AVO trend for gas-bearing sediments indicates increasing negative amplitudes with increasing offset (e.g. class 3 anomalies). On the other hand, the pre-stack data analysis presents decreasing negative amplitudes with increasing offset (e.g. class 4 anomalies) for the top-gas sand reflectors of the analyzed amplitude anomalies. Hence, a difference is observed between the modelled AVO responses and the results of the pre-stack data analysis.

The quality of the forward modelling results concerning the unconsolidated shallow sediments in the northern part of the Dutch offshore area is controlled by fluid substitution and reflectivity modelling. To answer the sub question whether the used methods for fluid substitution and reflectivity modelling are applicable to the shallow sediments studied in this work, attention is paid to Gassmann's algorithm and the Zoeppritz equations:

- *Fluid substitution:* The use of Gassmann's equations to perform fluid substitution regarding unconsolidated sand-shale mixtures in the northern part of the Dutch offshore area remains debatable. The unconsolidated character of the reservoir does not expressly violates one of Gassmann's assumptions, however, it is desirable to be careful with resulting conclusions. As Gassmann's algorithm is only valid for reservoirs which consist of isotropic, elastic and homogeneous materials, the shale fraction within the reservoir might cause erroneous results.
- *Reflectivity modelling:* Whether the Zoeppritz equations are applicable to the shallow, unconsolidated reservoirs studied in this thesis is arguable. Considering Zoeppritz's assumptions, the obtained reflection coefficients for the reflected compressional wave might be not accurate enough to describe real amplitude variations with offset for the shallow sediments studied.

The modelling results and the pre-stack data observations show differences between the AVO response of a water- versus gas-filled unconsolidated reservoir. This discrepancy is used in order to answer the sub question whether there are differences between the seismic response, in the pre-stack domain, of a water- versus gas-bearing shallow reservoir:

- *Modelling results:* Usually, the water-bearing AVO response shows a positive magnitude at zero-incidence and it decreases with increasing angle of incidence. It may show a polarity reversal at far angles. In general, gas-bearing AVO responses have negative amplitude magnitudes at zero-offset and they increase with increasing angle of incidence. AVO trends corresponding to gas-filled sediments have steeper slopes than water-bearing AVO trends.
- *Pre-stack data analysis:* For presumed water-bearing sediments, both slightly positive and negative amplitude magnitudes are observed at near angles. In both situations, magnitudes of the amplitude decrease with increasing angle of incidence. No polarity reversals have been included in this data due to limitations of the gather tracker algorithm used. However, polarity reversals have been observed on seismic data. Gas-filled sediments show larger negative magnitudes at near angles, decreasing with increasing offset. In general, the gas-bearing AVO trend shows a steeper slope than the AVO trend corresponding to water-filled sediments.

Frequently, water-bearing AVO responses show opposite polarities with respect to gas-bearing AVO trends. When water- and gas-filled sediments show both the same polarity, then distinction between the two might be possible by analyzing the AVO trend, since AVO responses corresponding to gas-bearing sediments seem to contain a steeper slope than water-bearing AVO responses.

A striking result of this study is the difference in AVO behavior between the modelled seal-reservoir boundary and the top-gas sand as identified on seismic data. To answer the research question whether AVO analysis of gas-bearing unconsolidated sediments in the study area helps in reducing the pre-drill gas saturation uncertainty, the modelling results are compared with the pre-stack data observations. The pre-stack observations show AVO class 4 anomalies, according to the Rutherford and Williams (1989) classification, with respect to the gas-bearing sediments. On the other hand, forward modelling results indicate AVO class 3 anomalies concerning gas-filled unconsolidated sediments. It is expected that the uncertainties in rock properties and in the methods used (e.g. Gassmann's equations), the relatively large offsets between the modelled reservoir and the analyzed anomalies and the limitations of the gather tracker algorithm play a significant role in this difference. The dataset that is used in the modelling work contains measured compressional wave velocity data and predicted density and shear wave velocity values due to the scarce data availability of the shallow subsurface. The model is based on one particular seal-reservoir combination within well F04-01, therefore corresponding reservoir and seal properties might not be representative. However, this uncertainty in rock properties is taken into consideration by performing Monte Carlo simulation on the elastic properties for the seal and the reservoir.

The outcome of this study shows that, based on the dataset used, the observed AVO behavior on pre-stack seismic data cannot be modelled yet. Whether studying the AVO response of shallow gas accumulations contributes to minimizing the gas saturation uncertainty is therefore still inconclusive.

10. Recommendations

For future research, the following recommendations are given:

- *Fluid substitution.* Instead of performing fluid substitution in a sand-shale mixture, apply Gassmann's equations to a clean sand interval to avoid violations of assumptions. Well-log-based petrophysical analyses may be used to identify a clean sand interval.
- *Gas gravity offshore fields.* Rather than using the gas gravity of the Groningen gas in order to derive elastic properties of gas, the gas gravity of the produced gas from the three producing fields (e.g. the A12-FA field) could be used. This is probably more consistent with the shallow gas present in the study area.
- *Well data.* When using well data in order to derive initial elastic properties, choose a well which contains V_p, V_s and ρ data, if available, as estimations of elastic parameters introduce considerable amounts of uncertainties. This includes the recommendation to increase the amount of open hole logging activities with respect to the North Sea Group.
- *Reservoir and seal thickness.* It is recommended to identify a water-bearing reservoir-seal combination, which is used as a base-case model, of which the seal and reservoir are thicker than the corresponding tuning thicknesses. Hence, the corresponding top-reservoir reflector may be recognizable on real seismic data, without any interference of the wavelet, and be used in order to calibrate the base-case model.
- *Theoretical models in addition to well data.* A problem with using only well data to obtain an initial V_p-V_s-ρ set corresponding to a reservoir-seal combination, is that this particular reservoir-seal combination might contain different mineral constituents compared with the reservoirs that comprise AVO anomalies. Comparison between the modelling results and the AVO anomalies is therefore uncertain. When the volume fractions and elastic moduli of the individual constituents, which are present in the reservoirs that contain AVO anomalies, are known, theoretical models can be used to predict an initial V_p-V_s-ρ set which corresponds to the reservoir that comprises AVO anomalies. If the theoretical data is used in addition to well data, the model can be specified for the reservoir to which it is compared with.
- *Density data.* As at moderately to high gas saturations fluid substitution seems to have a relatively large impact on the density, since the compressional and shear wave velocity remain more or less constant within this interval, density data might be used in order to distinguish between moderately and high gas saturations. Specific gravity measurements may be performed in order to obtain density data from.
- *Angle-stack data*. Investigate the use of angle-stack data for AVO purposes in more detail. With near- and far-angle seismic cubes a difference cube can be generated that may represent the gradient. For the intercept, near-angle data might be used. If the use of pre-stack seismic data for AVO analysis yields the same results as when angle-stack data has been used, it may be unnecessary to invest in state-of-the-art pre-stack seismic data for this purpose.
- *Attenuation*. Amplitudes are affected by reflection coefficients and other phenomena's like attenuation. It is recommended to investigate the use of attenuation modelling instead of modelling correlation coefficients as a function of gas saturation.
- *Reprocessing pre-stack seismic data.* In order to minimize the uncertainties with respect to the pre-stack data analysis, reprocess the pre-stack data aiming at the shallow subsurface (e.g. new migration and NMO correction).

References

Aki, K. and Richards, P.G., 1980: Quantitative seismology: Theory and methods. W. H. Freeman and Co.

Avseth, P., 2005: AVO responses: The good, the bad and the evil. *GEOExPro magazine*, **2** (5), 22-26.

Avseth, P., Mavko, G., Dvorkin, J. and Mukerji, T., 2001: Rock physics and seismic properties of sands and shales as a function of burial depth. 71st SEG annual meeting, San Antonio.

Bacon, M., Simm, R. and Redshaw, T., 2007: 3-D seismic interpretation. Cambridge University Press.

Batzle, M. and Wang, Z., 1992: Seismic properties of pore fluids. *Geophysics*, **57** (11), 1396-1408.

Berryman, J.G., 1995: Mixture theories for rock properties. Rock physics & phase relations: A handbook of physical constants, 205-228.

Biot, M.A., 1956: Theory of propagation of elastic waves in a fluid-saturated porous solid, I: Low-frequency range; II: higher frequency range, *The Journal of the Acoustical Society of America*, **28**, 168–191.

Blangy, J.P.D., 1992: Integrated seismic lithologic interpretation*:* The petrophysical basis (Vol. 51). Dept. of Geophysics, School of Earth Sciences.

Boogaard, van den M. and Hoetz, H.L.J.G., 2012: Shallow Gas Play in The Netherlands Takes Off. 74th EAGE Conference & Exhibition, Copenhagen.

Boogaard, van den M. and Hoetz, H.L.J.G., 2014: Derisking Shallow Gas as Exploration Target by Seismic Characterisation. EAGE Shallow Anomalies Workshop, Malta.

Boogaard, van den M., Gras, R. and Hoetz, H.L.J.G., 2013: Shallow Play in The Netherlands: De-risked by Seismic Characterisation. 75th EAGE Conference & Exhibition, London.

Boogaert, H.V. and Kouwe, W.F.P., 1997: Stratigraphic nomenclature of The Netherlands, *Mededelingen Rijks Geologische Dienst*, 50.

Brown, R.J. and Korringa, J., 1975: On the dependence of the elastic properties of a porous rock on the compressibility of the pore fluid. *Geophysics*, **40** (4), 608-616.

Cardona, R., 2002: Fluid Substitution Theories and Multicomponent Seismic Characterization of Fractured Reservoirs, Doctoral Thesis, Center for Wave Phenomena, Colorado School of Mines.

Castagna, J.P., Batzle, M.L. and Kan, T.K., 1993: Rock Physics: The link between rock properties and AVO response: *in* Castagna J.P. and Backus, M.M., eds., Offset-dependent reflectivity — Theory and practice of AVO analysis: SEG Investigations. *Geophysics*, **8**, 135– 171.

Castagna, J.P. and Swan, H.W., 1997: Principles of AVO crossplotting. *The Leading Edge*, **16** (4), 337–342.

Castle, R.J., 1994: A theory of normal moveout, *Geophysics*, **59** (6), 983-999.

Chevron, 2009: Special Report: Sand control unlocks shallow gas formerly regarded as drilling Hazard, Oil & Gas Journal.

Chopra, S. and Marfurt, K.J., 2007: Seismic attributes for prospect identification and reservoir characterization: SEG Geophysical Developments Series No. 11.

Connolly, P. and Kemper, M., 2007: Statistical uncertainty of seismic net pay estimations. *The Leading Edge*, **26** (10), 1284-1289.

Crain, E.R., 2000: Crain's petrophysical handbook. Spectrum.

Domenico, S.N., 1977: Elastic properties of unconsolidated porous sand reservoirs. *Geophysics*, **42**, 1339-1368.

Feng, H. and Bancroft, J.C., 2006: AVO principles, processing and inversion. CREWES Research Report, **18**, 1-19.

Foster, D.J., Smith, S.W., Dey-Sarkar, S. and Swan, H.W., 1993: A closer look at hydrocarbon indicators. 63rd SEG annual meeting, Washingtion, D.C.

Gassmann, F., 1951: Über die elastizität poröser medien. Vierteljahrsschrift der Naturforschenden Gesellschaft in Zurich, **96**, 1-23.

Gastaldi, C., Roy, D., Doyen, P. and Den Boer, L., 1998: Using Bayesian simulations to predict reservoir thickness under tuning conditions, *The Leading Edge*, **17** (4), 539-539.

Han, D.H., 1986: Effects of porosity and clay content on acoustic properties of sandstone and unconsolidated sediments. Unpublished Ph.D. dissertation, Stanford University.

Hashin, Z. and Shtrikman, S., 1963: A variational approach to the elastic behavior of multiphase materials. *Journal of the Mechanics and Physics of Solids,* **11**, 127-140.

Hill, R., 1952: The elastic behaviour of a crystalline aggregate. *Proceedings of the Physical Society (Section A)*, **65** (5), 349-358.

Katz, D.L., 1959: Handbook of Natural Gas Engineering. New York: McGraw-Hill Higher Education.

Keys, R.G. and Xu, S., 2002: An approximation for the Xu-White velocity model. *Geophysics*, **67** (5), 1406-1414.

Kuster, G.T. and Toksöz, M.N., 1974: Velocity and attenuation of seismic waves in two-phase media: Part I: Theoretical formulations. *Geophysics,* **39** (5), 587-606.

Mavko, G., Chan, C. and Mukerji, T., 1995: Fluid substitution: Estimating changes in V_p without knowing V_s. *Geophysics,* **60** (6), 1750-1755.

Mavko, G., Mukerji, T. and Dvorkin, J., 1998: The rock physics handbook: Tools for seismic analysis in porous media. Cambridge University Press.

Miller, S.L. and Stewart, R.R., 1991: The relationship between elastic-wave velocities and density in sedimentary rocks: A proposal. CREWES Research Report, **3**, 260-273.

Mindlin, R.D., 1949: Compliance of elastic bodies in contact. *Journal of Applied Mechanics*, **16**, 259-268.

Mukerji, T. and Mavko, G., 1994: Pore fluid effects on seismic velocity in anisotropic rocks. *Geophysics,* **59** (2), 233-244.

Nam, N. and Fink, L., 2008: From Angle Stacks to Fluid and Lithology Enhanced stacks: A case study from Norwegian Sea. 7th International Conference & Exposition on Petroleum Geophysics, Hyderabad.

Norris, M.W., Hares, M. and Wood, G., 1999: For processing geophysical seismic data from a seismic acquisition system. U.S. Patent No. 5.920.828, Washington, DC: U.S. Patent and Trademark Office.

Ostrander, W.J., 2006: Memoirs of successful geophysicists. CSEG Recorder, **31** (6), 38-41.

Overeem, I., Weltje, G.J., Bishop-Kay, C. and Kroonenberg, S.B., 2001: The Late Cenozoic Eridanos delta system in the Southern North Sea Basin: a climate signal in sediment supply?, *Basin Research*, **13**, 293-312.

Potter, R.W. and Brown, D.L., 1977: The Volumetric Properties of Aqueous Sodium Chloride Solutions from 0° to 500° C at Pressures Up to 2000 Bars Based on a Regression of Available Data in the Literature: Preliminary Steam Tables for NaCl Solution*s*. US Government Printing Office.

Reuss, A., 1929: Berechnung der Fliessgrenze von Mischkristallen auf Grund der Plastizitätsbedingung für Einkristalle*. Zeitschrift für Angewandte Mathematik und Mechanik*, **9**, 49–58.

Robertson, J.D. and Nogami, H.H., 1984: Complex seismic trace analysis of thin beds. *Geophysics*, **49** (4), 344-352.

Rutherford, S.R. and Williams, R.H., 1989: Amplitude-versus-offset variations in gas sands. *Geophysics*, **54** (6), 680-688.

Schmitt, D.P., 1988: Shear wave logging in elastic formations. *The Journal of the Acoustical Society of America*, **84** (6), 2215-2229.

Sheriff, R.E., 1975: Factors affecting seismic amplitudes. *Geophysical Prospecting*, **23** (1), 125-138.

Shuey, R.T., 1985: A simplification of the Zoeppritz equations. *Geophysics,* **50** (4), 609–614.

Simm, R., 2007: Practical Gassmann fluid substitution in sand/shale sequences. *first break*, **25** (12), 61-68.

Singleton, S. and Keirstead, R., 2011: Calibration of pre-stack simultaneous impedance inversion using rock physics. *The Leading Edge*, **30** (1), 70-78.

Strandenes, S., 1991: Rock physics analysis of the Brent Group reservoir in the Oseberg Field. Stanford Rock Physics and Borehole Geophysics Project.

Swan, H.W., 1993: Properties of direct AVO hydrocarbon indicators. Offset-dependent reflectivity – Theory and practice of AVO analysis: SEG, 78-92.

Thomas, L.K., Hankinson, R.W. and Phillips, K.A., 1970: Determination of acoustic velocities for natural gas. *Journal of Petroleum Technology*, **22** (07), 889-895.

Thomsen, L., 1995: Elastic anisotropy due to aligned cracks in porous rock. *Geophysical Prospecting*, **43** (6), 805-829.

Tittman, J. and Wahl, J.S., 1965: The physical foundations of formation density logging (gamma-gamma). *Geophysics*, **30** (2), 284-294.

Verweij, J.M., Daza, C.V., De Bruin, G. and Geel, K., 2014: Capillary Seal Capacity of Cenozoic Mudstone Caprocks of Shallow Gas Occurrences, Dutch Offshore. 4th EAGE Shale workshop 2014, Porto, Portugal.

Wahl, J.S., 1983: Gamma-ray logging. *Geophysics*, **48** (11), 1536-1550.

Wang, Z., Wang, H. and Cates, M.E., 2001: Effective elastic properties of solid clays. *Geophysics,* **66**, 428-440.

Waters, K.H., 1987: Reflection Seismology: A tool for energy resource exploration. John Wiley and Sons Inc., New York.

Wood, A.W., 1955: A textbook of sound. G. Bell and Sons Ltd., London.

Wyllie, M.R.J., Gregory, A.R. and Gardner, L.W., 1956: Elastic wave velocities in heterogeneous and porous media. *Geophysics*, **21** (1), 41-70.

Xu, S. and White, R.E., 1995: A new velocity model for clay-sand mixtures. *Geophysical Prospecting*, **43** (1), 91-118.

Yilmaz, Ö., 2001: Seismic data analysis. Tulsa, OK: Society of exploration geophysicists.

Zarembo, V.I. and Fedorov, M.K., 1975: Density of sodium-chloride solutions in a temperature range of 25-350 °C at pressures up to 1000 kg/cm^2. *Journal of Applied Chemistry of the USSR,* **48** (9), 2021-2024.

Zoeppritz, K., 1919: Erdbebenwellen VII, VII B, Über Reflexion und Durchgang seismischer Wellen durch Unstetigkeitsflächen. *Nachrichten von der Königlichen Gesellschaft der Wissenschaften zu Göttingen: Mathematisch-physikalische Klasse*, 66–84.

Websites:

www.cflhd.gov

www.ebn.nl

www.gasterra.nl

www.glossary.oilfield.slb.com

www.nlog.nl